A SEARCH FOR JET HANDEDNESS
IN HADRONIC Z^0 DECAYS

Yoji Hasegawa

Stanford Linear Accelerator Center
Stanford University, Stanford, CA 94309

March 1995

*Ph.D thesis, Tohoku University

Abstract

Transport of polarization through hadronization process is one of the fundamental interest in Quantum Chromodynamics which is a theory of strong interactions. In the low energy region where the hadronization occurs, QCD calculations are difficult, therefore at present the transport can be investigated experimentally. In this study we have searched for signatures of polarization of quarks and antiquarks in hadronic jets from $Z^0 \to q\bar{q}$ decays. The polarization of quarks and antiquark produced by Z^0 decays are predicted by the Standard Model of elementary particle physics. We defined several quantities depending on "jet handedness" methods and studied the correlation between the predicted polarization and the quantities. The signal was estimated by analyzing power which represents degree of the polarization transport through the hadronization process.

The Z^0 decays were measured by SLC Large Detector and the polarized electron beam provided by SLAC Linear Collider was useful for this study. The date from the 1993 run showed no signature of the transport of quark and antiquark polarization. Upper limits on magnitude of the analyzing power were set in the range 0.05–0.15 depending on the methods.

Acknowledgements

Contents

List of Tables

List of Figures

Chapter 1

Introduction

Spin is an intrinsic nature of a particle and the spin state of a particle plays an important role in the Standard Model of electroweak interactions. The model predicts that the coupling of a weak boson to a fermion depends on the spin state of the fermion, which is called helicity. Parity violation in weak interactions is due to the asymmetry in the coupling between left- and right-handed fermions.

On the other hand, effects of the spin state in strong interactions have not been fully understood yet. Strong interactions are believed to be described by Quantum Chromodynamics(QCD). QCD describes well the nature of the strong interactions in the high energy limit where the coupling constant is small and perturbative calculations are applicable. The helicity of a quark or antiquark is conserved in this limit. However, it is not obvious how QCD describes the helicity in the low energy region where perturbative calculations are not reliable. One of the typical phenomena in this region is "hadronization"; the QCD mechanism for hadron production. Several phenomenological hadronization models, which have been proposed to describe the strong interactions in the region, do not take into account spin polarization. Therefore, the transport of quark or antiquark helicity in strong interactions is of fundamental interest. It is at present an open question whether the polarization of quarks or antiquarks produced in hard collisions is observable via the final-stage fragmentation products in the resulting jets.

Nachtmann argued for a parity-odd correlation in quark fragmentation[1]. The correlation was defined in jets and thought to serve as a test of the helicity a structure of quark-antiquark pair or a measurement of the quark and antiquark polarizations. He pointed out that there was no theory to predict how large the transport of the polarization through the hadronization process was. However, his optimistic expectation was that 5–10% of the polarization was transported to final state jets.

Dalitz *et al.* studied the transport of charm quark polarization through decays

of $c \rightarrow D^0\pi$+hadrons on the basis of a model calculation[2]. They concluded that the expected transport was small ($\approx 10^{-5}$).

Efremov *et al.*[3] suggested a new concept "Jet handedness", which can be used to determine the parton polarization through its final state jets. The idea was based on an analogy with a determination of τ polarization using $\tau \rightarrow a_1^- \nu_\tau \rightarrow \pi^- \pi^- \pi^+ \nu_\tau$ process[4]–[6]. An observable which is defined from the momenta of hadrons in a jet may reflect the helicity of the parent quark or antiquark like the measurement of the τ polarization. "Jet handedness" is defined as the asymmetry of the numbers of jets with positive value of the observable and those with negative value. Jet handedness is written as a product of the quark and antiquark polarizations and the analyzing power as a coefficient. Jet handedness is different from the τ polarization measurement in the context of theory which describes the transport of the parton polarization through the hadronization process. One of the experimental interests is therefore whether polarization effects can be really observed in hadronic jets.

The Z^0 resonance is an ideal place to study this issue because the quarks in Z^0 decays are predicted to be highly longitudinally polarized by the Standard Model (SM)[7]. If jet handedness is observed in jets by applying some method, the analyzing power for the method can be derived by comparing the jet handedness with the expected polarization of the partons. From this point of view, the study of jet handedness in $e^+e^- \rightarrow q\bar{q}$ via Z^0 is suitable for the determination of the analyzing power.

Recently Ryskin suggested a possible origin of jet handedness[8] on the basis of an experimental result[9]. He introduced the color "magnetic" field as the origin in analogy to electromagnetism. The idea has to be checked experimentally.

At present, significant transport of the polarization has not been observed experimentaly. However if a method to observe such polarization were developed, it could be applied to jets produced in a variety of hard processes in order to elucidate the spin dynamics of the underlying interactions.

Motivated by this physics interest, we have searched for jet handedness in $Z^0 \rightarrow q\bar{q}$ decays using a sample of approximately 50000 hadronic Z^0 decays produced at the SLAC Linear Collider (SLC) in collision of polarized electrons with unpolarized positrons. The SLC is the 46GeV×46GeV first e^+e^- linear collider successfully operated in the world. The data used for this study were collected in the 1993 run of the SLC Large Detector (SLD) which is a general purpose detector consisting of several subsystems with state of the art technology. The SLD experiment has been carried out under an international collaboration which presently consists of about 150 physicists and graduate students from 32 institutes in Korea, Italy, Japan, United Kingdom and the United States. Tohoku University has been participating in the construction and data analysis of the particle identification system (the Čerenkov

ring imaging detector, CRID).

This study is an extension of the previous ones at SLD[9]–[11]. The thesis presents first experimental investigations on this subject. The outline of the thesis is the following; in this Chapter, physics motivation and brief history on the subject are introduced. In Chapter 2, polarization of fermions is described within the framework of the Standard Model and jet handedness is introduced. The experimental apparatus is described in Chapter 3. Analyses of jet handedness are given in Chapter 4. Finally the results from this study are summarized in Chapter 5.

Chapter 2

Polarization in the Standard Model

The Standard Model of elementary particles consists of electroweak theory and quantum chromodynamics (QCD). Phenomena of fermion polarization are well understood by the electroweak theory, but not obviously in QCD due to the complexity of the hadronization process. In this chapter, the roles of spin and polarization in the electroweak theory and QCD will be described.

2.1 Polarization in the Electroweak Theory

2.1.1 The Electroweak Cross Section for Electron-Positron Annihilations

The differential cross section for an interaction, $A + B \rightarrow C + D$, in their center-of-mass system has a general form of:

$$\frac{d\sigma(AB \rightarrow CD)}{d\Omega}\bigg|_{c.m.} = \frac{1}{64\pi s}\frac{p_f}{p_i}|\mathcal{M}|^2, \tag{2.1}$$

where $d\Omega$ is the solid angle element around outgoing final state particle C[12], s is the squared center-of-mass energy and p_i and p_f are momenta of the initial and final state particles, respectively. $\mathcal{M}$ is the matrix element. In the process of $e^+e^- \rightarrow f\bar{f}$, $\mathcal{M}$ is divided into two components according to two mediating bosons: one is a virtual photon which mediates the electromagnetic force and the other is the Z^0 boson which mediates the weak force. Figure 2.1 shows the Feynman diagrams for both processes. $\mathcal{M}$ is a sum of the two matrix elements, i.e. $\mathcal{M} = \mathcal{M}_\gamma + \mathcal{M}_{Z^0}$. According to the

5
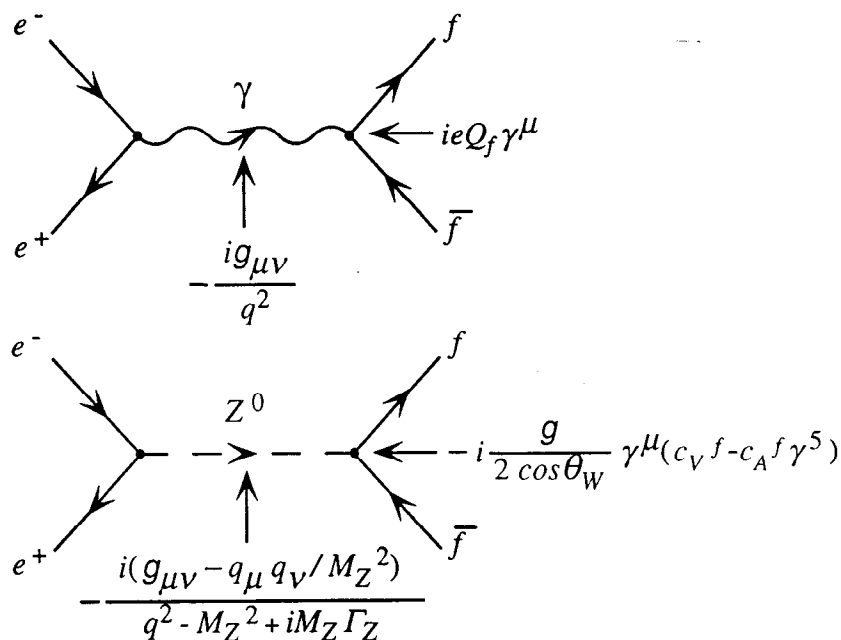
Figure 2.1: Feynman diagrams of $e^+e^- \to \gamma \to f\bar{f}$ and $e^+e^- \to Z^0 \to f\bar{f}$. g in the vertex factor is the electroweak coupling constant. Using charge of a proton e and the Weinberg angle θ_W, g is written by $g = e/\sin\theta_W$.

Feynman rule, these elements are described in terms of the propagator and the two vertex factors shown in Figure 2.1:

$$\mathcal{M}_\gamma = \bar{u}_f(ieQ_f)\gamma^\mu u_f \frac{-ig_{\mu\nu}}{q^2}\bar{u}_e(-ie)\gamma^\nu u_e \tag{2.2}$$

$$\mathcal{M}_Z = \bar{u}_f\frac{-ie\gamma^\mu}{\sin 2\theta_W}(c_V^f - c_A^f\gamma^5)u_f\frac{-i(g_{\mu\nu} - k_\mu k_\nu/M_Z^2)}{q^2 - M_Z^2 + iM_Z\Gamma_Z}\bar{u}_e\frac{-ie\gamma^\mu}{\sin 2\theta_W}(c_V^e - c_A^e\gamma^5)u_e \tag{2.3}$$

where γ^μ, M_Z and Γ_Z are the γ-matrix, mass and decay width of the Z^0 boson, respectively. q is the momentum transfer and $q^2 = s$. θ_W, c_V^f and c_A^f are the Weinberg angle, the vector coupling and the axial vector coupling constants, respectively. The electroweak coupling constant g was substituted by $\frac{e}{\sin\theta_W}$. c_V^f and c_A^f depend on the third component of the weak isospin, T_f^3, electric charge of a fermion f, Q_f, and the Weinberg angle, $\sin^2\theta_W$ and are given by,

$$\begin{aligned} c_V^f &= T_f^3 \\ c_A^f &= T_f^3 - 2Q_f\sin^2\theta_W. \end{aligned} \tag{2.4}$$

6

f	T_f^3	Q_f	c_A^f	c_V^f	A_f
ν_e, ν_μ, ν_τ	1/2	0	1/2	1/2	1
e^-, μ^-, τ^-	-1/2	-1	-1/2	$-1/2 + 2\sin^2\theta_W$	0.1448
u, c, t	1/2	2/3	1/2	$1/2 - 4/3\sin^2\theta_W$	0.6665
d, s, b	-1/2	-1/3	-1/2	$-1/2 + 2/3\sin^2\theta_W$	0.9353

Table 2.1: The third component of the weak isospin, electric charge, the axial and vector coupling constants to the weak boson for fermions and asymmetry of the strength of left- and right-handed fermions to the Z^0, where $\sin^2\theta_W = 0.2318$ is used [9]

Table 2.1 gives the values of these coupling constants for leptons and quarks. If the initial electrons are polarized by $\mathcal{P}$[1], the differential cross section for $e^+e^- \to f\bar{f}$ is written as

$$\left.\frac{d\sigma(e^+e^- \to f\bar{f})}{d\cos\theta}\right|_{c.m.} = \frac{N_c\pi\alpha^2 Q_f^2}{2s}(1 + \cos^2\theta)$$
$$-2N_c Q_f\left(1 - \frac{M_Z^2}{s}\right)k(1 - \mathcal{P})\left[c_V^e c_V^f(1 + \cos^2\theta)\right.$$
$$\left. + 2c_A^e c_A^f \cos\theta\right]$$
$$+N_c k\left\{(c_V^{e\,2} + c_A^{e\,2} - 2c_V^e c_A^e \mathcal{P})(c_V^{f2} + c_A^{f2})(1 + \cos^2\theta)\right.$$
$$\left. + 4\left[2c_V^e c_A^e - (c_V^{e\,2} + c_A^{e\,2})\mathcal{P}\right]c_V^f c_A^f \cos\theta\right\}, \quad (2.5)$$

with

$$k \equiv \frac{\alpha^2}{4\sin^4 2\theta_W}\frac{s}{(s - M_Z^2)^2 + \Gamma_Z^2 s^2/M_Z^2}, \quad (2.6)$$

where N_c is the number of colors for the fermion f. All fermions in the reaction are assumed to be massless. The first and third terms are contributions from the γ and Z^0 exchanges, respectively. The second term represents interference between the γ and Z^0 exchanges, *i.e.* $\mathcal{M}_\gamma^* \mathcal{M}_{Z^0} + \mathcal{M}_{Z^0}^* \mathcal{M}_\gamma$.

At the Z^0 pole, the interference term vanishes and the contribution from γ exchange is much smaller ($\sim 10^{-3}$) than that from Z^0 exchange. Therefore, at the Z^0 pole, the cross section in Equation (2.6) is dominated by the third term.

---

[1]The polarization of electrons is defined as: $\mathcal{P} \equiv \dfrac{n_R - n_L}{n_R + n_L}$ where n_R and n_L are numbers of right- and left-handed electrons, respectively.

2.1.2   Polarization of outgoing fermions in $e^+e^- \to f\bar{f}$

The polarization of the outgoing fermions, $\mathcal{P}_f$ is defined by:

$$\mathcal{P}_f(\mathcal{P}, \cos\theta, E_{cm}) \equiv \frac{\frac{d\sigma^{f_R}}{d\cos\theta} - \frac{d\sigma^{f_L}}{d\cos\theta}}{\frac{d\sigma^{f_R}}{d\cos\theta} + \frac{d\sigma^{f_L}}{d\cos\theta}}, \qquad (2.7)$$

where θ is the scattering angle between the incident electron and the final state fermion. Figure 2.2 shows four possible interactions of $e^+e^- \to \gamma/Z^0 \to f\bar{f}$. σ^{f_R} is the cross section for $e^+e^- \to f_R + \bar{f}_L$ and σ^{f_L} is that for $e^+e^- \to f_L + \bar{f}_R$, where the subindices R and L stand for 'right-' and 'left-handed', respectively.
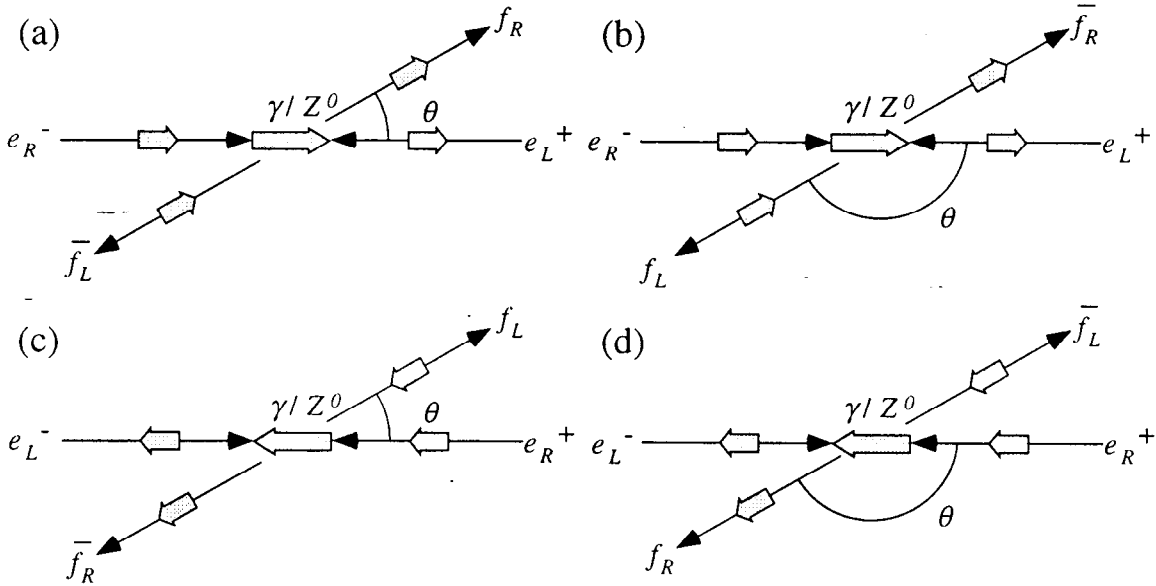
Figure 2.2: Interactions of (a) $e_R^- e_L^+ \to f_R \bar{f}_L$, (b) $e_R^- e_L^+ \to f_L \bar{f}_R$, (c) $e_L^- e_R^+ \to f_L \bar{f}_R$ and (d) $e_L^- e_R^+ \to f_R \bar{f}_L$. Spin state for each particle is shown by a hatched arrow. The angle between the outgoing fermion and the direction of the electron traveling is defined as θ. Difference in the cross sections for each event type gives net outgoing fermion and antifermion polarizations. The difference is due to the difference in the strength of the couplings of the Z^0 boson to right- and left-handed fermions.

By introducing the following two coupling constants, c_R^f and c_L^f, for the right- and left-handed fermions to the Z^0:

$$\begin{aligned} c_R^f &\equiv c_V^f - c_A^f \quad \text{and} \\ c_L^f &\equiv c_V^f + c_A^f, \end{aligned} \qquad (2.8)$$

8

the differential cross sections, $\dfrac{d\sigma^{f_R}}{d\cos\theta}$ and $\dfrac{d\sigma^{f_L}}{d\cos\theta}$ are obtained by substituting $c_L^f = 0$ and $c_R^f = 0$ in the differential cross section (2.6), respectively.

Figure 2.3 shows the polarization (2.8) as a function of center-of-mass energy E_{cm} for several values of electron polarization $\mathcal{P}$ and $\cos\theta$. The polarization of the outgoing fermions $\mathcal{P}_f$ strongly depends on E_{cm} and its absolute value reaches a maximum around the Z^0 mass region. The polarization becomes smaller as E_{cm} goes away from the Z^0 pole. Thus, analysis of e^+e^- annihilations at the Z^0 pole allows us to study the spin effects at the maximum quark polarization.

Using relations (2.9), the differential cross section (2.6) at the Z^0 pole is written by using c_R and c_L:

$$
\left.\frac{d\sigma(e^+e^- \to f\bar{f})}{d\cos\theta}\right|_{c.m.} = N_c k \left[\frac{1}{2}\left(\frac{1+\mathcal{P}}{2}c_R^{e\,2} + \frac{1-\mathcal{P}}{2}c_L^{e\,2}\right)(c_R^{f2}+c_L^{f2})(1+\cos^2\theta) \right.
$$
$$
\left. - \left(\frac{1+\mathcal{P}}{2}c_R^{e\,2} - \frac{1-\mathcal{P}}{2}c_L^{e\,2}\right)(c_R^{f2}-c_L^{f2})\cos\theta \right]. \quad (2.9)
$$

The differential cross sections in Equation (2.8) are written:

$$
\frac{d\sigma^{f_R}}{d\cos\theta} \propto (1-A_f)(1+\cos^2\theta + 2A_Z\cos\theta)
$$
$$
\frac{d\sigma^{f_L}}{d\cos\theta} \propto (1+A_f)(1+\cos^2\theta - 2A_Z\cos\theta) \quad (2.10)
$$

where A_f is written:

$$
A_f \equiv -\frac{c_R^{f2} - c_L^{f2}}{c_R^{f2} + c_L^{f2}} = \frac{2c_V^f c_A^f}{c_V^{f2} + c_A^{f2}}, \quad (2.11)
$$

and is listed in Table 2.1 for various fermions. A_Z is the polarization of the Z^0 bosons multiplied by -1:

$$
A_Z \equiv \frac{A_e - \mathcal{P}}{1 - A_e\mathcal{P}}. \quad (2.12)
$$

From Equations (2.11), (2.12) and (2.13), the polarization of the outgoing fermions coupled to the Z^0 (2.8) is given by:

$$
\mathcal{P}_f(\mathcal{P}, \cos\theta) = -\frac{A_f(1+\cos^2\theta) + 2A_Z\cos\theta}{1+\cos^2\theta + 2A_ZA_f\cos\theta}. \quad (2.13)
$$

2.2   Polarization in Quantum Chromodynamics

The polarization of outgoing fermions is described as the cross section asymmetry in $e^+e^- \to f\bar{f}$ as shown in the previous section. If the fermions f, is a quark or
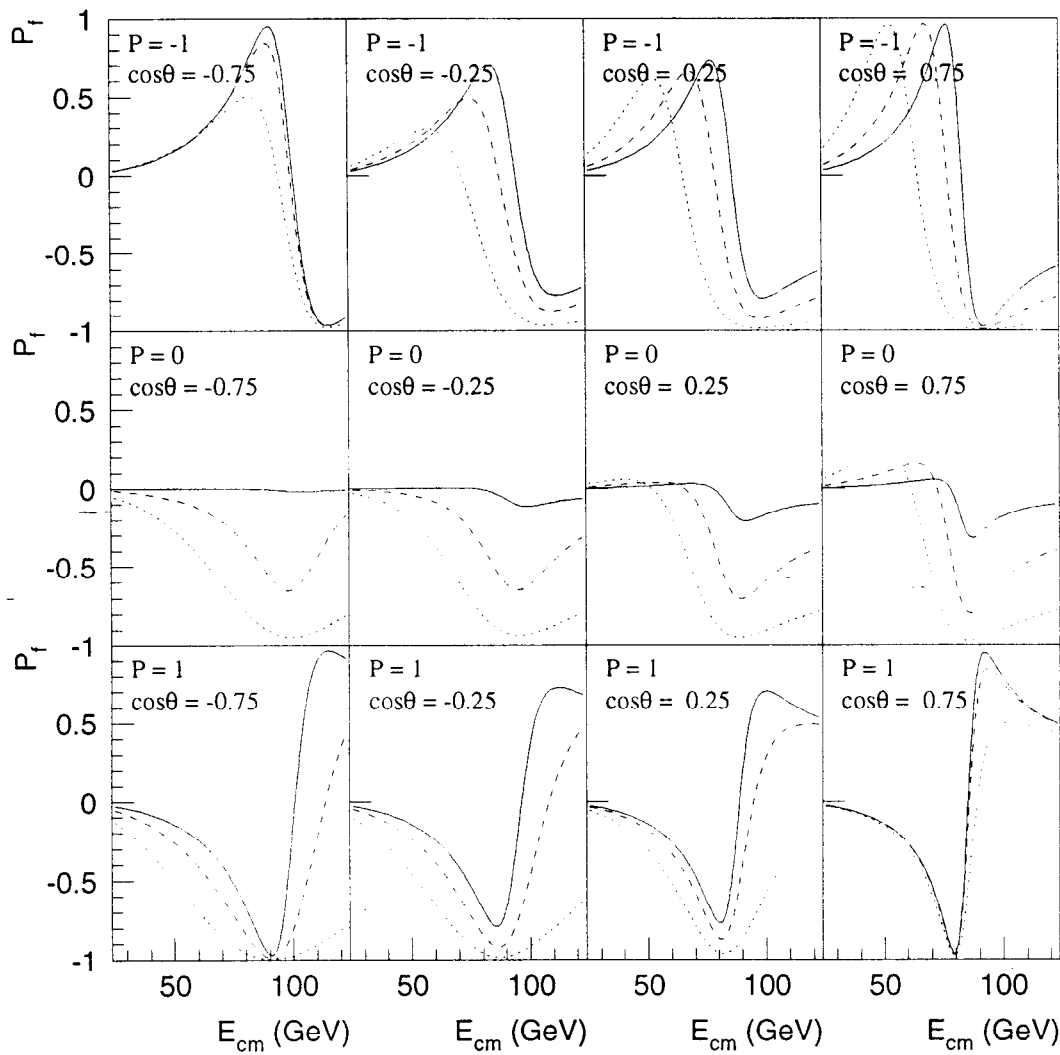
Figure 2.3: The polarization $\mathcal{P}_f$ as a function of $\mathcal{P}$, $\cos\theta$ and E_{cm}. Solid, dashed and dotted curves show the $\mathcal{P}_{e,\mu,\tau}$, $\mathcal{P}_{u,c}$ and $\mathcal{P}_{d,s,b}$, respectively. The electron beam polarization $\mathcal{P}$ and $\cos\theta$ for each case are shown in the figure.
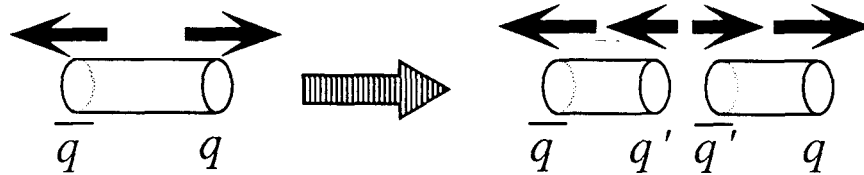
Figure 2.4: Schematic pictures of behaviors of quark and antiquark and color flux tubes in the string model.

antiquark, we only observe hadrons in final state. This process is called *hadronization* or *fragmentation* and is described by Quantum Chromodynamics (QCD) in principle. However, it is not obvious how the spin or helicity of quark and antiquark is transported to the final state hadrons, since the hadronization process is not completely calculable in QCD yet.

In this section, a model of hadronization is explained. The hadronization model, however, does not take into account the process of the transport of quark or antiquark spin.

Hadronization Model

The QCD describes phenomena well in a high energy region where the coupling constant of the strong interaction, α_s, is small enough to apply perturbation theory. However, perturbative QCD can not be applied to phenomena in a low energy region where the coupling constant becomes large. One of the typical phenomena which occur in such a low energy region is the hadronization of quarks and antiquarks. The behavior of quarks and antiquarks through the hadronization is difficult to solve. Therefore, only phenomenological models are proposed to describe what happens in the process.

Typical hadronization models are the independent fragmentation model[14], the cluster fragmentation model[15] and the string model[16]. All of them describe the hadronization phenomenologically.

Among them, the Lund string model[16] is a widely used model. In the following, the basic dynamical picture of this model is explained with help of Figure 2.4: When two colored quarks are separated, a color flux tube is stretched between them. This flux tube is modelled by a relativistic massless (one dimensional) string with a string constant of $\kappa \approx 1$ GeV/fm to simulated a linear confinement force. In the string picture, one end of the string corresponds to a quark and the other end to an antiquark, while gluons are represented by excitations or "kink"s in the string. While

the string evolves, it breaks up into color $q\bar{q}$ two singlets; this rate of break-up is calculated from a semiclassical model of fermion pair tunnelling from the vacuum. The energy carried off by the daughter singlets at each break-up is well determined by the 'left-right' symmetry principle. This principle states that the final particle distributions should be blind to the order in which causally disconnected break-ups happen. Assuming a parton, which means quark, antiquark or gluon, splitting $A \to B + C$, z is defined as:

$$z \equiv (E + p_{//})_B / (E + p_{//})_A \qquad (2.14)$$

where E and $p_{//}$ are energy and the longitudinal momentum along the parent parton direction, respectively. For the Lund string model, the fragmentation function, which is the probability of the splitting with z, is given by:

$$f(z) = \frac{N}{z}(1 - z)^a \exp\left(-\frac{bm_t^2}{z}\right), \qquad (2.15)$$

where N is the normalization factor, and a and b are the constants to be determined from experiment. m_t is the transverse mass of the final state hadron with mass m and transverse momentum, p_t: $m_t^2 = m^2 + p_t^2$. This iterative break-up of the string into hadrons stops when the mass of the string fragments reaches a hadronic scale. The transverse momentum distributions for hadrons can be taken into account by adding another parameter.

Events generated by Monte Carlo simulations in which this model is implemented reproduce real data such as momentum distribution of tracks and number of charged tracks in an event well. However, this string model does not take into account the effect of the spin or helicity of quarks and antiquarks. Therefore, information on the spin and helicity of each particle is not obtainable from the Monte Carlo simulation. At present, we can not predict the polarization of quarks and antiquarks in final state jets from any of the Monte Carlo simulations.

2.3   Jet Handedness

A quantity related to the polarization of quarks and antiquarks underlying jets was first proposed in ref. [1] in 1977 in which no prediction of the magnitude was presented.

In 1988, Dalitz *et al.*[2] calculated another quantity related to the polarization of charm quarks in $c \to D + \pi + hadrons$ and gave the value of order of 10^{-4}. However, the value depends on the model describing the decay of c quarks.

The experimental study of "jet handedness"[2] in e^+e^- annihilations was first

---

[2]The term of "jet handedness" was defined in [3].

(a) Laboratory Frame   (b) 3-π Rest Frame
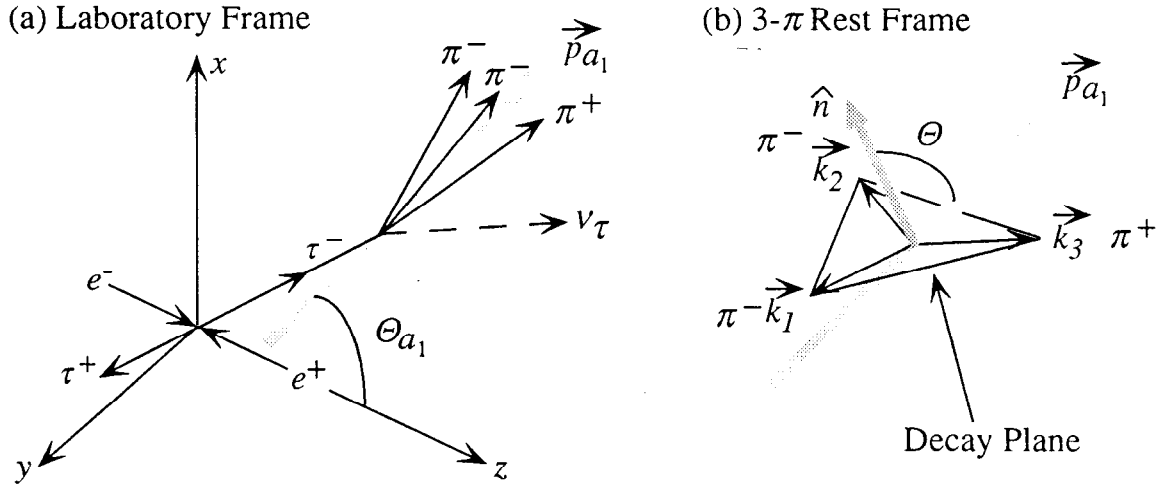
Figure 2.5: Schematic view of $\tau^- \to a_1^- \nu_\tau \to \pi^- \pi^- \pi^+ \nu_\tau$ shown both in (a) laboratory frame and (b) 3-π rest frame.

suggested in 1992[3], because of high quark polarization at the Z^0 predicted by the standard model. In the following, the concept of jet handedness is discussed.

2.3.1 τ polarization in $\tau \to \pi\pi\pi\nu_\tau$

The analysis method to find the quark spin transport in jets is not known apriori. One possible method[3] can be obtained from the hadronic 3-π decay of a τ lepton:

$$\tau^- \longrightarrow a_1^- \ \nu_\tau$$
$$\longmapsto \rho^0 \ \pi^-$$
$$\longmapsto \pi^- \ \pi^+$$

for which several theoretical works calculated the τ polarization[4]–[6], [17]. The estimates using the properties of the weak axial current and the hadronic current gave reasonable agreement with the data [18], [19]. Therefore, we will discuss the τ polarization according to ref. [6].

Figure 2.5 shows coordinate systems of the 3-prong decay of τ^- via an a_1 meson produced in $e^+ e^-$ annihilation. Momenta of $\vec{k}_1, \vec{k}_2$ and $\vec{k}_3$ are assigned to two pions with negative charge and a pion with positive charge, respectively, in the 3-π rest frame. $\vec{k}_1$ or $\vec{k}_2$ is assigned to each of two negative pions at random. A vector normal

to the decay plane of a_1, $\hat{n}$ is defined by:

$$\hat{n} \equiv \frac{\vec{k}_1 \times \vec{k}_2}{|\vec{k}_1 \times \vec{k}_2|}. \tag{2.16}$$

Using $\hat{n}$, a τ polarization observable, $\cos\Theta$ is defined by:

$$\cos\Theta = \vec{p}_{a_1} \cdot \hat{n}, \tag{2.17}$$

where $\vec{p}_{a_1}$ is a unit vector pointing to the direction of 3 πs boosted, *i.e* the unit vector of momentum of a_1 in the laboratory frame. Asymmetric distribution gives the τ polarization as follows:

$$\mathcal{H} = \frac{N(\cos\Theta(s_1 - s_2) > 0) - N(\cos\Theta(s_1 - s_2) < 0)}{N(\cos\Theta(s_1 - s_2) > 0) + N(\cos\Theta(s_1 - s_2) < 0)}, \tag{2.18}$$

where N is the number of events observed with the criteria in the parenthesis, and $s_1 = (k_1 + k_3)^2, s_2 = (k_2 + k_3)^2$ are squared invariant masses. According to [6], $\mathcal{H}$ is proportional to the τ polarization:

$$\mathcal{H} = \alpha\mathcal{P}_\tau \tag{2.19}$$

where $\mathcal{P}_\tau$ is the polarization of τ leptons and α is an analyzing power for this method.

2.3.2 Definition

Handedness for the quark and antiquark polarization in a jet was called "jet handedness" [3] and can be defined in analogy with the decay of $\tau \to \pi\pi\pi\nu_\tau$ [6]. Since quark and antiquark go to hadrons through strong interactions, the decay amplitude must be invariant for parity operation. This requires one to choose an observable which conserves parity. Taking the analogy with Equation (2.18), the following observable, Ω is introduced as the simplest quantity which may carry helicity of quark or antiquark:

$$\Omega \equiv \hat{t} \cdot (\vec{k}_1 \times \vec{k}_2), \tag{2.20}$$

where $\vec{k}_1$, $\vec{k}_2$ are the momenta of two particles in a jet. $\hat{t}$ is the jet axis which represents a unit vector of momentum of an underlying quark or antiquark. A selection of tracks and ordering of momenta $\vec{k}_1, \vec{k}_2$ depend on analyses to be performed. In this study, tracks with higher momentum are usually selected, because those tracks are expected to carry information on helicity of quark and antiquark. A detailed explanation of the selection method and the ordering will be given in the following two sections and in Chapter 4. Ω is calculated for each jet individually. A jet with a negative (positive)

value of Ω is called a "left-handed" ("right-handed") jet. Jet handedness H is defined as:

$$H \equiv \frac{N_L - N_R}{N_L + N_R} \tag{2.21}$$

where N_L, N_R are the numbers of left- and right-handed jets, respectively. Jet handedness is a statistical observable and is not to measure the helicity of an individual quark or antiquark underlying a jet.

A probability that a left- or right-handed quark produces a left- or right-handed jet is defined as:

$$P(q_L \to \Omega < 0) = P(q_R \to \Omega > 0) \equiv \frac{1}{2}(1 - \alpha) \tag{2.22}$$

where α is the "analysing power" and takes a value between -1 and 1. On the other hand, a probability for a left- or right-handed jet coming from right-, left-handed quark is also defined as:

$$P(a_R \to \Omega < 0) = P(a_L \to \Omega > 0) \equiv \frac{1}{2}(1 + \alpha) \tag{2.23}$$

The probabilities are considered for antiquarks independently, but in this study they are assumed to be identical as those for quarks.

For a sample containing n_L left- and n_R right-handed quarks and antiquarks, jet handedness (2.22) is given from the probabilities by:

$$
\begin{aligned}
H &= \frac{N_L - N_R}{N_L + N_R} \\
&= \frac{1/2(1 - \alpha)n_L + 1/2(1 + \alpha)n_R - 1/2(1 + \alpha)n_L - 1/2(1 - \alpha)n_R}{n_L + n_R} \\
&= \alpha \frac{n_R - n_L}{n_R + n_L} \\
&= \alpha \mathcal{P}_p, \tag{2.24}
\end{aligned}
$$

where $\mathcal{P}_p$ is a polarization of quarks and antiquarks in the sample. The analyzing power will strongly depend on the selection method and ordering of the two particles used in the analysis procedure. Optimization to get a large value of the analyzing power is important to observe the evidence for jet handedness.

2.3.3   Jet Handedness in e^+e^- Annihilations

As mentioned in the previous section, the ordering of particles is important in order to get a large value of the analyzing power. The polarization also depends on the ordering. In the present study, we used three methods for the ordering of two momenta, $\vec{k}_1$ and $\vec{k}_2$, in the Ω definition (2.21):

- "Helicity-based" analysis, where the momenta are ordered according to their the magnitudes,

- "Modified helicity-based" analysis, where the momentum ordering is arbitrary, but the sign of the vector product in the Ω definition is defined by two invariant masses, and

- "Chirality-based" analysis, where the momenta are ordered according to the particle charges.

In this section, definitions of the polarization for these are described briefly. A detailed description of the polarization for both analyses is given in Appendix A.

Helicity-based Analysis

'Helicity-based' polarization is defined at a given $\cos\theta$ by using the differential cross sections (2.11):

$$\mathcal{P}_{hel} \equiv \frac{\sigma_R^f + \sigma_R^{\bar{f}} - \sigma_L^f - \sigma_L^{\bar{f}}}{\sigma_R^f + \sigma_R^{\bar{f}} + \sigma_L^f + \sigma_L^{\bar{f}}} = -2\frac{A_Z\cos\theta}{1+\cos^2\theta}, \tag{2.25}$$

where σ_R^f, σ_L^f are abbreviations of $\dfrac{d\sigma_R^f}{d\cos\theta}$, $\dfrac{d\sigma_L^f}{d\cos\theta}$ in Equation (2.11), respectively. The helicity of the fermion and antifermion in an e^+e^- annihilation event are always of opposite sign, because the antifermion always goes in the opposite direction to the fermion. Therefore, the replacements $R \to L, L \to R$ and $\cos\theta \to \cos(\pi - \theta)$ in the differential cross sections (2.11) give the following cross sections $\sigma_R^{\bar{f}}$, $\sigma_L^{\bar{f}}$:

$$\sigma_R^{\bar{f}}(\cos\theta) = \sigma_L^f(\cos(\pi - \theta)),$$
$$\sigma_L^{\bar{f}}(\cos\theta) = \sigma_R^f(\cos(\pi - \theta)).$$

Figure 2.6 shows the polarization, $\mathcal{P}_{hel}$ as a function of $\cos\theta$ for $\mathcal{P} = 0$ and ± 0.63[3]. The polarization is independent of quark flavor, and reaches ∓ 0.72 and ± 0.52 at $\cos\theta = \pm 1$ for beam polarization of -0.63 and $+0.63$, respectively.

The Ω corresponding to the definition (2.21) is taken to be:

$$\Omega_{hel} \equiv \hat{t} \cdot (\vec{k}_1 \times \vec{k}_2) \tag{2.26}$$

where the momenta $\vec{k}_1, \vec{k}_2$, of two particles chosen from a jet are ordered to be $|\vec{k}_1| > |\vec{k}_2|$ and $\hat{t}$ is the jet axis. The methods for selection of tracks are described in Section 2.3.4.

---

[3]The electron polarization of 0.63 is the average value in the 1993 SLD run[20].
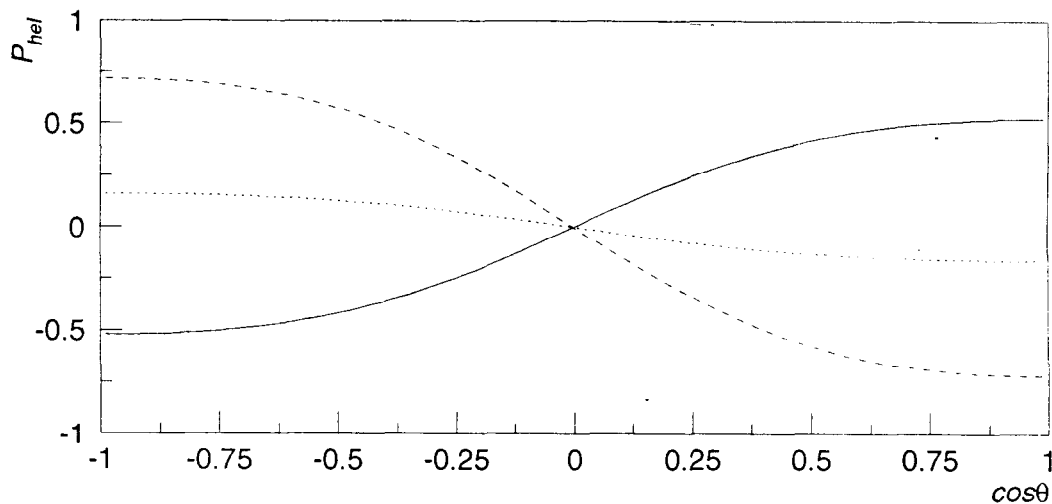
Figure 2.6: $\mathcal{P}_{hel}$ as a function of $\mathcal{P}$ and $\cos\theta$. Solid, dotted and dashed curves show $\mathcal{P}_{hel}$ for $\mathcal{P} = +0.63$, 0 and -0.63, respectively.

Modified Helicity-based Analysis

The 'modified helicity-based' Ω is the same observable used in Equation 2.19. In this analysis, Ω is defined for three particles with total charge equal to ± 1. When one selects three particle a, b, which have the same charge, and c, whose charge is opposite to that of a or b, $\Omega_{mod.hel}$ is defined as:

$$\Omega_{mod.hel} = \hat{t} \cdot (\vec{k}_a \times \vec{k}_b)(s_a - s_b) \tag{2.27}$$

where $\vec{k}_a, \vec{k}_b$ are the momenta of particles with same charge in the 3-particle rest frame, and $s_a = (k_a + k_c)^2$, $s_b = (k_b + k_c)^2$ are squared invariant masses. $\hat{t}$ is the jet axis. The corresponding polarization is the same as the helicity-based polarization:

$$
\begin{aligned}
\mathcal{P}_{mod.hel} &= \mathcal{P}_{hel} \\
&= -2\frac{A_Z \cos\theta}{1 + \cos^2\theta}.
\end{aligned}
\tag{2.28}
$$

Chirality-based Analysis

The 'chirality-based' polarization of underlying quarks and antiquarks is defined as:

$$\mathcal{P}^f_{chi} \equiv \frac{\sigma^f_R - \sigma^{\bar{f}}_R - \sigma^f_L + \sigma^{\bar{f}}_L}{\sigma^f_R + \sigma^{\bar{f}}_R + \sigma^f_L + \sigma^{\bar{f}}_L} = -A_f, \tag{2.29}$$

where A_f is given by Equation (2.12). Thus, this polarization is independent of $\cos\theta$ but depends on quark flavor. The Ω for this case is given by:

$$\Omega_{chi} \equiv \hat{t} \cdot (\vec{k_+} \times \vec{k_-}), \tag{2.30}$$

where $\hat{t}$ is the jet axis, and the momenta $\vec{k_+}, \vec{k_-}$ for positive and negative particles, respectively, are ordered as given in Equation (2.31). Methods for selection of tracks are described in the following section. This form of the triple vector product is taken such that a quark jet gives the same sign of Ω_{chi} as an antiquark jet with opposite helicity. In general, the chirality-based polarization is given by:

$$\mathcal{P}_{chi} = -\sum_f s_f R_f A_f \tag{2.31}$$

where s_f is sign of charge of a quark f and R_f is the fraction of $f\bar{f}$ events in a sample of hadronic Z^0 decays. Equation (2.32) will be used later to obtain explicit values for $\mathcal{P}_{chi}$ given in Table 4.3 in Section 4.4.

2.3.4   Selection of Tracks from a Jet

Two tracks used in the definition of Ω are selected from tracks in a jet. The selection of tracks depends on assumptions of the origin of jet handedness.

This study is motivated by two models. One of the assumptions ascribes the origin of jet handedness to similar phenomena to the τ polarization. The other assumes that jet handedness is caused by fragmentation phenomena.

Selection Based on the Analogy with τ Polarization

In the analogy with the τ polarization, we assume that a light flavor quark q such as u or d, goes to 3 πs (plus another quark, q') as a result of the hadronization, *i.e.* $q \rightarrow \pi\pi\pi q'$. The most plausible decay of the quark q is to pass through the a_1 and ρ resonances. There are two decay modes for a_1 meson which interfere with each other like 3-prong decays of τ leptons as shown in Figure 2.7. If the helicity of the quark or antiquark in $Z^0 \rightarrow q\bar{q}$ is transported to the a_1 meson, we can observe jet
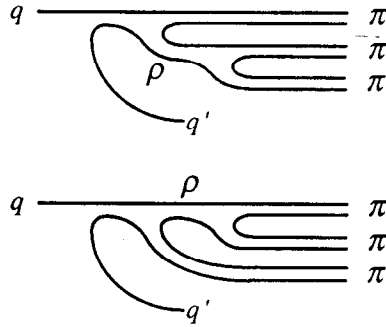
Figure 2.7: Naive models of $q \to \rho \pi q' \to \pi \pi \pi q'$.

handedness in a similar analysis as for the τ polarization. One can expect also that the leading particles in a jet carry helicity information of a quark or antiquark in $Z^0 \to q\bar{q}$. From the above view points, we select a set of three highest momentum tracks from a jet and require that three tracks have a total charge equal to $+1$ or -1 and invariant mass in a region of a_1 mass. In addition, we require that at least one of the two particle invariant masses with zero charge is in the region of the ρ^0-mass, where all particles are assumed to be π. The momenta in the 3-selected-particle rest frame are used to calculate Ωs from (2.27) and (2.31).

Selection based on Fragmentation Phenomena

Ryskin[8] introduced "color magnetic" field $\vec{H}$ as well as "color electric" field which is ordinary color field. This assumption is an analogy with electromagnetism. Figure 2.8 shows a schematic view of the string model modified by Ryskin. He assumed that $\vec{H}$ was generated by the spin of the quark $\vec{\sigma}$ and was parallel to $\vec{\sigma}$, $\vec{H} \| \vec{\sigma}$. When a color string becomes long enough during the fragmentation process, the string is broken and a new quark-antiquark pair is produced at both ends. At the beginning, transverse momenta of new quark and antiquark with respect to the initial string are balanced. However, moving in the color-magnetic field they get an additional momentum ($\delta \vec{k}_t$ and $-\delta \vec{k}_t$ shown in the figure). This momentum kick is of. the order of a few ten MeV/c[8] and these momenta, $\delta \vec{k}_t$ and $-\delta \vec{k}_t$ contain information on the helicity of the initial quark or antiquark.

We can only observe the hadron momenta, not the additional momentum $\delta \vec{k}_t$. Therefore, based on this assumption, we look for angular correlation of two particles from the same string break up in order to get nonzero jet handedness. The momenta of two tracks in the laboratory frame are used to get Ωs from (2.27) and (2.31). $\hat{t}$ in
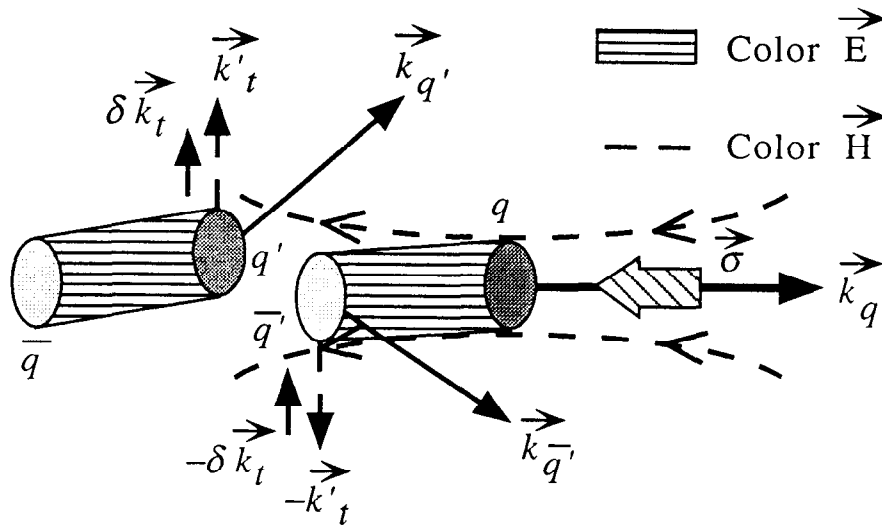
Figure 2.8: Schematic view of the string model modified by Ryskin. He added "color magnetic field" in addition to color flux tube. Due to this field, $q'\bar{q}'$ pair got additional momentum kick $\delta\vec{k}_t, -\delta\vec{k}_t$, respectively.

the Ω definitions (2.27) and (2.31) should be a unit vector of the quark or antiquark momentum. This seems to be represented by the jet axis.

Chapter 3

Experimental Apparatus

The SLAC linear collider (SLC) is located at the Stanford Linear Accelerator Center (SLAC) in Stanford, California. SLC consists of a 3 km long linear accelerator and two arcs which bring the electron and positron beams around to the interaction point (IP). The linear accelerator is the world's longest and accelerates both electrons and positrons in the same straight line up to the energy of 50 GeV.

Due to the single path collider scheme, the SLC can have only one IP. The SLC Large Detector (SLD) is placed at that position. The SLD was designed for general purpose to study, for example, precision tests of the electroweak theory, QCD and heavy flavor physics, etc. In order to accomplish this purpose, the SLD was built and equipped with a state-of-the-art technology for tracking, particle identification and calorimetry systems. In this chapter, characteristics of SLC and SLD are described.

3.1   The SLAC Linear Collider

The SLC consists of a 3 km long linear accelerator, which accelerates both electrons and positrons up to the energy of 50 GeV, and the two arcs, which bring the beams to the interaction point, IP. The schematic view of the SLC is shown in Figure 3.1. In this section, the delivery of the electron and positron beams from an electron source to the IP is described.

The beam collision cycle of the SLC is 120 Hz. In each cycle, two bunches of electrons are produced at an electron source[1]: one of them is delivered to the IP through the linac and the arc, and another serves for positron production at two-

---

[1]There are two sources for electron production: a thermionic source and a polarized source. The polarized source was used in the 1993 run. A detailed description of the source will appear in Section 3.1.1.
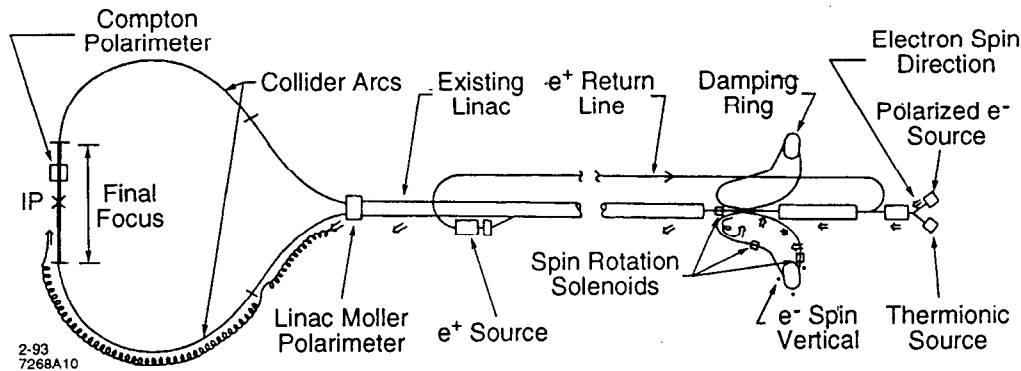
Figure 3.1: The layout of the SLAC linear collider.

thirds down the linac. Positrons are collected from electromagnetic showers produced by injecting 30 GeV electrons onto a target. Those positrons are returned to the beginning of the accelerator and delivered to the IP via the south arc in the same way as electron bunches.

At an energy of 1.2 GeV, both electron and positron bunches are lead to the north and south damping rings, respectively, where the emittance[2] of the bunches is reduced.

After the damping rings , those bunches are returned to the accelerator and accelerated to 46.7 GeV. At the end of the accelerator, they are separated by the bending magnet to be lead into the arcs. During transportation in north and south arcs, the beam lose their energy by about 1 GeV due to synchrotron radiation.

Before reaching the interaction region, the beams go through a series of magnets, called the final focus, in order to compress horizontal and vertical beam sizes down to 2.6 and 0.8 μm, respectively. The electron and positron beams collide with each other at the IP every 8.3 ms(*beam crossing time*).

After passing through the interaction region, the polarization of the electron beam is measured by the Compton polarimeter. Energies of both beams are measured by the wire imaging synchrotron radiation detector (WISRD), before the beams are dumped.

In general, the luminosity of a collider is given by:

$$\mathcal{L} = f_R \times \frac{N^+ N^-}{4\pi \sigma_x \sigma_y} \tag{3.1}$$

where N^+ and N^- are the number of positrons and electrons per bunch, f_R is the

---

[2]Emittance is defined as momentum spread × spatial spread of a bunch.

repetition rate. σ_x and σ_y are the vertical and horizontal spot sizes. Those parameters of the SLC for the 1993 run are shown in Table 3.1. The luminosity of the SLC for the 1993 run had the peak value of $\mathcal{L} = 5 \times 10^{29} \text{cm}^{-2}\text{sec}^{-1}$ equivalent to a rate of about 50 Z^0 events per hour for the observable (neutrino production excluded) cross section of $\sigma(e^+e^- \to f\bar{f}) = 32$ nb at the center of mass energy of 91.26 GeV[21]. The performance of the SLC in the 1993 run was summarized in Table 3.1 together with the design values.

Parameter		Design Value	The 1993 Run
Intensity ($\times 10^{10}$)	$N^+(e^+)$	7	3
	$N^-(e^-)$	7	3
Repetition Rate, f_R (Hz)		180	120
Beam Size (μm)	Horizontal, σ_x	1.6	2.6
	Vertical, σ_y		0.8
Luminosity(Z^0s/hr)		650	50(peak)
e^- Polarization		N/A	63%
Up Time		N/A	70%
Integrated Z^0s		N/A	50000

Table 3.1: Comparison of the SLC parameters for the 1993 run to the design values.

3.1.1 Polarized source

Figure 3.2 shows the schematic layout of the polarized electron source located at the beginning of the accelerator. The polarized source consists of three parts: two YAG-pumped Ti:Sapphire lasers, a series of optical elements to control the intensity, pulse length and circular polarization and an electron source with the photocathode made by strained-lattice gallium arsenide (GaAs) crystal (the polarized gun). The two YAG lasers produce two pulses separated by 60 ns in order to produce two bunches of electrons: one for collision and the other for positron production. Those lasers produce photons with wavelength of 865 nm. The pulses are randomly left- or right-circularly polarized by a circular polarizer in order to reduce systematics, and they are guided to the photocathode in the polarized gun by the optical elements. Finally the pulses are injected to the photocathode with -120kV potential.

When circular polarized photons are injected to GaAs, polarized electrons are emitted[22]. The theoretical limit of the polarization with a normal crystal is 50%. The experimental break through was brought by the use of the strained-lattice crystal. Theoretically, the strained-lattice photocathode can produce 100% polarization. In
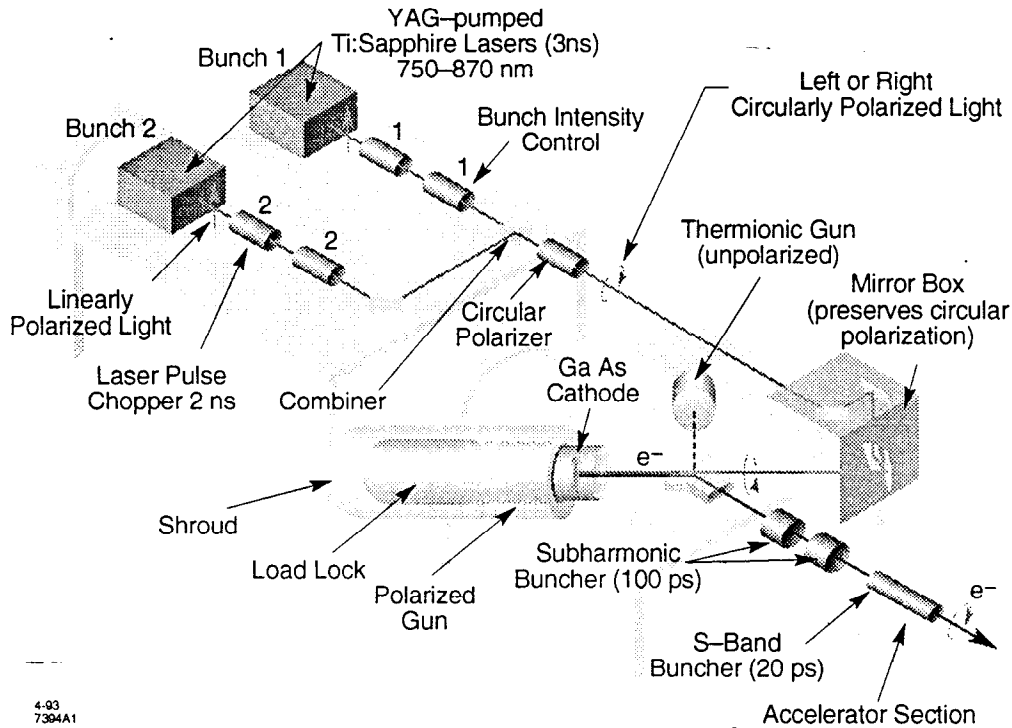
Figure 3.2: The schematic layout of the polarized electron source at the SLC injector. The source consists of the laser, the optical elements and the polarized gun.

practice, the polarization reached about 90% on the test bench[23]. In the 1993 physics run, this strained-lattice crystal was used as the photocathode. The strained lattice crystal consists of $GaAs_{1-x}P_x$ ($x = 0.24$) substrate of thickness 2.5 μm with an eptaxial layer of GaAs of thickness 0.1-0.3 μm. And approximately one atomic layer of cesium and fluorine applied to the surface in order to decrease the work function down to zero or negative and increase quantum efficiency (5%-15%).

3.1.2 Spin Transportation

The electron polarization has to be maintained during the acceleration and delivery to the IP. There are two main sources of depolarization of the electron beam from its source to the IP: in the damping ring and the arc.

Energy spread in the electron bunch leads to incoherent Thomas precession within the bunch in the electromagnetic field if the spin of electrons in the bunch
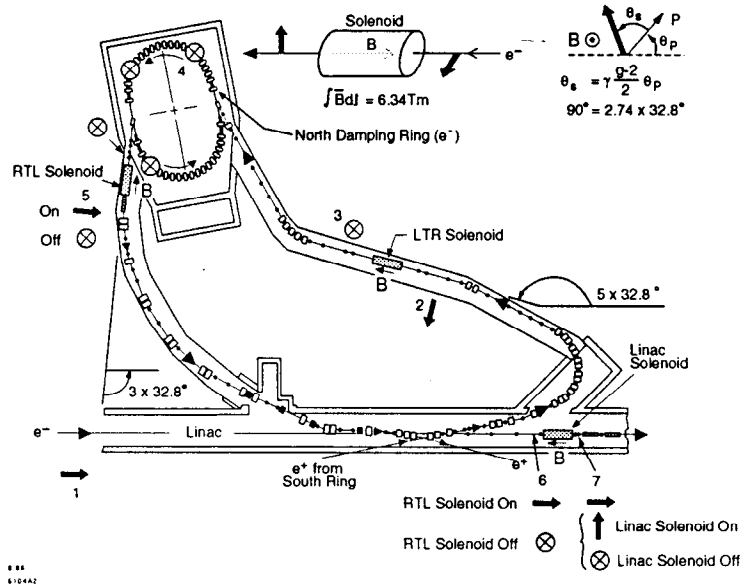
Figure 3.3: The schematic view of the north damping ring. Spin vector at each point is shown by an arrow.

directs along their momenta. This incoherent precession causes depolarization of the electrons. This effect is serious in the damping ring where the electron bunch spends about 8 ms and makes tens of thousands of revolutions. Figure 3.3 shows the schematic view of the north damping ring where emittance of electron buches is reduced.

In order to avoid depolarization of the electron beam in the damping ring, the electron spins are rotated to the vertical direction before being injected into the damping ring, so that there is no horizontal component in the damping ring. This rotation is carried out by one superconducting solenoid called a spin rotator located at the linac-to-ring line. After energy spread in the beam is reduced in the damping ring, the spin vector can be oriented to an arbitrary direction by two spin rotators at the ring-to-linac line and the linac.

Transportation of the electron beam in the arc is controlled by a series of magnets. Therefore, incoherent spin precession due to energy spread causes depolarization of the electron beam. In the 1993 run, electrons were kept polarized vertically in the linac and their spin were rotated longitudinally at the exit of the arc. The estimate of the depolarization was about 1.4 % for a Gaussian energy spread of a0.1.5 % in the beam[24].

3.1.3 Polarimetry

There are two devices to measure the electron polarization: The linac Møller polarimeter and the Compton polarimeter just after the IP. In this section, polarimetry by the two devices and spin transport in SLC are described.

Linac Møller Polarimeter

The linac Møller polarimeter based on Møller scattering $(e^-e^- \rightarrow e^-e^-)$ is set at the end of the linac in the PEP extraction line.This is used for diagnostic measurements of the polarization before the beam enters the north arc. The device measures the polarization asymmetry in the cross section for polarized beam electrons scattered by the electrons in atom of an insertable magnetized iron target. By varying the beam and target polarization, the longitudinal beam polarization is extracted:

$$P_z^{beam} = \frac{A^{meas}}{P_z^{target} A_z} \qquad (3.2)$$

where A^{meas} is the measured Møller asymmetry , P_z^{target} is the longitudinal target polarization, and A_z is the longitudinal Møller asymmetry at the selected momentum.

Due to the location and the method, measurements by this device need a special run in which the electron beam can not be delivered to the IP. The average of several measurements by the polarimeter was $(65.8\pm2.7)\%$[24].

The dominant systematic errors come from the theoretical uncertainty in the estimation of the polarization of the target electron, since atomic effects on the polarization are not completely understood[25].

The Compton Polarimeter

The schematic layout of the compton polarimeter is shown in Figure 3.4. The compton polarimeter is placed at 33m down stream of the SLD and consists of three components: a YAG-pumped Nd laser, a series of optical elements to control intensity, pulse length and circular polarization and a gas Čerenkov counter to detect scattered electrons. The polarization measurement of the device is based on the cross section asymmetry in Compton scattering between a polarized electron and a circularly polarized photon $(e^-\gamma \rightarrow e^-\gamma)$. After the electron beam leaves the IP, it interacts with the circularly polarized photon. The photon is generated by the laser and circularly-polarized by optical elements, then guided to the "Compton" IP. The scattered electron is measured by the Čerenkov detector after being bent by the analysing magnets.
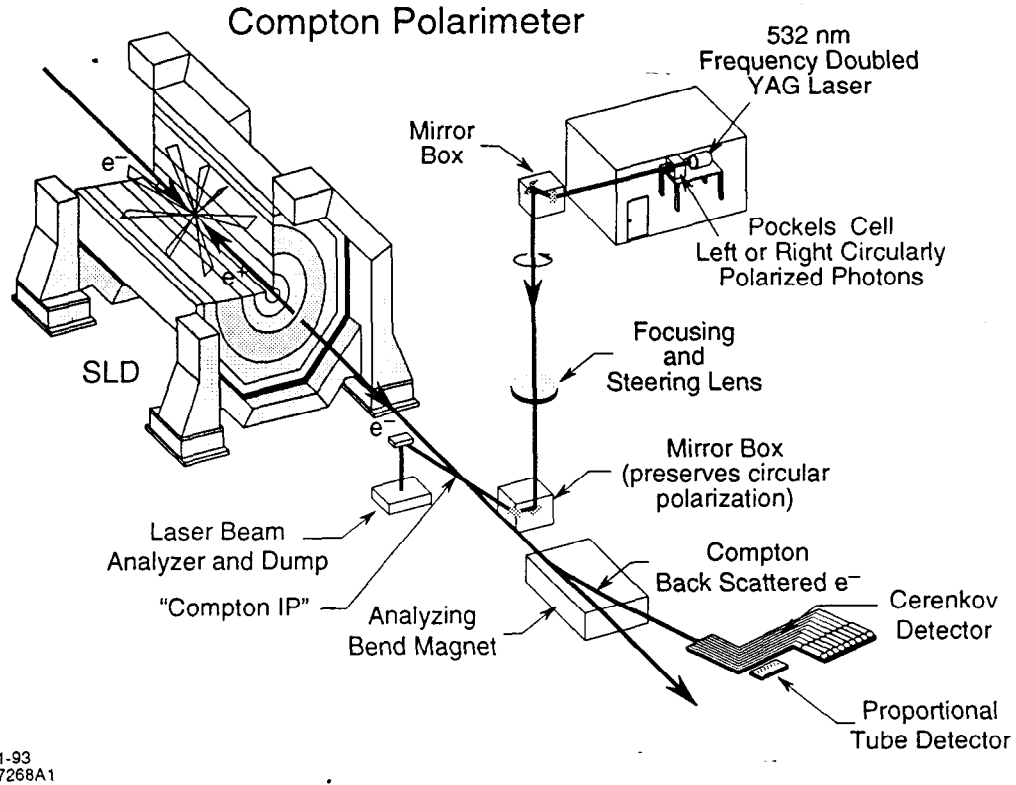
Figure 3.4: The schematic layout of the compton polarimeter. The Compton polarimeter is located at 33 m down stream of the SLD. It consists of the laser, a series of optical elements and a Čerenkov detector.

The cross section for scattering depends on the polarizations of electron and photon as follows:

$$\frac{d\sigma_p}{dE_s} = \frac{d\sigma_u}{dE_s}[1 + P_\gamma P_e A(E_s)] \tag{3.3}$$

where E_s is the energy of the scattered electron, σ_u is the unpolarized compton scattering cross-section, P_γ is the photon spin polarization, P_e is the longitudinal polarization of the electron and $A(E_s)$ is the Compton asymmetry function defined as

$$A(E_s) = \frac{(1/k - 1/k')[\vec{k}\cos\theta_0 + \vec{k}'] \cdot s}{(k - k')^2/kk' + 1 + \cos\theta_0{}^2} \tag{3.4}$$

with $\vec{k}$ and $\vec{k}'$ being the momentum vectors of the incident and scattered photons, respectively and θ_0 the photon scattering angle. In the 1993 run, the average electron polarization measured by the Compton polarimeter was $63.0 \pm 1.0\%$[20].

3.1.4 Energy measurement
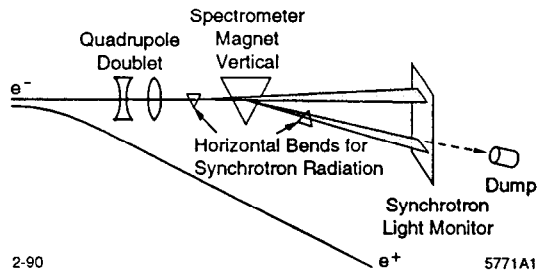
Figure 3.5: Schematic of the wire imaging synchrotron radiation detector for the SLC energy measurement. There are one spectrometer in each of two arcs.

The beam energies are measured by a wire imaging synchrotron radiation detector (WISRD), shown in Figure 3.5,located at just before the beam dump. The WISRD is essentially a deflection spectrometer. Before reaching the WISRD, each beam goes through a series of three dipole magnets in a split-beam configuration. The first magnet induces a horizontal spray of synchrotron radiation that provides a reference pedestal for the bending down stream. The second magnet is a precisely calibrated analyzing dipole which bends the beam 15 meters upstream of the WISRD. The third magnet provided another horizontal stripe of synchrotron radiation. The position of this last stripe is compared to the position of the first one to measure a deflection. The beam energy is then calculated as,

$$E_{beam} = \frac{c}{\theta} \int |\vec{B} \times d\vec{l}| \qquad (3.5)$$

where θ is the measured beam deflection, $\vec{B}$ is the magnetic field in the analysis magnet, and $d\vec{l}$ is the path length along the beam. The synchrotron radiations detected by Compton scattering of the electrons in two screens of copper wires. The measured mean center-of-mass energy for the 1993 run was 91.26 GeV.

3.2 The SLC Large Detector

The SLC Large Detector (SLD) is a general purpose detector to study physics at the Z^0 mass scale. Figures 3.6, 3.7 show the cut and cross sectional views of the SLD.

The construction of the SLD was carried out from 1986 to 1991. The SLD is located in a 15 m deep pit inside the collider hall built on the interaction region of

SLD

Support
Arches

Magnet Coil
Liquid Argon
Calorimeter

Magnet Iron
and Warm Iron
Calorimeter

Moveable Door

e⁻   Čerenkov Ring
Imaging Detector

e⁺

Drift
Chambers

Vertex
Detector   9-88
5731A2
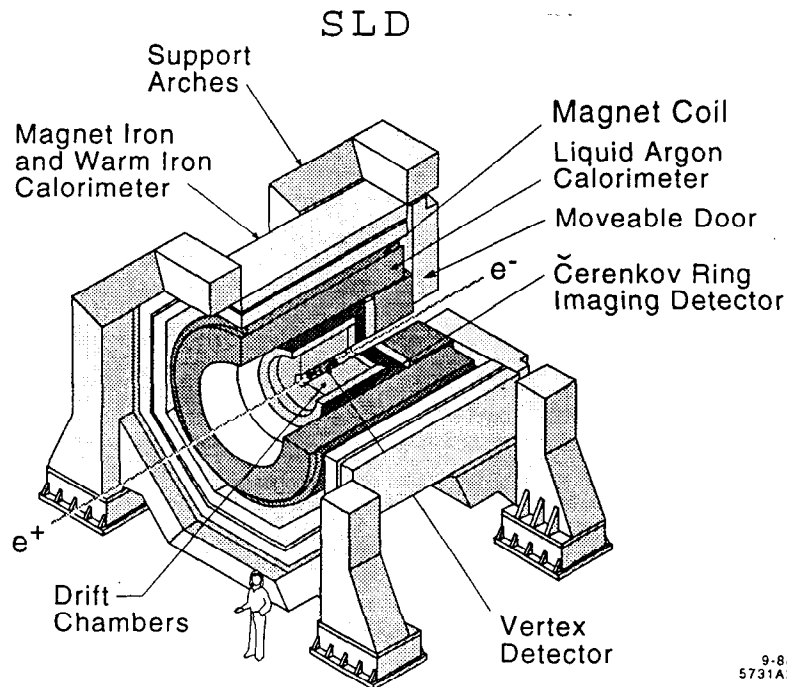
Figure 3.6: A cut view of the SLD. The endcap in the positron arc side is not shown for clarity. The luminosity monitor is also not shown.

the SLC. All detector components are contained in a 9 m diameter octagonal steel structure. The SLD consists of three major subsystems: tracking system, particle identification system and calorimeter system.

A silicon vertex detector (VXD), a precision central drift chamber (CDC) and a set of endcap drift chambers (EDC) for low angle tracks serve for charged particle tracking. Identification of charged particles is done by a set of Čerenkov ring imaging detectors (CRID). Calorimetry is provided by three parts: Liquid Argon Calorimeter (LAC), measuring the electromagnetic part of the energy and the hadronic energy, a Warm Iron Calorimeter (WIC), instrumented with streamer tubes and being also capable to track escaping muons, and a Luminosity Monitor (LUM) which measures energies deposited in the extreme forward and backward directions. All the components, except for the WIC are placed inside a normal magnet coil producing a 0.6 Tesla magnetic field. By measuring the curvature of the charged particle in the magnetic field one can determine its momentum. Platforms all around the detector support the power supplies for each component. A small building on top of SLD, accommodates the fastbus readout electronics (FB) for the data acquisition.

29
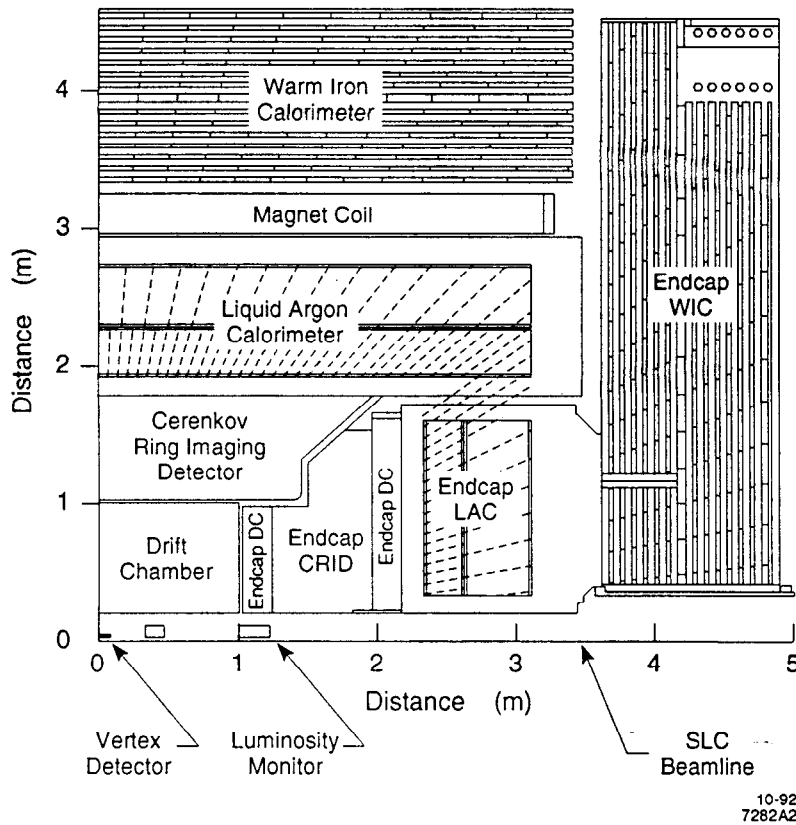
Figure 3.7: A cross-sectional view of the SLD.

3.2.1   The Tracking System

The tracking system consists of the vertex detector and the drift chambers which measure curvatures of charged tracks going through the magnetic field of 0.6 Tesla for the determination of their momenta.

The Vertex Detector

Figure 3.8 shows the Vertex Detector (VXD) which is placed around the beam pipe of 2.5 cm radius surrounding the IP to precisely measure 3-D space points where charged tracks pass through. It provides good reconstruction of secondary vertices. The VXD has 480 silicon charged couples devices (CCDs). Each CCD contains 375 × 578 22μm square pixels and each pixel works independently to detect the space points. The CCDs and their driver electronics comprise a ladder. 4 CCDs are mounted on
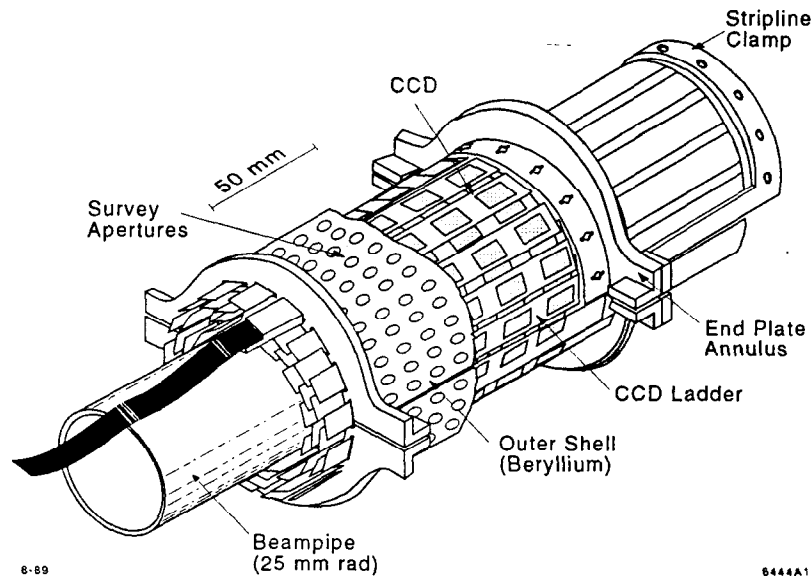
Figure 3.8: A cut view of the vertex detector (VXD).

each side of the ladder. The CCDs on top and bottom sides are slightly overlapping each other to ensure full coverage. 60 ladders are arranged in four concentric layers just outside the beam pipe at radii between 29 and 41 mm.

The VXD is built in a low mass structure ($\sim$ 1.1% of a radiation length par layer) to minimize multiple scattering.

Information from the VXD is useful to distinguish secondary vertices from the primary vertex where electron and positron interacted. The secondary vertices are produced by decay in flight of heavy flavor hadrons with short lifetime and τ leptons. Therefore, the VXD is a powerful tool for study of those particles.

The Drift Chamber system

The barrel and endcap drift chambers provide the position and momentum measurement for charged particles. A set of high voltage wires provides a uniform electric field in a gas filled volume. A charged particle traversing this volume ionizes the gas atoms and the electrons drift with a constant velocity towards the anode. In the high gradient field near the anode wires the electrons avalanche, amplifying the signal. Measuring the drift time and using the known drift velocity, the drift distance can be determined to an accuracy of about 100μm. A track fitting program then
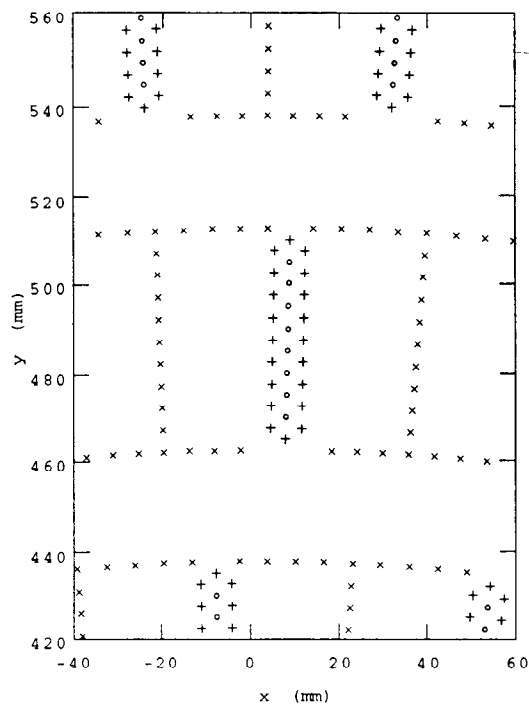
Figure 3.9: Cell structures in the central drift chamber. Shown are the sense wires (circles), field wires (cross symbols) and guard wires (plus symbols).

·reconstructs the trajectory of the track from the space points provided by the drift chamber. The curvature of the track in the magnetic field determines the particle momentum.

Central Drift Chamber   The VXD is surrounded by the central drift chamber. The central drift chamber is 2.0 m long with an inner and outer radius of 0.2 m and 1.0 m, respectively, centered at the IP. The constant drift field is due to a set of field shaping wires and guard wires. Twenty four guard wires and 27 field shaping wires made by gold-coated aluminum are form cell structure shown in Figure 3.9. Each cell contains eight gold-coated tungsten sense wires with 25 μm diameter separated by 5 mm in radial direction. The drift gas consists of CO_2, Ar and Isobutane with constituents of 75 %, 21 % and 4 %, respectively. Doping of $\sim$ 0.2% of water help retard wires aging. The maximum drift distance in any cell is 30 mm. The intrinsic spatial resolution is about 70 μm. The total spatial resolution is, however, degraded to $\sim$ 100μm due to alignment errors in the wires and uncertainty in the drift velocity.

The cells are arranged in 10 concentric superlayers shown in Figure 3.10, provid-
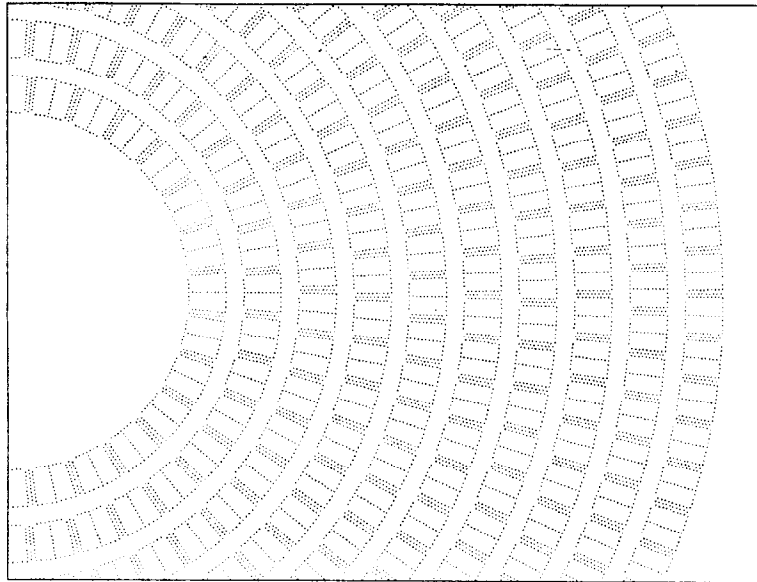
Figure 3.10: The structure of the superlayers in the central drift chamber. From inside to outside (left to right in the figure), the superlayers were arranged in order of *AUVAUVAUVA*, where A, U and V represent for the axial layer and two stereo layers with ±41 mrad stereo angles.

ing up to 80 space points per track. Since the drift cell is symmetric about the sense wires, it is not known which side of the sense wire the electron came from. To resolve the left-right ambiguity, the cells are staggered in each superlayer. An axial layer is set at every third layer with the wire are strung parallel to the beam axis. The rests are small angle stereo layers where the wires were strung at a ±41 mrad stereo angle with respect to the beam axis. From inside to outside, the superlayers are arranged in order of *AUVAUVAUVA*, where *A*, *U* and *V* are represented for the axial layer and two stereo layers with ±41 mrad stereo angles shown in Figure 3.10. The stereo superlayers are also used for determination of a coordinate along the wire together with charge division technique. Each sense wire has identical readout electronics on both sides of the chamber, then a hit point is determined by comparing the outputs in both sides. The charge division determines the coordinate of the hits along the wire to an accuracy of ∼ 6 cm. The position along the beam axis (z axis in the SLD coordinate system) is better determined by hits in stereo layers.

Endcap Drift Chamber   The track momentum resolution of the CDC drops off at angles of less than 30° with respect to the beam axis, since the number of hits on sense wires decreases in this region. To improve the resolution in this region, two sets of drift chambers, the Endcap Drift Chambers (EDC) were set at each of endcap.

The EDC of each side consists of two drift chambers, inner and outer, located at 1.2 m and 2.0 m away from the IP and covers the region between 12° and 40°. Each of the four drift chambers has three superlayers with a relative rotation of 60°.

The Magnet

The magnet[3] is a 5.9 m diameter and 6.4 m long coil situated between the LAC and the WIC. A current of 6600 A through 508 turns provides a magnetic field of 0.6 Tesla in the center of the coil. The iron structure of the WIC on the doors and the barrel serves as flux return[4]. The Poisson-parametrization of the magnetic field in the coil:

$$B_r = B_r^0 \frac{rz}{r_0 z_0}$$

$$B_z = B_z^0 + 0.5 B_r^0 \frac{r^2 - 2z^2}{r_0 z_0}$$

where $B_r^0 = 0.0214T$, $B_z^0 = 0.601T$, $r_0 = 1.2m$ and $z_0 = 1.5m$ agrees with the measured field to within 0.05% inside the volume of the CDC and to within 0.4% for the EDC. The uniformity of the field is more than adequate for the tracking measurements and the radial component of the field is small enough for the requirements of the CRID.

Tracking Performance

The raw hits from the VXD and the drift chambers are used for the track reconstruction divided into two steps: pattern recognition in the drift chambers and linking of the hits in the VXD and the track found in the drift chamber.

Figure 3.11 shows a schematic illustration of the reconstruction of a track in the CDC. At first, two track segments for each cell are reconstructed by χ^2 fitting of those segments to 8 hits of the sense wires in a cell[5]. Those segments are called *vector hits*. Then the vector hits are fitted to a track. Charge division is used for pattern recognition, however, final track fitting uses only the information from vector hits.

The hits in the VXD are clustered by pattern recognition with a loose constraint on the primary vertex in advance of the extrapolation of the track found in the drift chambers. Those tracks are extrapolated into the VXD and linked to clusters in the

---

[3]The magnet was manufactured by Mitsubishi Heavy Industry Company.

[4]The magnet yoke was manufactured by Kawasaki Heavy Industry Company.

[5]The two segments are due to left-right ambiguity of the position where a track really passed through.
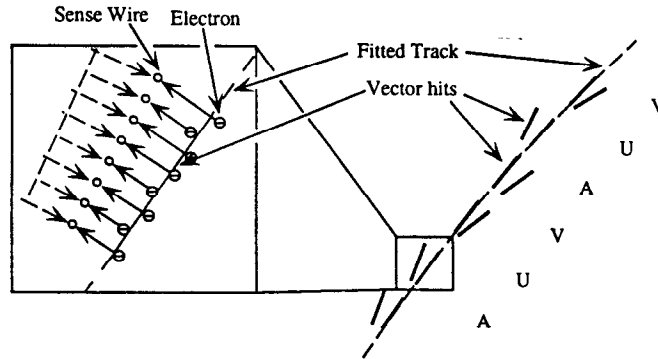
Figure 3.11: The schematic illustration of the reconstruction of a track in the CDC. Solid arrows in the left figure show the drift paths of electrons from ionization of a charged track, dashed arrows are mirror images of the real drift paths.

VXD. Each cluster is allowed to be associated with one extrapolated track. Then a combined track fit is performed using the Billoir method[26] taking into account the track multiple scattering in the detector material.

The CDC with a magnetic field of 0.6 Tesla has a the momentum resolution of[27]:

$$\frac{\sigma_p}{p} = \sqrt{0.0095^2 + (0.0049p \ (\text{GeV/c}))^2}$$

where p is the momentum of a track in GeV/c. For the combined CDC and VXD track, the momentum resolution is[27]:

$$\frac{\sigma_p}{p} = \sqrt{0.0095^2 + (0.0026p \ (\text{GeV/c}))^2}.$$

The combination of the CDC and VXD improves the resolution significantly.

3.2.2 The Particle Identification System

The Čerenkov Ring Imaging Detector

The Čerenkov Ring Imaging Detector(CRID) shown in Figure 3.12 is used for particle identification and flavor tagging. When a charged particle passes through a medium, exceeding the speed of light in the medium, the atoms get polarized and emit photons (Čerenkov radiation). The opening angle of the light cone with respect
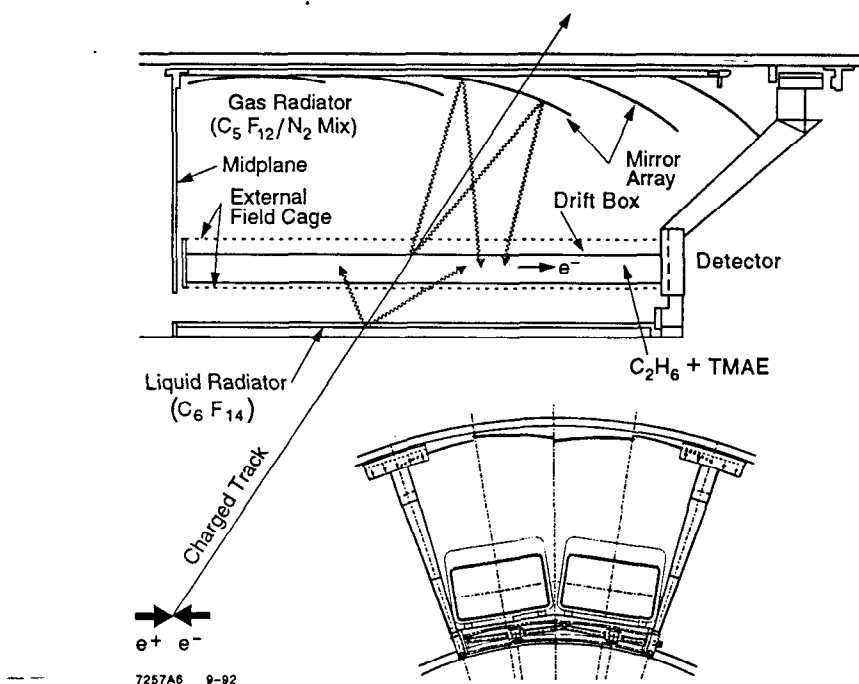
Figure 3.12: Two cross-sectional views of the barrel Čerenkov ring imaging detector (barrel CRID). Wavy lines show the traces of Čerenkov photons. The photons are converted to electrons in the drift box by TMAE.

to the incident track, θ_C is related to the velocity and an index of refraction of the medium, n as follows: $\cos\theta_C = 1/(\beta n(\lambda))$, where β is the ratio of the velocity to the speed of light. The index of refraction depends on the wavelength of a photon, λ. If the angle θ_C is measured, one can determine the velocity of the particle. Together with a momentum measurement of the particle, the mass and hence the type of the particle can be determined: $m = p\sqrt{(n\cos\theta_C)^2 - 1}$.

The CRID consists of three main parts: liquid radiator, time projection chambers (TPCs) to detect photons and gas radiator and spherical mirrors to reflect the photons to the TPC, Figure 3.12 shows the barrel CRID, the emission of the Čerenkov photons and how to detect them. At first, the particle from the IP passes through a thin layer(10 mm) of liquid radiator which is Freon (F_6C_{14}) with an index of refraction $n = 1.277$. For $\beta = 1$, the Čerenkov angle of the photons is 672 mrad. The photons are mainly emitted at frequencies in the near ultraviolet (UV) region(170-220 nm), therefore the outer side of the radiator vessel is made of quartz glass, which is transparent to the UV light. Typically about 12-15 photoelectrons, which will be defined below, are expected for a particle of $\beta = 1$. After being refracted at the quartz

window by 236 mrad, the photons pass across the 13 cm gap to the TPC at an angle of 52 mrad with respect to the incident particle trajectory, forming a circle of 17 cm radius and about 1.5 cm width.

The outer side of the TPC is filled with 76 % of F_5C_{12} as gas radiator and 24 % of nitrogen. The gas radiator has a low index of refraction of $n = 1.0017$ and is transparent to UV light. The gas radiator thickness of ~ 45 cm expects 7-9 photoelectrons. Those photons are emitted at an angle θ_C of ~ 53 mrad for a track with $\beta = 1$. The photons are reflected and focused back onto the outer side of the TPC by a set of spherical mirrors mounted on the outer wall of the CRID vessel.

A time projection chamber (TPC) is used to detect the Čerenkov light. The drift volume is filled with ethane saturated with TMAE(Tetrakis Dimethyl Amino Ethane), which converts the Čerenkov photon to an electron with a very high quantum efficiency in the wave length range of 170 to 220 nm. The photons enter the driftbox from the top and the bottom through a quartz window and are absorbed by the organic TMAE molecules and knock out an electron, called a *photoelectron*. The electron drifts to the sense wires in the uniform drift field of 400 V/cm established by a set of equally spaced wires around the box. The sense wires and readout electronics are located at the endcap side of the TPC. Negative high voltage is applied on the midplane side of the TPC. Over a maximum drift distance of 126 cm this amounts to a potential difference of 60 kV between the HV side and the readout side. The electrons drift parallel to the magnetic field produced by the magnetic coil in the detector. The anode of each drift box is made of 93 carbon fiber wires of $7\mu m$ diameter, strung in the radial direction with a spacing of 3.2 mm. Each wire has identical readout electronics on both ends for charge division. The z-coordinate of the electron conversion, along the beam axis, is obtained from the measurements of the drift time and the azimuthal coordinate is determined by the anode wire address. The depth of the conversion in the drift box is measured by charge division on the sense wires. The detector is optimized for single electron detection, typically a dozen electrons from each circle make it all the way to the anode. However, it will also detect the large dE/dx signal of ionization loss from the charged particle passing through the drift box.

The barrel CRID consists of 40 TPCs, 40 liquid radiator trays and 400 spherical mirrors. Each endcap portion of the CRID has 5 TPCs, 1 liquid radiator and 60 mirrors.

3.2.3   The Calorimeter System

The task of the calorimetry is to measure accurately the fraction of electromagnetic and hadronic energies from the decay of the Z^0, covering as much of the solid angle around the IP as possible. This large solid angle is very important because of

cleanly separating events with missing energy. The SLD calorimeter consists of three parts:

- a lead-liquid argon calorimeter (LAC), which absorbs most of the electromagnetic and hadronic energy in order to measure them,

- a warm iron calorimeter (WIC) which contains the tails of hadron showers and tracks penetrating particles through the LAC, such as muons and

- a Luminosity Monitor (LUM) which measures the energy deposit of the Bhabha events at very small angles to the beam and determines the luminosity of the SLC.

The electromagnetic part of the LAC has 22 radiation lengths X_0, and the LAC and the WIC together have 8 interaction lengths[6] to absorb most hadrons completely. Electrons and gammas form electromagnetic showers which can be distinguished from hadronic showers by the profile of the energy deposit. Electromagnetic showers deposit most of their energy within the first section of the LAC while hadronic showers extend much further into the detector since the hadronic interaction length is greater than the electromagnetic radiation length. The form of the showers can thus be used to separate electrons from pions and/or protons. An EM shower matched to a track in the CDC will be identified as an electron and can thus be separated from a shower induced by a gamma.

The Liquid Argon Calorimeter

The LAC is placed inside the magnet coil, to avoid degrading the performance of the calorimeter due to energy absorption in the material of the coil. The LAC works as an ionization chamber and consists of stacks of lead tiles interspaced by gaps filled with purified liquid argon as a sensitive material. The tiles at ground and negative high potential are mutually placed. Tiles at the same potential are connected together like a daisy chain to form projective towers pointing to the IP. The signals are induced on the anode when the electrons from primary ionization drift to the electrode. Since no secondary ionization occurs in argon, the signal must be amplified by charge amplifiers.

The towers have lateral dimensions between 6 and 12 cm, somewhat larger than the average lateral size of an electromagnetic shower. The towers are further split into four parts in the radial direction, making up two electromagnetic parts of the

---

[6]$1 - e^{-1}$ of all charged particles interact electromagnetically in one radiation length and $1 - e^{-1}$ of all hadrons interact strongly with matter of one interaction length they are passing through.
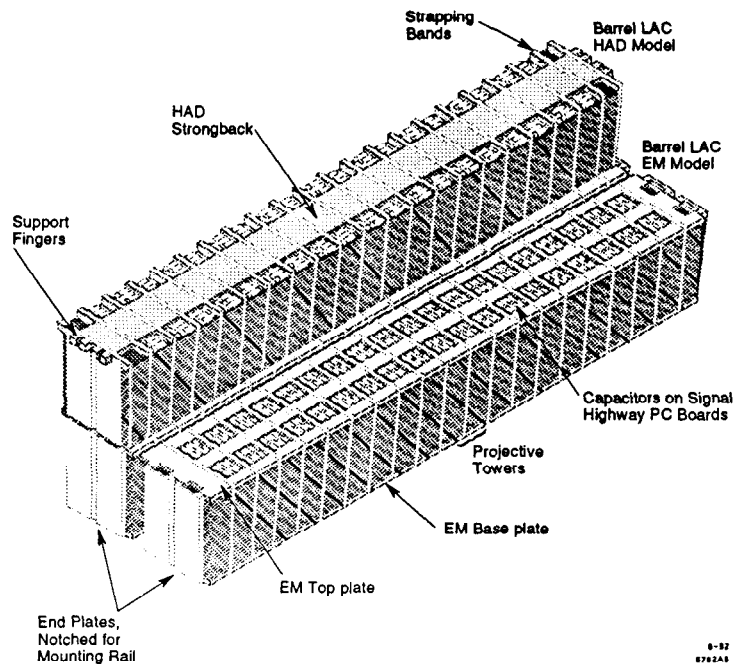
Figure 3.13: The barrel liquid argon calorimeter (LAC). Shown are three of the 288 modules that make up the barrel LAC.

calorimeter, E1 and E2, and two hadronic parts, H1 and H2 as shown in Figure 3.13. The geometry of the electromagnetic section was chosen to provide the best possible efficiency for isolating electrons from semileptonic decays within jets, lowest possible π/γ overlap background, and good position resolution. The LAC is placed inside a vacuum vessel and surrounded by a cryostat which is cooled by liquid Nitrogen. The LAC's endcap is a continuation of the barrel in the forward and backward direction with a similar internal tower geometry. The endcaps fit like plugs inside the barrel. Together they cover about 98% of the solid angle for electromagnetic showers.

Since a liquid argon calorimeter has no gain in the sensitive medium and therefore produces very small signals, low noise amplifiers must be provided. The approximately 44,000 electronics channels require a fast pre-processing of the event to form reliable trigger information and to reduce the data volume passed to the computer.

The Warm Iron Calorimeter

The hadronic energy which escapes the LAC is measured by the Warm Iron Calorimeter (WIC) which also serves as a muon tracking device and as a flux return

Detail of Single Layer

Double Layer for Muon Tracking

Fe

Pads
Wire
Plastic 8-tube Container
Graphite Coated Comb Structure
Longitudinal Strips

Fe

Fe

Pads
Transverse Strips
Ground Plane
Transverse Strips
Longitudinal Strips

Fe

100 cm

Fe Single Layer Typical

Single Layer Typical

Detail of Double Layer

4-94
7628A86

100 cm
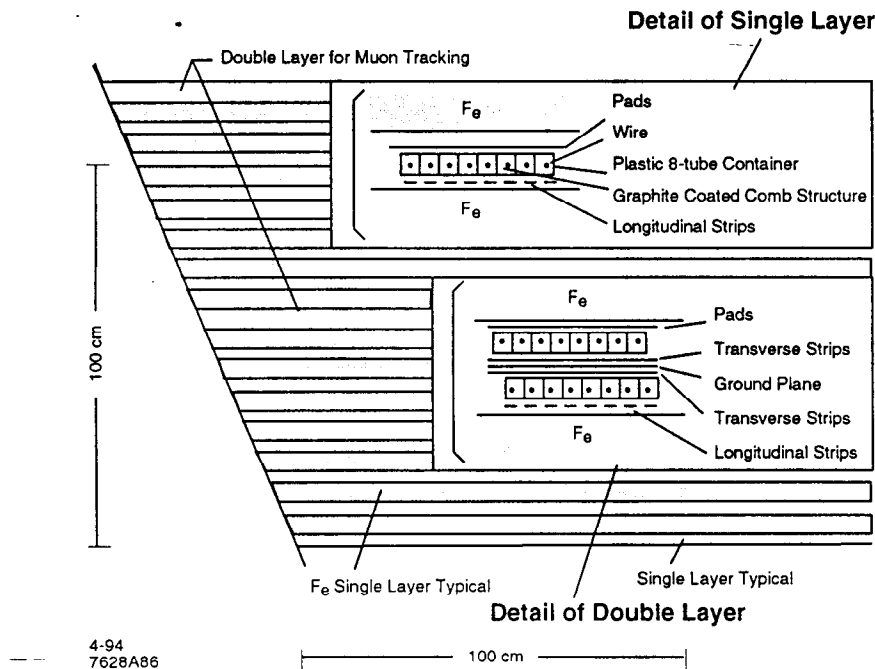
Figure 3.14: The worm iron calorimeter(WIC).

yoke for the magnetic field. The iron structure is segmented into 18 layers, 50 mm thick with 32 mm gaps instrumented with streamer tubes(Iarocci gas tubes) shown in Figure 3.14. At 90° the iron makes up 4 interaction lengths; together with the LAC and the coil, the SLD has at least 8 interaction lengths in any direction. The WIC consists of eight barrel section surrounding the coil in an octagonal fashion and two endcaps, covering almost the entire solid angle around the IP.

In the center of the slightly conductive graphite coated plastic 9 mm × 9mm streamer tubes, there is a 100μm wire of BeCu held at 4.5 kV in a gas mixture of 25% argon and 75% isobutane. On the top and bottom of the tubes is stripes of G10 material plated with copper patterns in the form of strips and pads. A charged particle passing through the gas mixture forms so-called streamers, small discharges from the high voltage wire to the surface, inducing charge in the copper circuits proportional to the energy of the particle, typically 12 pC per streamer and about 7-8 streamer per GeV of energy.

In the eight coffins of the barrel section there are 17 layers of tubes. The strips run parallel to the tubes, except in layer 8 and 17 where they are perpendicular to them They are read out digitally providing an exact tracking of the particles in r-ϕ

40
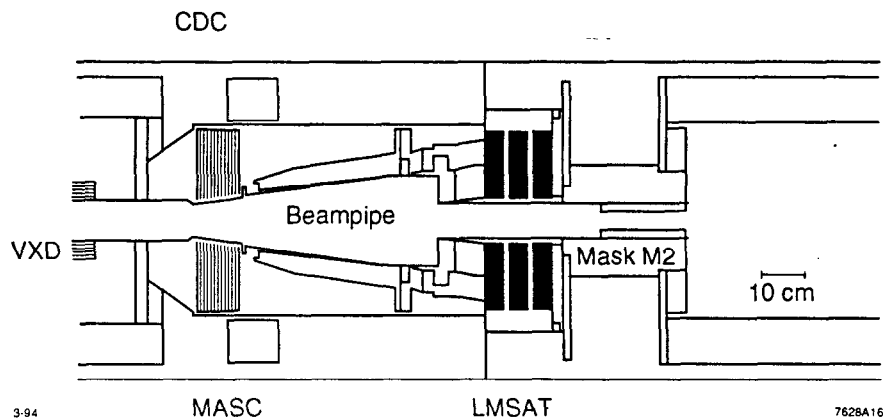
Figure 3.15: The luminosity monitor.

and two points in z determining the angle of the muons to better than 10 mrad.

The geometry of the pads is a continuation of the hadronic tower structure of LAC. The readout is analog, proportional to the energy deposited. They are squares of 265 mm × 216 mm on the inner most layer, increasing in size to 295mm × 316mm in the outer plane. The first eight layers are connected together to measure the energy flux in the "front tower", the remaining 7 layers form the "back tower".

The endcap region consists of eight horizontal and eight vertical layers of tubes read out in a similar fashion as the barrel with strips along each tube and pads in a tower structure. To cover the gaps between the endcaps and the barrel, so called 45 chambers have been installed on the support arches. Along each section of the octagon there are two of these chambers, staggered by half a cell, 120 cm × 375 cm in size, with strips parallel and vertical to the tubes. The WIC contains a total 101,488 strips and 8640 towers covering 97% of the solid angle.

The Luminosity Monitor

The Luminosity Monitor (LUM) [28] in the SLD consists of Small Angle Tagger (LMSAT) and the medium angle silicon calorimeter(MASiC) shown in Figure 3.15. The LUM provides SLD's small angle electromagnetic coverage, measuring photons and electrons in the 23-200 mrad region. The main function is to measure the luminosity by tagging of electrons in Bhabha events. With a total of 23 radiation lengths it simultaneously provides a low angle coverage for the calorimetry.

The LMSAT and MASiC are cones of silicon detector centered around the beam

pipe with a projective tower structure very much like the LAC. The LMSAT covers the angles from 23 to 65 mrad and is about 1 m from the IP, right in front of the final focus magnets. The MASiC covers the angle of 65 to 200 mrad and is right next to the VXD at $z = \pm 200$ mm. On both devices each of the 23 layers of silicon detector is interspaced with tungsten plates of 1 radiation length. Like the electromagnetic part of the LAC the monitor is split up into EM1 and EM2, two sets of towers in front of each other.

Chapter 4

Analysis

4.1 Introduction

The data taken by the SLD in the 1993 run and the events generated by a Monte Carlo simulation are used for this study. The brief summary of the production of Z^0 bosons by the SLC and data taking by the SLD is described, followed by the description of event generation by the Monte Carlo simulation.

Z^0 **Production by the SLC and SLD Data Taking** SLC produced the first Z^0 in April, 1989. Z^0s were measured by the Mark II detector which was located at the IP of the SLC prior to the SLD. The Mark II detector was replaced by the SLD after it collected about 700 Z^0 decays in 1989 and 1990. The SLD was rolled in to the IP in the spring of 1991. The SLD collected about 400 Z^0 decays in the 1991 engineering run without the electron beam polarization. In the 1992 run, electron beam was polarized with magnitude of 23% and the SLD collected about 10000 Z^0 decays. In the 1993 run, the electron beam polarization was increased to 63% due to the replacement of the photocathode by the strained gallium arsenide crystal. The luminosity of the SLC was also improved and at the end of the 1993 run about 50000 Z^0 decays had been accumulated by the SLD.

The SLD Monte Carlo Each events are reconstructed by using the data from individual detector elements. The reconstructed events may get biased due to the detector effects such as the limited coverage and detector resolutions. Those effects give bias to some results. Therefore, we have to estimate the magnitude of the effects and correct such results by using events produced by event generators and the SLD detector simulation. There are several event generators, such as JETSET[29], HERWIG[15]

43

for $e^+e^- \rightarrow q\bar{q}$, KORALZ[30] for $e^+e^- \rightarrow \tau^+\tau^-$, BHLUMI[31] for $e^+e^- \rightarrow e^+e^-$ and MCTWOG[32] for 2γ events. It depends on the aim of the study which generator is used. The generated particles are fed to the program called GEANT[33] which simulates particle decays, nuclear and electromagnetic interactions, multiple scattering, etc. GEANT was tuned to the SLD so as to reproduce well the response of the SLD.

JETSET version 6.3[29] and GEANT version 3.14[33] were used for the hadronic event generation and the SLD detector simulation, respectively. Generated events have the same information, *e.g.* hits in the CDC, output from each of the LAC tower, etc., as that contained in the real data. Those generated events are fed to the SLD reconstruction program which reconstructs charged tracks in the tracking system, determines the energy deposit in the calorimeter system and identifies the charged particles. This procedure is the same as that for the real data.

This study focused on the transport of parton polarization through the hadronization process. As mentioned in Section 2.2, none of the hadronization models implements the spin transport through the hadronization to event generators. Therefore, events generated by the programs are expected to have no signal in terms of the polarization and we can not estimate how large the signal can be. However, these generated events are useful to estimate systematic errors or biases introduced by the analysis methods.

4.2   Event Type and Triggers

Events produced by decays of the Z^0 are divided into the following four categories:

- Hadronic events,

- Electron-positron events,

- $\mu^+\mu^-$ events and

- $\tau^+\tau^-$ events.

Examples of typical events in these categories are shown in Figure 4.1. Hadronic events are characterized by a burst of tracks observed in the drift chamber and they form jet-structure. For e^+e^- and $\mu^+\mu^-$ production, two back-to-back charged tracks are reconstructed in the drift chamber. These two types of events are distinguished either by deposit of electromagnetic energies in the LAC or tracking by the WIC. Both charged tracks in the electron-positron pair production have large amount of energy deposit in the electromagnetic part of the LAC due to the electromagnetic showers.

44
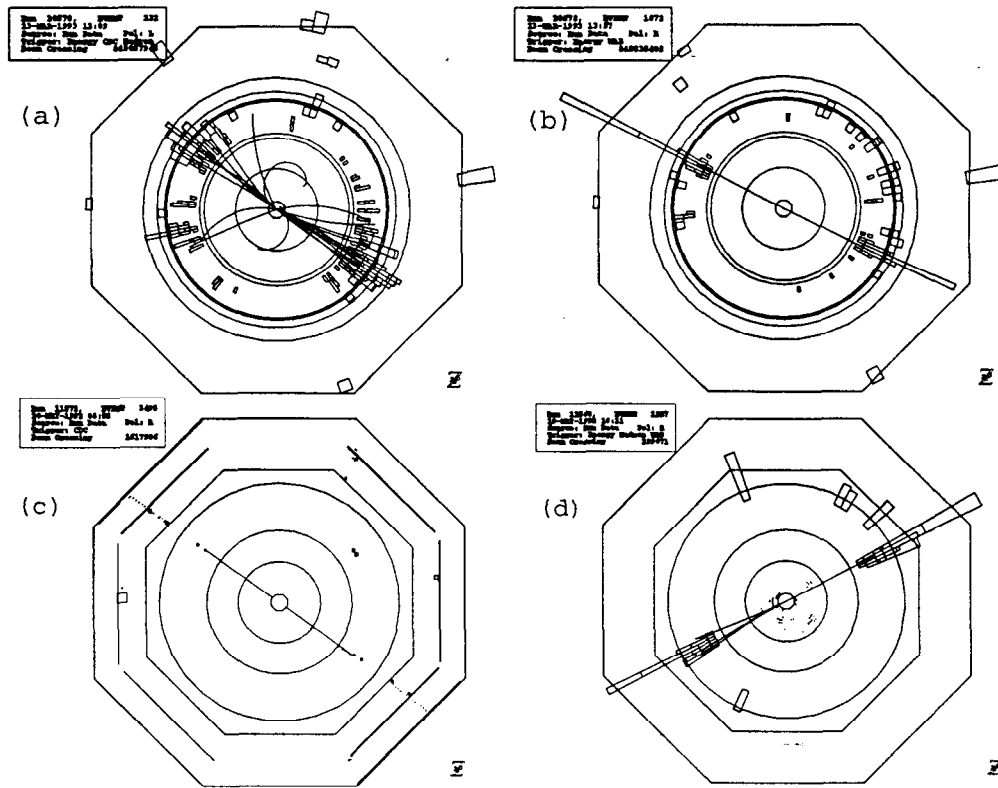
Figure 4.1: Examples of four categories of physical events. Shown are (a) a hadronic event with 2 jets, (b) an e^+e^- pair production, (c) a $\mu^+\mu^-$ pair production and (d) a candidate of a $\tau^+\tau^-$ pair production, where a τ^- and τ^+ decayed into three charged particles(a 3-prong decay) and one charged particle (a 1-prong decay). Each trapezoid indicates an energy deposit in a tower of the LAC and its area is proportional to the amount of the deposit.

On the other hand, charged tracks in the $\mu^+\mu^-$ pair production lose energies only by ionization so that they deposit small fraction of their energies (about a few hundred MeV) in the LAC. In addition, the tracks are observed by the WIC surrounding the LAC. The $\tau^+\tau^-$ pair production events exhibit the characteristics different from hadronic events or other lepton-antilepton pair production events due to the variety of decay modes of τ lepton. The event, in general, has two or more tracks, but does not have so many tracks as a hadronic events. τ decays into e, μ or hadrons so that the energy deposit in the LAC depends on those particles.

Event Triggers   The purpose of the event trigger is to reduce the background events as much as possible without loss of physical events. The following five trigger types were used to select the events:

- The energy trigger, which is the most important trigger described below,

- The luminosity trigger, which requires a minimum deposit energy of 10 GeV in each of two back-to-back towers in the LUM,

- The tracking trigger, which requires two or more tracks detected in the CDC with an opening angle > 20°,

- The hadron trigger, which is a combination of the energy trigger and the tracking trigger with at least one track in the CDC, and

- The random trigger, which records events at the time of a beam crossing at a fixed rate of 1/20 Hz for the purpose of background studies.

The trigger rate depends on the beam conditions. The hadron trigger is often used to reduce the trigger rate when the beam conditions are noisy. Among these triggers, the energy trigger is most important. The energy trigger[34] uses information defined by the following three LAC quantities:

- $\overline{\text{NEMHI}}$, which is the number of LAC EM towers that have signals above 60 ADC counts,

- EHI, a high-threshold energy sum, which is the sum of energy recorded in all EM tower with signals above 60 ADC counts and HAD towers with signals above 120 ADC counts and

- ELO, a low-threshold energy sum, which is the sum of energy recorded in all EM towers above 8 ADC and all HAD towers above 12 ADC.

The LAC energy scale is based on the energy deposit of a minimum ionizing (min-I) particle, such as muon. The ADC counts for the EM towers and HAD towers correspond to the following energies in the towers:

        EM towers :1 ADC count≈2.8 MeV min-I,
        HAD towers:1 ADC count≈7.5 MeV min-I.

These constants were determined by comparison of the ADC counts for muons with their expected energy deposit in each tower. The energy trigger requirements are:

1. NEMHI $\geq$ 10,

2. EHI > 15 GeV min-I,

3. ELO < 140 GeV min-I,

4. EHI > 1.5 × (ELO − 70) and

5. Each north/south side of the detector must have NEMHI > 0.

Requirements 1 and 2 identify large energy deposits in the LAC caused by hadronic events. The backgrounds due to beam-wall and beam-gas interactions are removed by 3 and 5. SLC muon backgrounds[1] are removed by 1, 2 and 4.

4.3 Event Selection

Events satisfying the trigger criteria still contain background events besides the Z^0 events. Since only the hadronic events of Z^0 decays were used in this study, background events[2] and leptonic events must be removed from the event samples. In the study, only charged tracks measured by the central drift chamber and the vertex detector were used. Therefore, the hadronic event selection depends on charged track measurements and no information of the calorimetry was used. It was performed in two steps: good track selection and hadronic event selection using those tracks.

In the first step, the good track selection was performed by requiring the following four criteria for charged tracks:

- the track had transverse momentum of $p_\perp > 0.15$ GeV/c with respect to the beam axis,

- cosine of polar angle θ with respect to the beam axis was in a range of -0.8 to 0.8,

- distance of the track's closest approach to the beam axis was less than 5 cm and

- distance of the track's closest approach to the interaction point along the beam axis was less than 10 cm.

Figures 4.2, 4.3, 4.4 and 4.5 show distributions of transverse momentum with respect to the beam axis, p_t, cosine of polar angle θ, $\cos\theta$, distance of closest approach to the beam axis, r_0 and distance of closest approach to the interaction point along the beam axis, z_0.

---

[1]The SLC produces muons when stray electrons and positrons collide with collimators. Some of these muons are transported to by the accelerator and strike the SLD at a nearly horizontal direction.

[2]Background means events such as interactions of the beam with the beam pipe or gas inside the beam pipe.
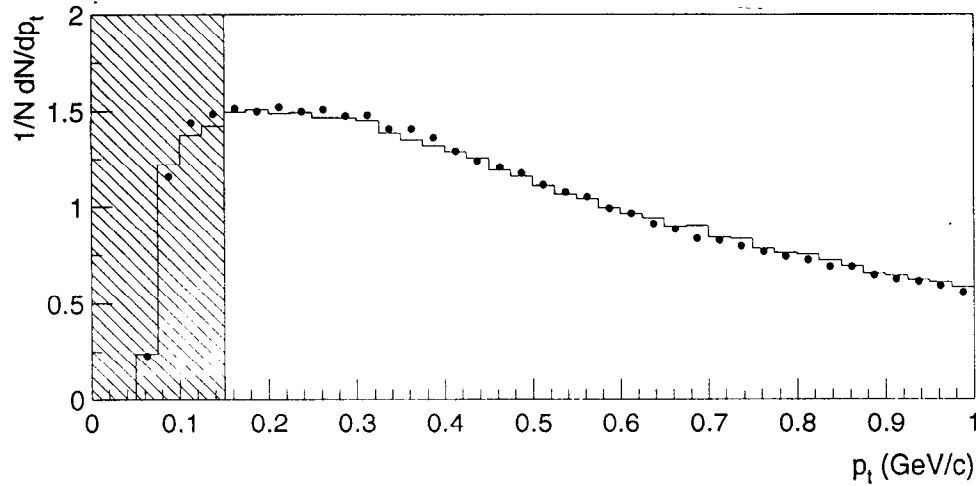
Figure 4.2: Distribution of transverse momentum of charged tracks with respect to the beam axis. Points represent data and histogram shows the Monte Carlo simulation. Charged tracks in the hatched region were not used in this study.
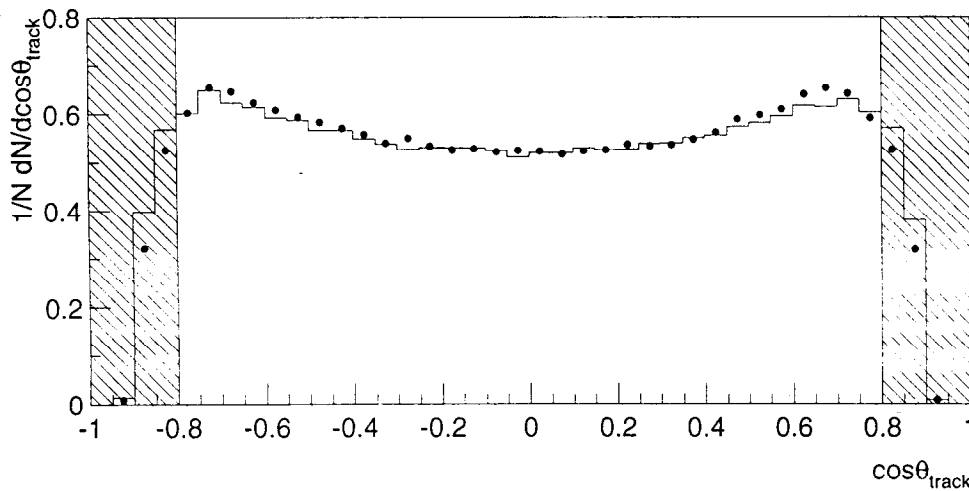
Figure 4.3: Distribution of cosine of polar angle of charged tracks. Shown are data (points) and the Monte Carlo simulation (histogram). Charged tracks in the hatched region were not used in this study.
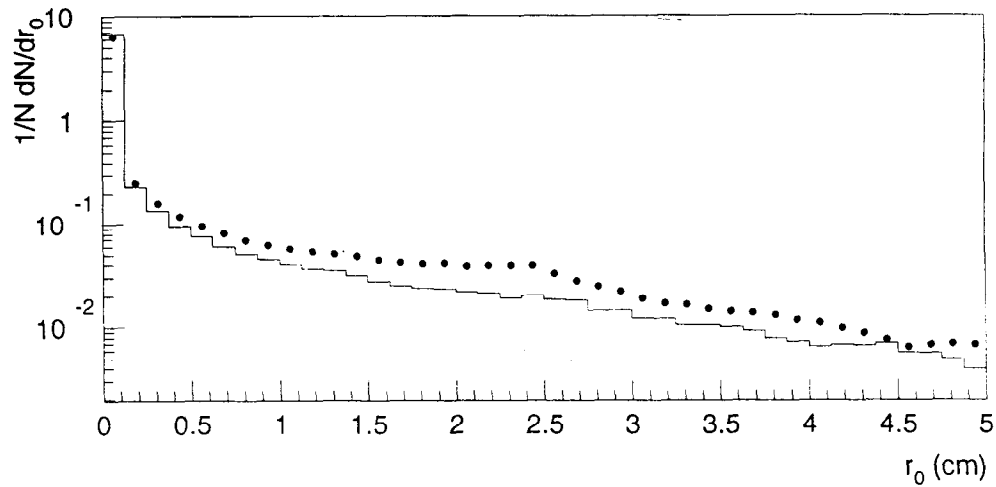
Figure 4.4: Distribution of distance of closest approach of charged tracks to the beam axis. Shown are data (points) and the Monte Carlo simulation (histogram). There is a discrepancy between data and Monte Carlo in the region of large distance. The discrepancy is ascribed to background tracks and tracking failure. The Monte Carlo does not completely simulate the real events in the region.
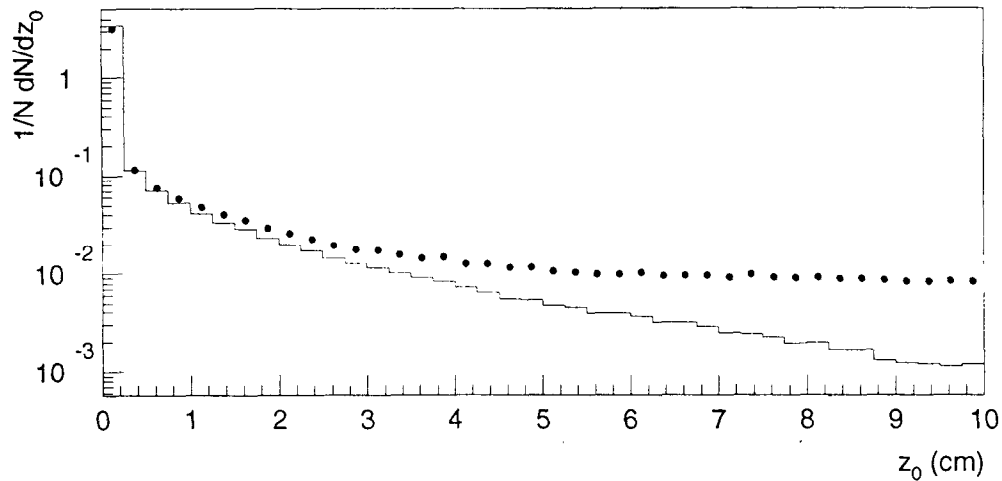
Figure 4.5: Distribution of distance of closest approach of charged tracks to the interaction point along the beam axis. Shown are data (points) and the Monte Carlo simulation (histogram). There is a discrepancy between data and Monte Carlo in the region of large distance.
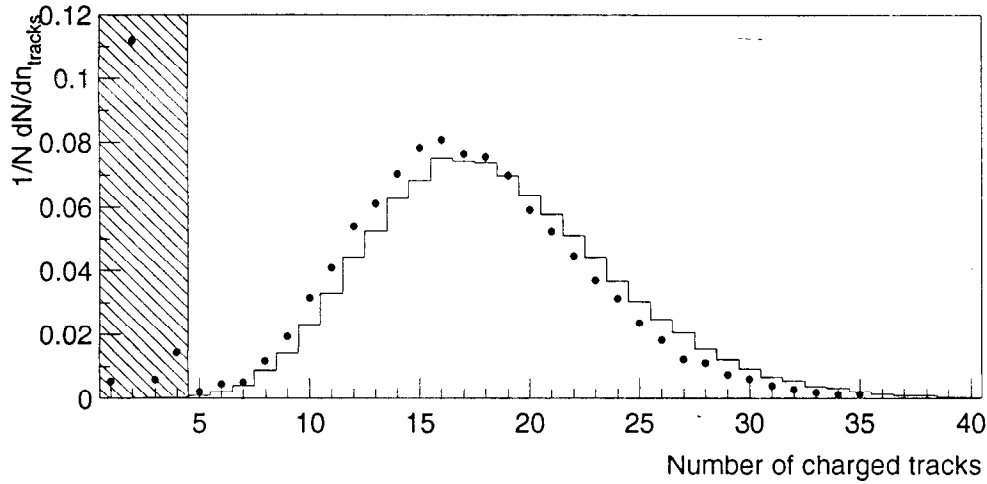
Figure 4.6: Distribution of number of good charged tracks in an events. Shown are data (points) and the Monte Carlo simulation (histogram). Events in the hatched region were not used in the analysis. Large number of entries in data at two tracks is contribution from $e^+e^-, \mu^+\mu^-$ and $\tau^+\tau^-$ pair productions.

After good tracks were selected, hadronic events were selected according to the following three conditions:

- There were at least 5 good charged tracks in an event,

- the cosine of the thrust axis which was calculated using the selected tracks was in the range $|cos\theta_T| < 0.71$ and

- the sum of the energies of charged tracks, *a visible energy* was more than 20 GeV, where all selected tracks were assumed to have the charged pion mass.

Figures 4.6, 4.7 and 4.8 show distributions of number of good charged tracks in an event (*charged-track multiplicity*), cosine of the thrust axis ($|\cos\theta_{thrust}|$) and charged visible energy. Thrust T is defined as[35]

$$T = \max\left(\frac{\sum_i \vec{p_i} \cdot \hat{t}}{\sum_i |\vec{p_i}|}\right) \tag{4.1}$$

where $\vec{p_i}$ is momentum of a final state particle and i runs over all the final state particles and the axis $\hat{t}$ is called the thrust axis. After this hadronic event selection, 30036 events survived.
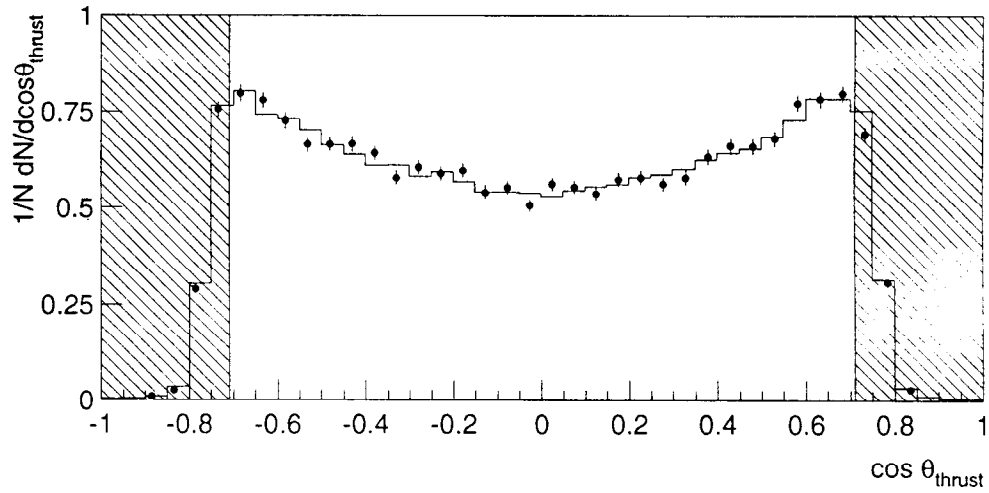
Figure 4.7: Distribution of cosine of the thrust axis. Shown are data (points) and the Monte Carlo simulation (histogram). Events in the hatched region were not used in the analysis.
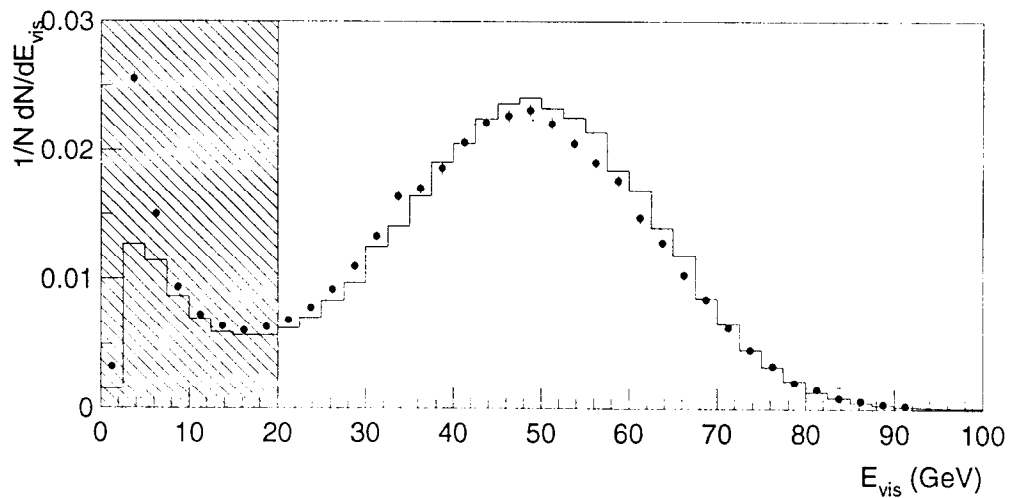
Figure 4.8: Distribution of charged visible energy. Shown are data (points) and the Monte Carlo simulation (histogram). Events in the hatched region were not used in the analysis.
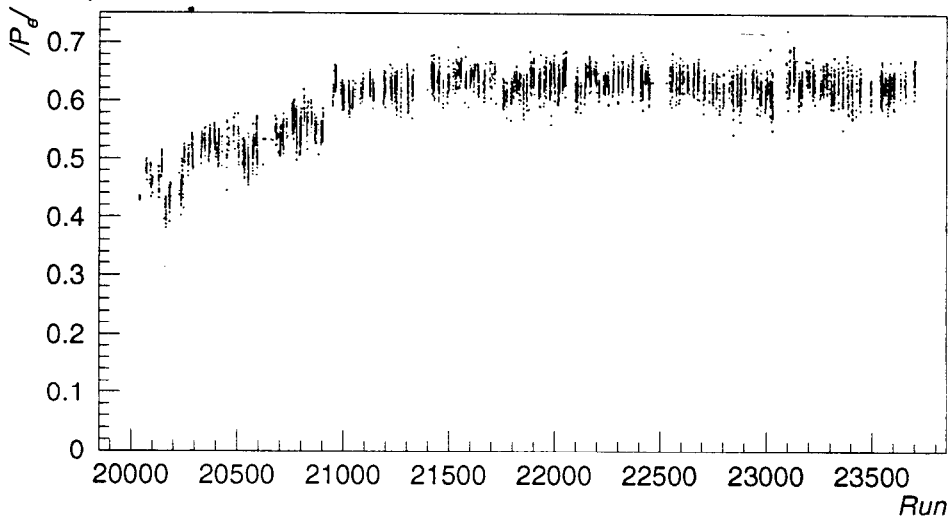
Figure 4.9: Electron beam polarization shown as a function of run number. Each point represents the beam polarization measured by the Compton polarimeter near an event.

The SLC provides the longitudinally polarized electron beam and the Compton polarimeter measures the polarization of the beam downstream of the SLD as described in Section 3.1.3. This study took advantages of the longitudinal electron beam polarization, so that the analyzing power for jet handedness is determined at high accuracy in the helicity-based analysis. The beam polarization is measured every 3 minutes by the Compton polarimeter. The polarization for each event is the polarization measurement closest in time to the event. Figure 4.9 shows the beam polarization of each event which satisfied the above hadronic event selection criteria. The average electron beam polarization $\langle \mathcal{P} \rangle$ for the 1993 run was estimated by using the luminosity weighted average:

$$\langle \mathcal{P} \rangle = (1 + \xi) \frac{1}{N} \sum_{events} \mathcal{P}_i, \tag{4.2}$$

where N is the total number of events, $\mathcal{P}_i$ is polarization measured by the Compton polarimeter near the ith event, and $\xi = 0.017$ is the chromaticity correction for polarization biases due to tails in the beam energy distribution. The average value was[20]:

$$\langle \mathcal{P} \rangle = 0.630 \pm 0.011. \tag{4.3}$$

Selected events had the magnitude of electron beam polarization in a range between 0.2 and 0.8. If the polarization was negative, -0.63 was used for the helicity-based

analysis as nominal polarization. In the case for the positive polarization, +0.63 was used.

The numbers of events with right- and left-handed beam polarization were 13515 and 16519, respectively[3].

2-jet events were selected in order to avoid contamination from hard gluon emission, since we can not predict the polarization of such gluons. There are several algorithms to find jets[36]–[38]. All algorithms basically consist of two processes: calculating invariant the mass or a similar quantity for each pair of tracks in an event, and combining the tracks. The JADE algorithm[36] was used in this study. In the following, the procedure in the JADE algorithm is explained as an example:

1. The scaled "invariant mass" y_{ij} of every pair of particles is calculated, assuming all hadrons to be massless:

$$y_{ij} = \frac{2E_i E_j (1 - \cos\theta_{ij})}{E_{vis}^2} \qquad (4.4)$$

where E_i, E_j and $\cos\theta_{ij}$ are the particle energies and the angle between them. E_{vis} is the total energy in the event.

2. The pair with the smallest invariant mass y_{ij} is combined into a pseudo-particle or cluster k by adding their 4-momenta:

$$p_k = p_i + p_j \qquad (4.5)$$

As a result of this procedure, the number of tracks in the event decreases by one.

3. The above procedure is repeated until the smallest invariant mass y_{ij} becomes larger than a cutoff value y_{cut}. y_{cut} defines the resolution of two jets. Selection of the y_{cut} value depends on the purpose of studies. The remaining pseudo-particles are defined as jets.

The definition of the scaled invariant mass and the combination criteria depend on the algorithm used for jet-finding.

Figure 4.10 shows the fractions of 2-jet events and events containing 3 or more jets as a function of y_{cut} value for the hadronic events in the case of the JADE algorithm. As y_{cut} value increases, 2-jet events increase and multi-jet(3 or more) events decrease. The y_{cut} value has to be small enough to avoid the contamination of 3-jet events, *i.e.* $e^+e^- \to q\bar{q}g$. If a 3-jet event is categorized as a 2-jet event by

---

[3]There were only 2 events with no polarization measurement. They were discarded.
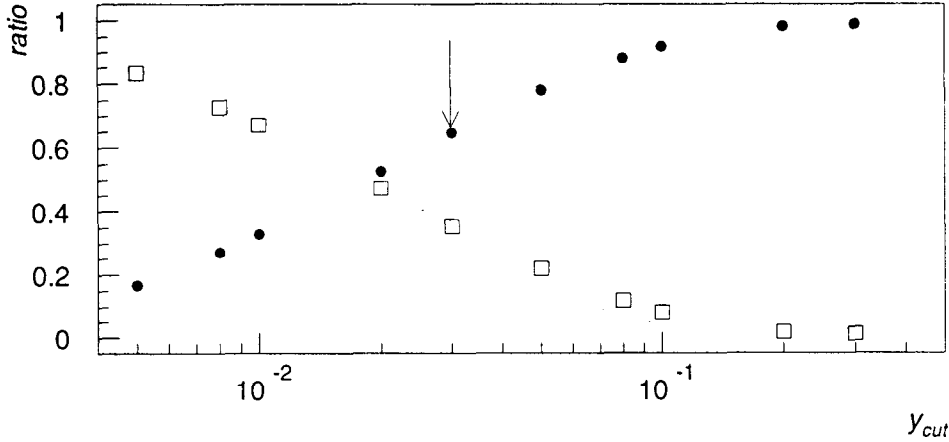
Figure 4.10: Jet rate as a function of y_{cut} value for the hadronic events. Shown are fractions of 2-jet events (points) and events with 3 jets or more (squares). $y_{cut} = 0.03$ was used in this analysis (shown by arrow).

some y_{cut} value, its thrust axis does not represent quark and antiquark momentum vectors correctly. The contamination may dilute a signal measured in this study. However, a small value of y_{cut} results in decrease of 2-jet events and makes the statistical fluctuation in results increase. The y_{cut} value used throughout this study was 0.03 (Figure 4.10). At $y_{cut} = 0.03$, 2-jet event rate was found to be about 65% of hadronic events. In order to get correct parton direction, the additional requirement of the acollinearity angle[4] to be less than 20° left about 90% of the 2-jet events. There remained 9942, 8196 2-jet events with left-, right-handed electron polarization, respectively.

4.4 Flavor Tagging by Normalized Impact Parameter

A handedness signal may be diluted in heavy quark events ($Z^0 \rightarrow c\bar{c}, b\bar{b}$), since many tracks come out from decays of spinless heavy mesons. Dalitz *et. al* have reported a study of the expected handedness signal for charm quarks and concluded that any spin effect resulting from D^* or B^* decays was very small[2]. Therefore,

---

[4]The acollinearity angle is defined as difference between π and an angle between two jets.
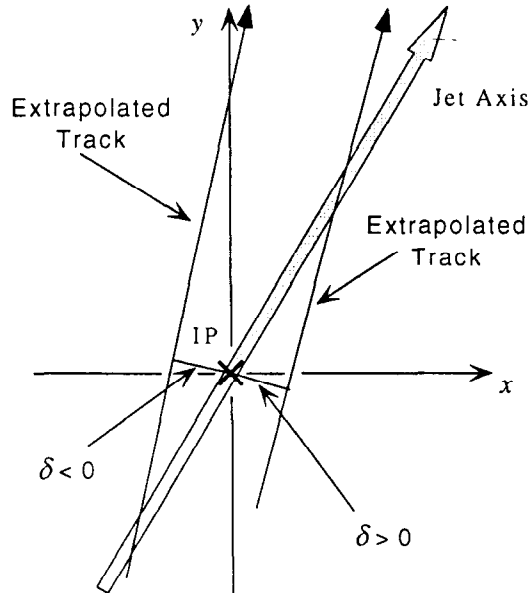
Figure 4.11: Definition of the signed impact parameter, δ. The sign of the impact parameter depends on the location of an intersection between a extrapolated track and the jet axis in which the track are contained.

we should use only light flavor $(u\bar{u}, d\bar{d}, s\bar{s})$ events in order to observe the possible handedness signal. In this study, the data is divided into two samples which originated from a light or heavy flavor $q\bar{q}$.

The separation of light flavor events from heavy flavor events uses a flavor tagging technique[5]. Heavy flavor tagging often makes use of the information on the decay length of heavy flavor mesons, *e.g.* D, B, etc. As the decay length is short (typically a few hundred μm), they are detectable only by placing a very precise position detector near the IP. This means that the efficient flavor tagging strongly depends on the performance of the detector and its location. The VXD in the SLD satisfies the requirements and, in practice, achieves high efficiency for heavy flavor tagging. Light flavor events are anti-tagged against the heavy flavor tagging.

Event flavor tagging used the signed x-y impact parameter, δ. The parameter is defined as the distance of closest approach of a charged track to the IP in x-y plane[6]. Figure 4.11 shows the definition of the signed impact parameter, δ. If an extrapolated track crosses the jet axis before its closest approach to the IP, its δ is set to be positive. On the other hand, if there is an intersection between a track and

---

[5]The flavor tagging method was often used to measure lifetime of B hadrons[39]

[6]The x-y plane is defined as a plane perpendicular to the beam axis.
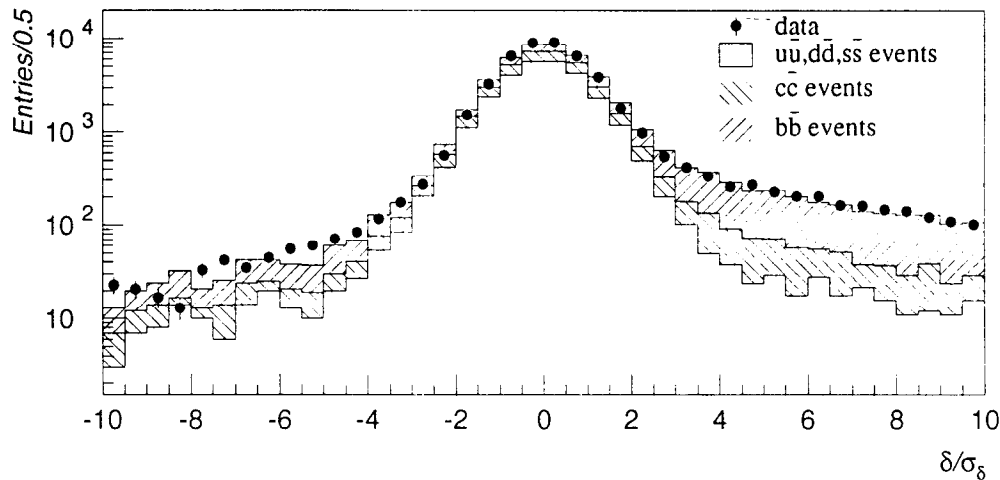
Figure 4.12: Distribution of the normalized impact parameter. Shown are data(points) and the Monte Carlo simulation (histograms). Each of two kinds of hatched areas shows the contribution from $c\bar{c}$ and $b\bar{b}$ events to entries in the Monte Carlo simulation.

the jet axis after the track passes its closest approach, its δ is negative.

In addition to the standard good track selection criteria, the following restrictions are imposed in order to ensure good measurements of the impact parameter:

- tracks must have at least 2 clusters of hits in different CCD layers of the VXD,

- tracks must have $\chi^2/NDF^7 < 5.0$ in a track fit to the CDC hits and

- tracks must not come from V^0 particles (if an invariant mass of two tracks falls into in a range of K^0 or Λ^0 mass, those tracks are removed).

The signed normalized impact parameter, δ/σ_δ, was defined as signed impact parameter divided by its measuring error. Figure 4.12 shows the signed normalized impact parameter distribution for data and the Monte Carlo simulation. The simulation well reproduces the data. The excess of positive impact parameters seen in Figure 4.12 is ascribed to the secondary vertices produced by decays in flight of heavy flavor mesons. The heavy flavor mesons are only produced in $c\bar{c}$ or $b\bar{b}$ events. This quantity was used for flavor tagging. The flavor tagging purity and efficiency depend on the cut value of the normalized impact parameter(*the normalized impact parameter significance*). This value must be optimized in terms of the purity and efficiency.

---

[7]Number of degrees of freedom.
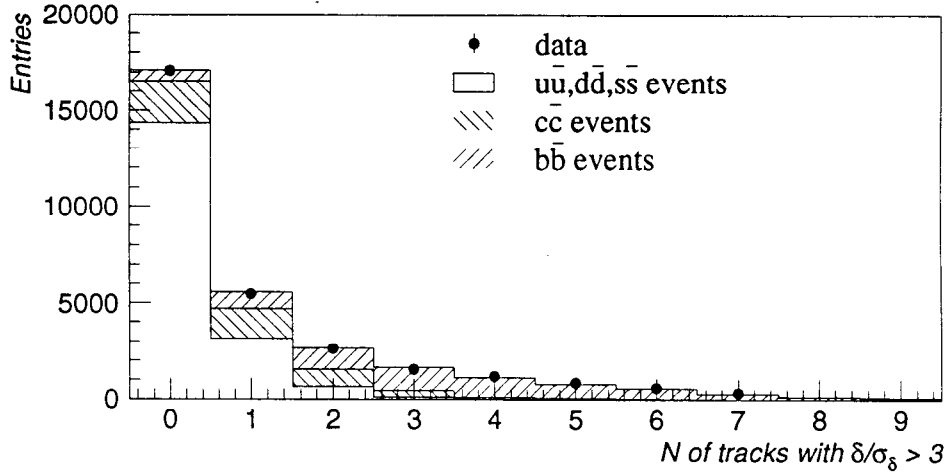
Figure 4.13: Distribution of the number of the significant tracks in an event. Shown are data(points) and the Monte Carlo simulation (histogram). Two different hatched areas show the contributions from $c\bar{c}$ and $b\bar{b}$ events to entries in the Monte Carlo simulation.

In this study, if δ/σ_δ of a track is more than three, that track is called a 'significant track'. The number of significant tracks in a heavy flavor event is expected to be more than that in light flavor events. Figure 4.13 shows the distribution of the number of significant tracks in an event. Each event was classified as being of light (u, d or s) or heavy (c or b) quark origin according to the number of significant tracks in the event. Events containing no significant track were assigned to the light flavor sample and all other events were assigned to the heavy flavor sample. The numbers of events in the light and heavy favor samples are given in Table 4.1. The global sample is defined as the sum of the light and heavy flavor samples. The purities and components of

Sample		Right-handed $\mathcal{P}$	Left-handed $\mathcal{P}$
Hadronic events		13515	16519
2-jet events	Light flavor	4608	5547
	Heavy flavor	3588	4395
	Global	8196	9942

Table 4.1: Summary of statistics. 2-jet events are a subset of hadronic events, and are classified into the light and heavy flavor samples according to the number of significant tracks in a event. The global sample is the sum of the light and heavy flavor samples.

Sample	Purity(Π)	Fraction of events from flavor: (%)				
		$u\bar{u}$	$d\bar{d}$	$s\bar{s}$	$c\bar{c}$	$b\bar{b}$
Light Flavor	84.0±0.2	23.6±0.2	30.6±0.2	29.9±0.2	12.8±0.2	3.1±0.1
Heavy Flavor	70.3±0.2	8.3±0.2	10.3±0.2	11.1±0.2	22.6±0.2	47.7±0.3

Table 4.2: Purities of the light and heavy flavor samples and constituent flavor of these samples, estimated by the Monte Carlo simulation.

flavors in the samples estimated from the simulation are given in Table 4.2. The light flavor sample contained about 56% of all events and its purity was about 84%.

4.5   Three Leading Particle Selection Method

This method was based on the analogy to the measurement of the τ polarization for 3-prong decays of τ leptons[3]. In particular, since all charged tracks were assumed to be pions, this method was focused on the decay of the a_1 meson into 3 charged πs via ρ meson and π. The initial parton in $Z^0 \to q\bar{q}$ may be contained in such an a_1. The method measures the polarization of the a_1 similar to the τ polarization on the assumption that the parton polarization is transported to the a_1. As shown in Section 2.3.1, the measurement of the polarization is based on the theoretical model of the 3-prong decay of the τ via the a_1. Therefore, it is essential to select pairs or triplets of particles which produce an invariant mass in the region of the ρ or a_1 mass, respectively.

In order to fulfill this requirement, the analysis was performed in line with the following procedures:

1. The three highest momentum particles in each jet are selected if they had a total charge of ±1.

2. One of the invariant masses for the two oppositely charged pion pairs is required to be in the range $0.62 < m_{\pi\pi} < 0.92$ GeV/c² (ρ-mass region), and the invariant mass of the 3-π system is in the range $0.86 < m_{\pi\pi\pi} < 1.66$ GeV/c² (a_1-mass region).

3. The particles forming the higher mass pair are used to calculate

$$\Omega_{hel} = \hat{t} \cdot (\vec{k}_1 \times \vec{k}_2) \quad \text{and}$$
$$\Omega_{chi} = \hat{t} \cdot (\vec{k}_+ \times \vec{k}_-), \tag{4.6}$$

where the momenta of the particles are defined in the 3-particle rest frame and $|\vec{k}_1| > |\vec{k}_2|$. $\hat{t}$ is the thrust axis signed so as to point along the jet direction. $\vec{k}_+$ and $\vec{k}_-$ are momenta of particles with positive and negative charge, respectively. For the modified helicity-based analysis, $\Omega_{mod.hel}$ is calculated by:

$$\Omega_{mod.hel} = \hat{t} \cdot (\vec{k}_a \times \vec{k}_b)(s_a - s_b) \tag{4.7}$$

where $\vec{k}_a, \vec{k}_b$ are momenta of the tracks with the same charge in the 3-particle rest frame, and $s_a = (k_a + k_c)^2$, $s_b = (k_b + k_c)^2$ are the squared invariant masses of the two pairs of positive and negative particles.

4. For all cases, the jet handedness H is defined as the asymmetry in the number of jets with positive and negative Ω. The helicity-based and modified helicity-based Hs depend on the angle defining the jet direction $\cos\theta$ and the electron beam polarization $\mathcal{P}$. Therefore, jets are divided into several subsets according to $\cos\theta$ and $\mathcal{P}$, and jet handedness $H(\mathcal{P}, \cos\theta)$ is calculated for each subset. The chirality-based H does not depend on $cos\theta$ and $\mathcal{P}$, but the handedness is also calculated for the subsets.

5. The analyzing powers for the helicity-, modified helicity- and chirality-based analyses are determined in the following ways. The helicity- and modified helicity-based analysis fits the following $H_{hel}(\mathcal{P}, \cos\theta)$ and $H_{mod.hel}(\mathcal{P}, \cos\theta)$ to the measured handedness:

$$H_{hel}(\mathcal{P}, \cos\theta) = \alpha_{hel}\mathcal{P}_{hel}(\mathcal{P}, \cos\theta) \tag{4.8}$$

$$H_{mod.hel}(\mathcal{P}, \cos\theta) = \alpha_{mod.hel}\mathcal{P}_{mod.hel}(\mathcal{P}, \cos\theta) \tag{4.9}$$

with

$$\mathcal{P}_{hel}(\mathcal{P}, \cos\theta) \quad = \quad \mathcal{P}_{mod.hel}(\mathcal{P}, \cos\theta) = -2\frac{A_Z(\mathcal{P})\cos\theta}{1 + \cos^2\theta}$$

$$\tag{4.10}$$

where α is the analyzing power to vary and $A_Z(\mathcal{P}) = \frac{A_e - \mathcal{P}}{1 - A_e\mathcal{P}}$. The analyzing power takes a different value for each analysis. The analyzing power for the chirality-based analysis is determined by fitting the measured handedness to the following $H(\mathcal{P}, \cos\theta)$ for each sample:

$$H(\mathcal{P}, \cos\theta) = \alpha\mathcal{P}_{chi}. \tag{4.11}$$

$\mathcal{P}_{chi}$ does not depend on $\mathcal{P}$ and $\cos\theta$. Therefore, the handedness is fitted to a constant value. According to the fractions given in Table 4.2, $\mathcal{P}_{chi}$ for each sample is calculated and given in Table 4.3.

	Global	Light	Heavy
$\mathcal{P}_{chi}$	0.391±0.003	0.354±0.003	0.442±0.004

Table 4.3: The polarization for the chirality-based analysis, $\mathcal{P}_{chi}$, for the global, light and heavy flavor samples.

4.5.1 Application to $\tau \to \pi\pi\pi\nu_\tau$

Before this method was applied to the real data, we tried to study events of $\tau \to \pi\pi\pi\nu_\tau$ by the method. The events were generated by the Monte Carlo program KORALZ[30] which simulates $e^+e^- \to \tau^+\tau^-$. Decays of τ leptons into, for example, $\rho\nu_\tau$, $a_1\nu_\tau$, followed by decays of ρ or a_1 generated by the Monte Carlo program TAUOLA[40]. The Monte Carlo programs take into account the τ polarization and give good agreement with the predictions made by the electroweak theory[18],[19].

About 124k $e^+e^- \to \tau^+\tau^-$ events were generated using the programs. Each τ^- and τ^+ in the events was selectively forced to decay into $a_1^-\nu_\tau$ and $a_1^+\bar{\nu}_\tau$, respectively. The event generation was made without the SLD detector simulation.

Figure 4.14 shows distributions of the invariant masses of two $\pi^+\pi^-$ pairs which give the Dalitz plot for the 3-π system ($\pi^+\pi^+\pi^-$ or $\pi^-\pi^-\pi^+$). The invariant mass of the 3-π system is also shown in the figure. ρ-mass peaks in the two distributions of $m_{\pi\pi}$ are clearly seen due to a_1 decaying into 3-πs via $\rho\pi$. Ω_{hel}, $\Omega_{mod.hel}$ and Ω_{chi} were defined for each triplet satisfying the conditions for invariant masses of 2 πs and 3 πs given in the previous section. These triplets entered the hatched histogram shown in the bottom-left of Figure 4.14.

Jet handedness would be visible as a nonzero mean Ω. In particular, jet handedness for the helicity- and modified helicity-based analyses is of opposite sign for events produced with left- and right-handed beam polarization. It also has opposite sign for jets with positive and negative $\cos\theta = \hat{t}_z$, the z-component of $\hat{t}$. For the chirality-based analysis, jet handedness does not depend on the beam polarization and the jet direction. Figure 4.15 shows the distributions of Ω_{hel}, $\Omega_{mod.hel}$ and Ω_{chi}. For the helicity-based analysis, each Ω distribution looks symmetric about zero, implying that any jet handedness is small. There is a difference between the Ω distributions for forward jets and backward jets for the modified helicity-method. For the chirality-based analysis, it seems that there is an excess in the positive Ω_{chi} region.

The jet handedness for all three analyses was calculated for each bin of jet direction $\cos\theta$ according to Equation (2.21) separately for events produced with positive or negative electron beam polarization. Results are shown in Figure 4.16.
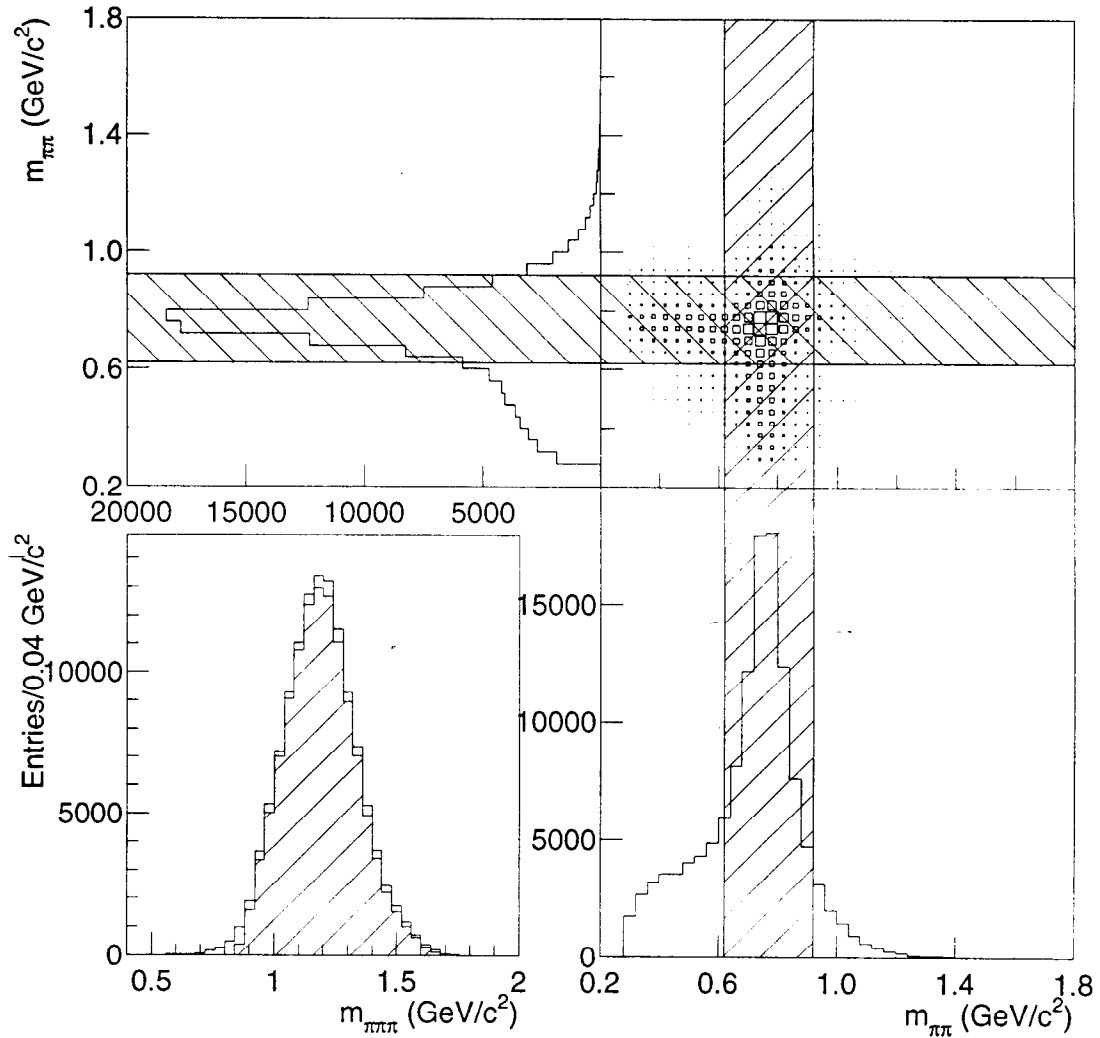
Figure 4.14: Distributions of invariant masses and the Dalitz plot of the 3-π system. The top-left and bottom-right figures show two invariant masses of $\pi^+\pi^-$ pairs, $m_{\pi\pi}$. ρ-mass peaks in both the top-left and bottom-right figures are seen at ~ 0.77 GeV/c^2. Hatched regions in these two figures represent criteria (in text) for the invariant masses of $\pi^+\pi^-$. The bottom-left figure shows the distribution of the invariant mass for the 3-π system, $m_{\pi\pi\pi}$. The hatched histogram in the bottom-left figure represent the triplets lying in the overlap region in the Dalitz plot (top right) and satisfying the conditions (in text) for the invariant mass of the 3-π system.
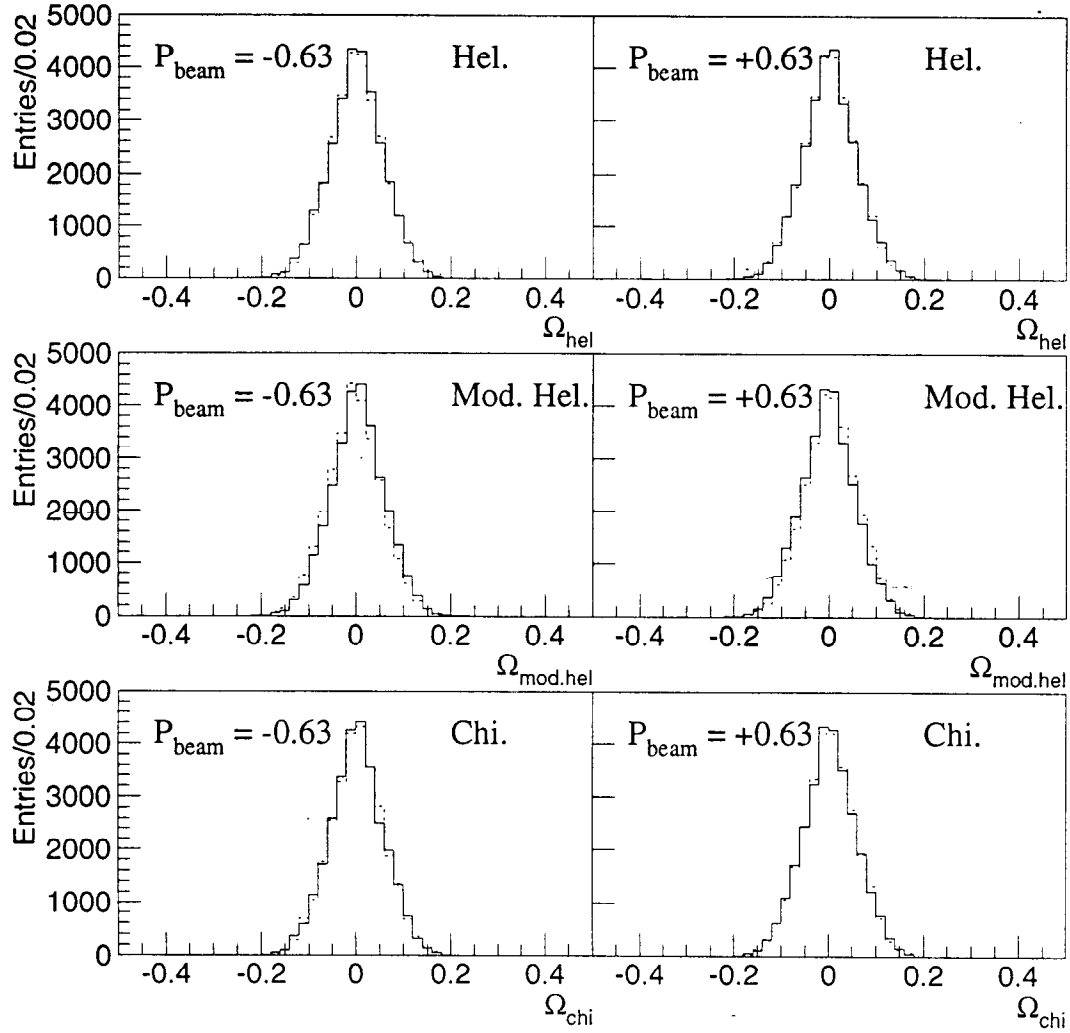
Figure 4.15: Ω distributions for the helicity- (top), modified helicity- (middle) and chirality-based (bottom) analyses. The left and right figures show the distributions for jet in left- and right-handed electron beam events. Solid and dashed histograms show the distributions of Ω_{hel} for jets pointing forward ($\cos\theta > 0.$) and backward ($\cos\theta < 0.$), respectively.
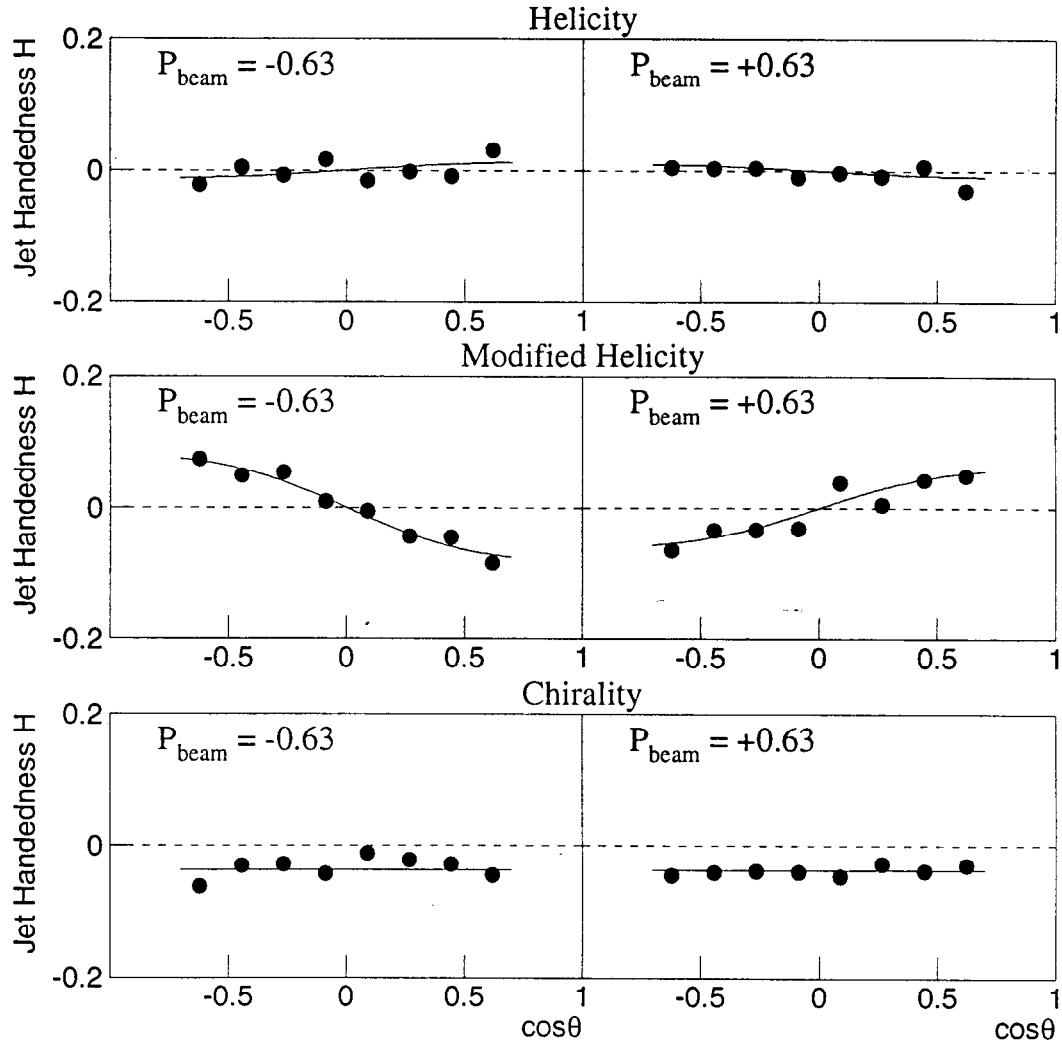
Figure 4.16: Jet handedness as a function of jet direction $\cos\theta$ and the beam polarization $\mathcal{P}$ for the helicity- (top), modified helicity- (middle) and chirality-based (bottom) analyses for the events generated by KORALZ. Events were divided into left- (left) and right-handed (right) events. Solid curves are the result of the best fit of Equations (4.8), (4.9) and (4.10) to data and the reduced χ^2s of the fits are 1.25, 1.30 and 1.02 for the helicity- and modified helicity- and chirality-based analyses, respectively. Data were limited to the region of $-0.71 < \cos\theta < 0.71$ by the detector acceptance.

Analysis	Analyzing Power KORALZ Events
Helicity	-0.018 ± 0.007
Modified Helicity	0.113 ± 0.007
Chirality	-0.256 ± 0.020

Table 4.4: Analyzing powers of the helicity-, modified helicity- and chirality-based analyses for the events generated by KORALZ.

The handedness in each bin for the helicity-based analysis in Figure 4.16 is small and small angular and $\mathcal{P}$ dependence can be seen. This fact means that the corresponding analyzing power is small. For the modified helicity-based analysis, one can clearly see the angular and $\mathcal{P}$ dependences of the handedness. The chirality-based handedness in each bin is negative and all the values are almost equally away from zero.

The obtained handedness was fitted to $H(\mathcal{P}, \cos\theta)$ in Equation (4.8), (4.9) or (4.11) for the helicity-, modified helicity- or chirality-based analysis, respectively, allowing the analyzing power α to vary. In the fitting procedure, $\mathcal{P}_{hel}$ and $\mathcal{P}_{mod.hel}$ were averaged over each $\cos\theta$ bin of 0.1775 and $\mathcal{P}_{chi} = A_\tau$ (Equation 2.29) was 0.1448 as given in Table 2.1. The fitting was performed for events produced with positive or negative beam polarization simultaneously. The results of the fitting are shown as the solid curves in Figure 4.16 for all analyses, and the fitted analyzing power is listed in Table 4.4. Significant nonzero signals were found for the modified helicity- and chirality-based analysis. A small nonzero signal was also found for the helicity-based analysis. The chirality-based analysis gives the largest magnitude of the analyzing power. However, the maximum significance $\alpha/\Delta\alpha$ is given by the modified helicity-based analysis. The results suggest that $\Omega_{mod.hel}$ and Ω_{chi} reflect the helicity of the τ lepton.

4.5.2 Application to Hadronic Jets

In the preceding section, significant signals of the polarization of τ leptons were observed in events generated by KORALZ using the modified helicity- and chirality-based analyses. However, the helicity-based analysis did not show a significant signal of jet handedness. Since the mechanism of transport of the parton polarization may not be the same as that for τ leptons, we tried to apply both the analyses for the 3-leading-particle selection method to jets in the data. The procedure of the analysis was identical to that performed for the τ events.
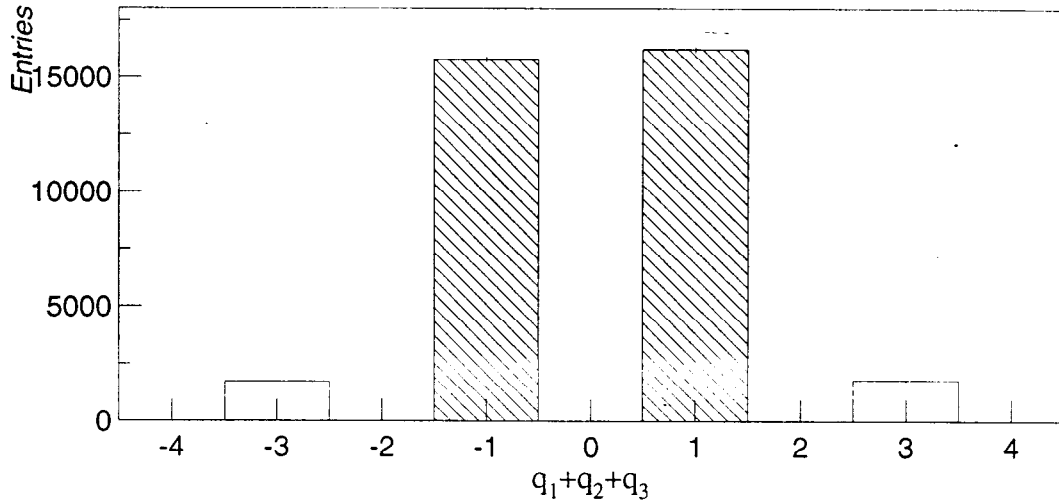
Figure 4.17: Distribution of sum of charges of fastest 3 particles in a jet. Jets falling into hatched bins were used in this analysis.

Figure 4.17 shows the distribution of the sum of the charges of the 3 leading charged particles. About 10% of jets have a sum of charges of -3 or $+3$. If the 3 tracks take positive or negative charge at random, 25% of jets would have such charges. The distribution seems to reflect the transport of the charge of a parton through the fragmentation process. Jets with the sum of charges of -1 or $+1$ were used in the analysis.

Figure 4.18 shows distributions of the two invariant masses of $\pi^+\pi^-$ with the Dalitz plot of the 3-π system ($\pi^+\pi^+\pi^-$ or $\pi^-\pi^-\pi^+$). The distribution of the invariant mass of the 3-π system is also shown in the figure. Although clear resonances were not seen, Ω_{hel} and Ω_{chi} were defined for each jet using the 3 leading particles which satisfy the criteria for the invariant masses of the 2-π and 3-π systems. Such jets are indicated by the hatched histogram in bottom-left of Figure 4.18.

Distributions of Ω_{hel}, $\Omega_{mod.hel}$ and Ω_{chi} are shown for the global, light flavor and heavy flavor samples in Figure 4.19, Figure 4.21 and Figure 4.20, respectively. The calculations of the measured handedness and the procedure for extracting the analyzing power α were exactly the same as those performed for the τ events. For the chirality-based analysis, the calculation and procedure were almost the same as those for the τ events, except for the polarization of quark and antiquark, $\mathcal{P}_{chi}$. $\mathcal{P}_{chi}$ (Equation (2.29)) was averaged over the flavor composition of each sample, estimated from the simulations and weighted by the sign of the quark charge. $\mathcal{P}_{chi}$ for each
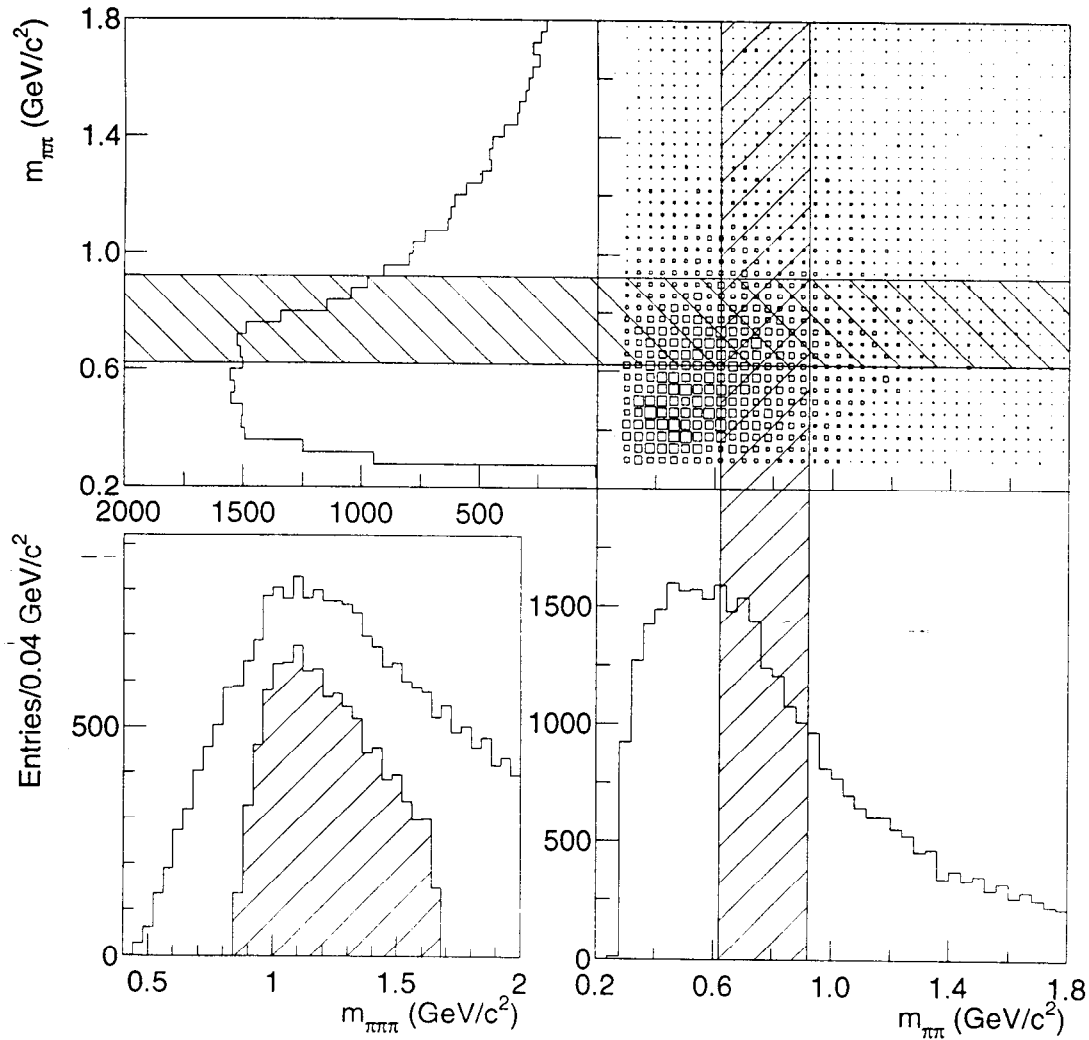
Figure 4.18: Distributions of invariant masses and the Dalitz plot of 3-π system. The top-left and bottom-right figures show two invariant masses of $\pi^+\pi^-$ pairs, $m_{\pi\pi}$. Hatched regions in these two figures represent the criteria (in text) for the invariant mass of $\pi^+\pi^-$. The bottom-left figure shows the distribution of the invariant mass for the 3-π system, $m_{\pi\pi\pi}$. The hatched histogram in the bottom-left figure represents the triplets lying in the overlap region in the Dalitz plot (top right) and satisfying the criteria (in text) for the invariant mass of the 3-π system.

Figure 4.19: Ω distributions for the helicity- (top), modified helicity- (middle) and chirality-based (bottom) analyses for the global sample. The left and right figures show the distributions for jet in left- and right-handed electron beam events. Solid and dashed histograms show the distributions of Ω_{hel} for jets pointing forward ($\cos\theta > 0.$) and backward ($\cos\theta < 0.$), respectively.

Figure 4.20: Ω distributions for the helicity- (top), modified helicity- (middle) and chirality-based (bottom) analyses for the light flavor sample. The left and right figures show the distributions for jet in left- and right-handed electron beam events. Solid and dashed histograms show the distributions of Ω_{hel} for jets pointing forward ($\cos\theta > 0.$) and backward ($\cos\theta < 0.$), respectively.

Figure 4.21: Ω distributions for the helicity- (top), modified helicity- (middle) and chirality-based (bottom) analyses for the heavy flavor sample. The left and right figures show the distributions for jet in left- and right-handed electron beam events. Solid and dashed histograms show the distributions of Ω_{hel} for jets pointing forward ($\cos\theta > 0.$) and backward ($\cos\theta < 0.$), respectively.

Analysis	Analyzing Power		
	Global	Light flavor	Heavy flavor
Helicity	-0.029 ± 0.024	-0.057 ± 0.031	0.007 ± 0.036
Modified Helicity	0.055 ± 0.024	0.056 ± 0.032	0.055 ± 0.036
Chirality	-0.001 ± 0.026	0.052 ± 0.038	-0.058 ± 0.035

Table 4.5: Analyzing powers for the helicity-, modified helicity- and chirality-based analyses.

sample is given in Table 4.3.

The measured handedness and the results of the fitting are shown as a function of $\cos\theta$ in Figure 4.22, 4.23 and 4.24, for the global, light- and heavy-flavor samples. Since the light- and heavy-flavor samples are independent of each other, there is no correlation in results from those two samples. However, the global one is sum of these two samples, therefore, results from the sample is correlated with those from the light- and heavy-flavor samples.

Most of the measured handedness (shown as points) is consistent with zero within 2σ. Angular dependence is not seen in the helicity-based handedness. However, the modified helicity-based handedness for the three samples seems to slightly depend on $\cos\theta$ and $\mathcal{P}$. The chirality-based handedness is scattered randomly in all $\cos\theta$ region. The fitted analyzing powers for all three analyses with the three samples are listed in Table 4.5.

The small angular dependence of the modified helicity-based handedness gives slightly large analyzing powers for the three samples. The analyzing power for the global sample is most significant among others and is away from zero by 2.3σ. The other analyzing powers are consistent with zero within 2σ.

Dependence on Invariant Mass Cut The 3-particle selection method uses interference phenomena in $a_1 \to \rho\pi \to \pi\pi\pi$ to measure the polarization of quark and antiquark. Therefore, it is useful to estimate the amounts of a_1 and ρ mesons included in the samples. The amounts depend on the invariant mass cut applied to the 3-π and 2-π system. We expect the handedness signal to decrease as the amounts decrease.

Figure 4.25 shows invariant mass distributions of the 3-π system and the 2-π system. The ρ resonance of can be seen around $0.73\mathrm{GeV}/c^2$. The resonance is fitted to a Gaussian plus quadratic and the fit gives 0.73 as the peak value and 0.05 as the width of the Gaussian distribution. However, an a_1-meson resonance can not be seen in the figure. This may imply that the handedness signal will be small.
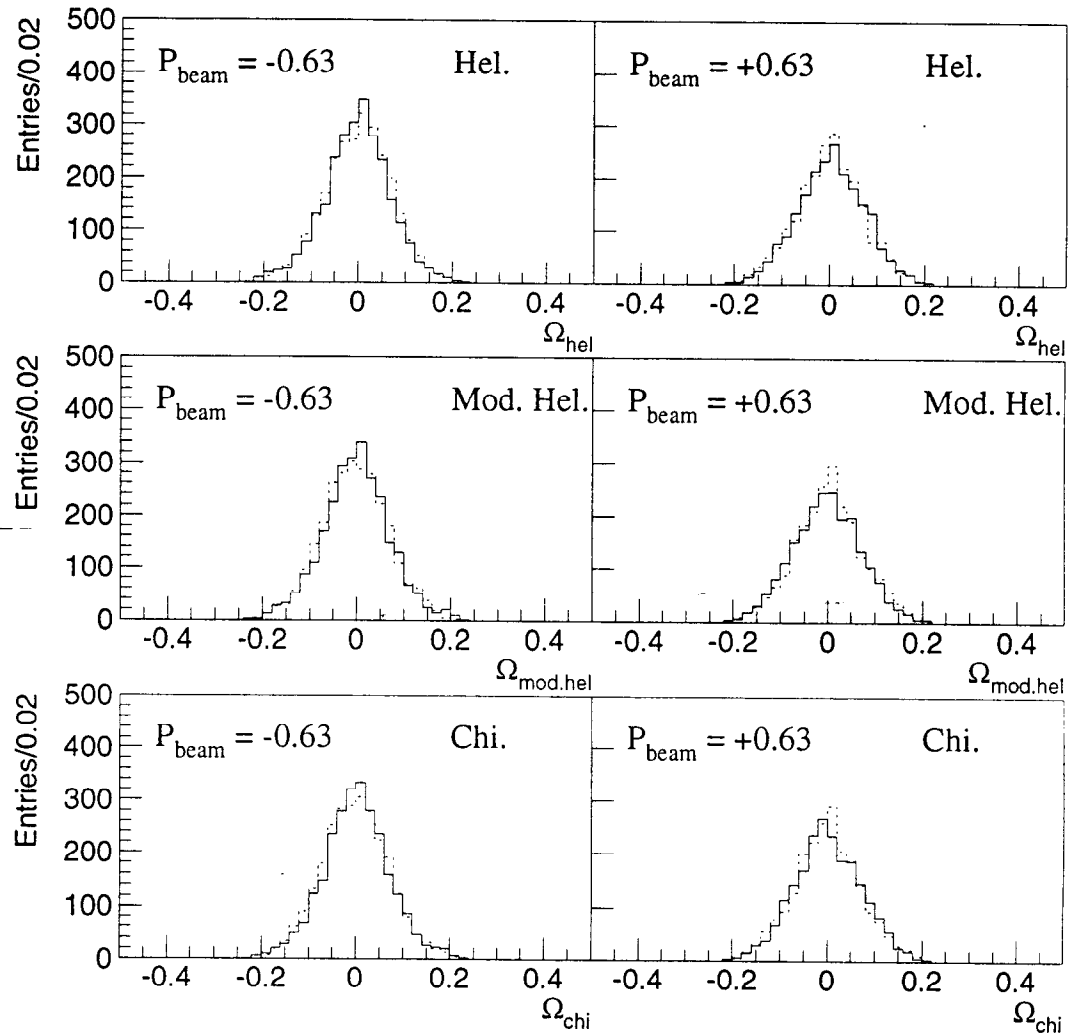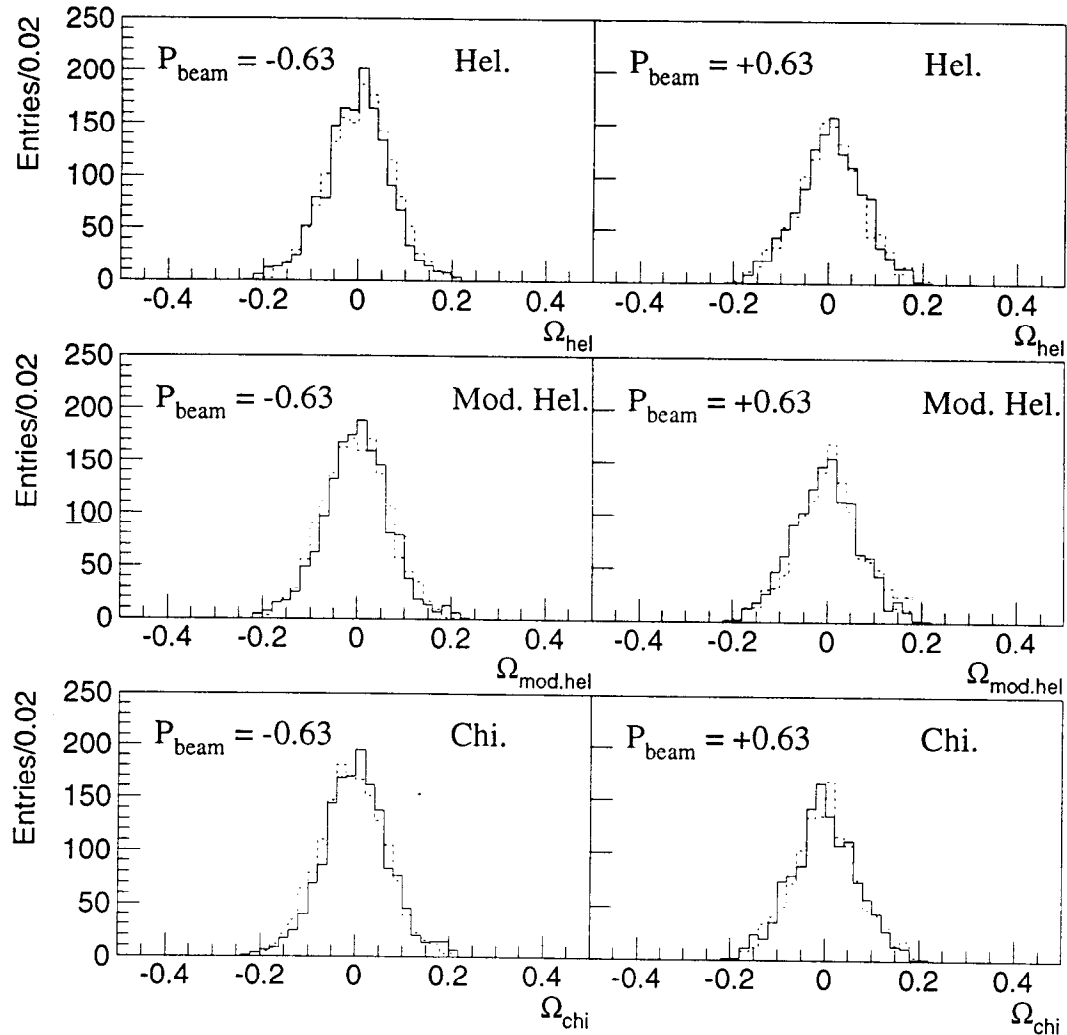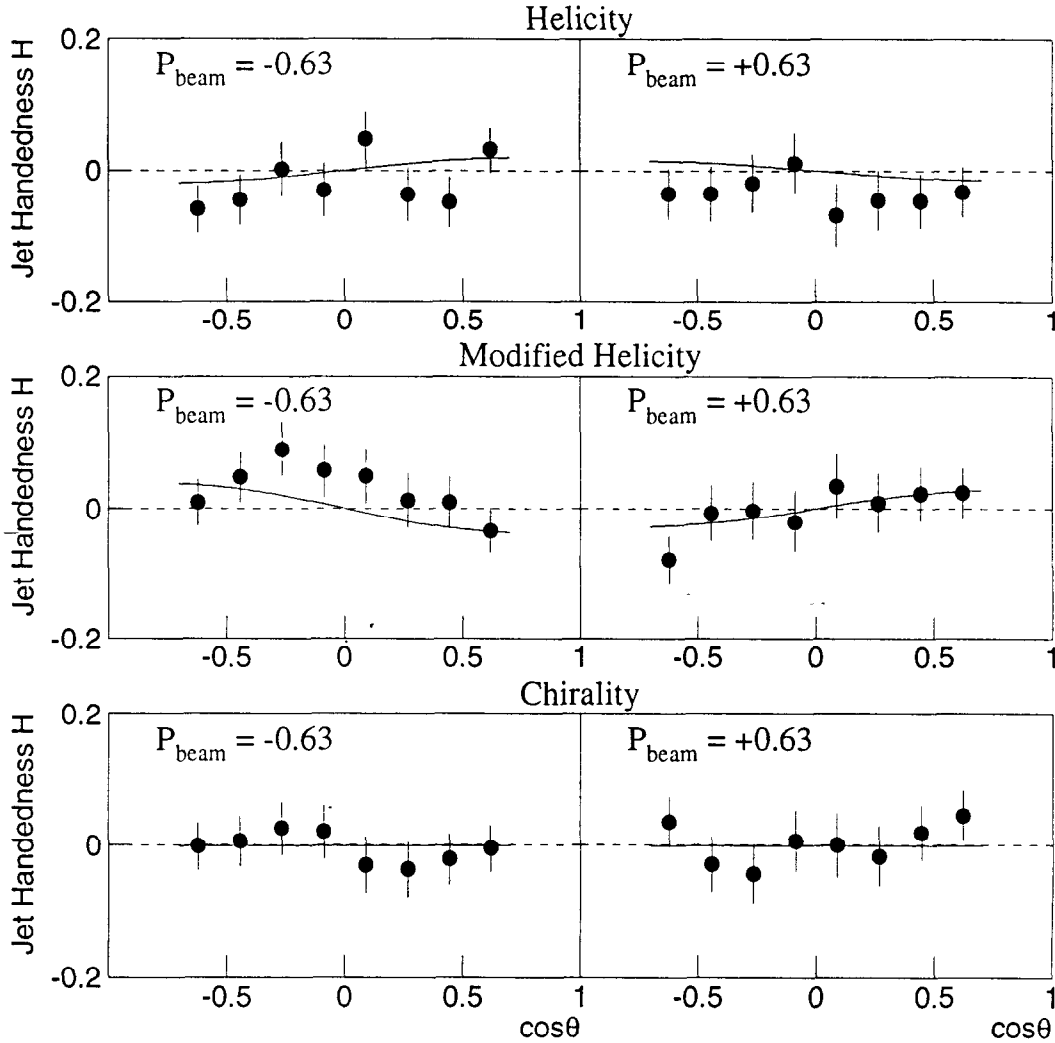
Figure 4.22: Jet handedness as a function of the jet direction $\cos\theta$ for the helicity- (top), modified helicity- (middle) and chirality-based (bottom) analyses for the global sample. Events were divided into left- (left) and right-handed (right) events. Solid curves are the results of the best fit of Equations (4.8), (4.9) and (4.10) to data and the reduced χ^2s of the fits are 0.95, 0.73 and 0.41 for the helicity-, modified helicity- and chirality-based analyses, respectively. The data were limited to the region $-0.71 < \cos\theta < 0.71$ by the detector acceptance.
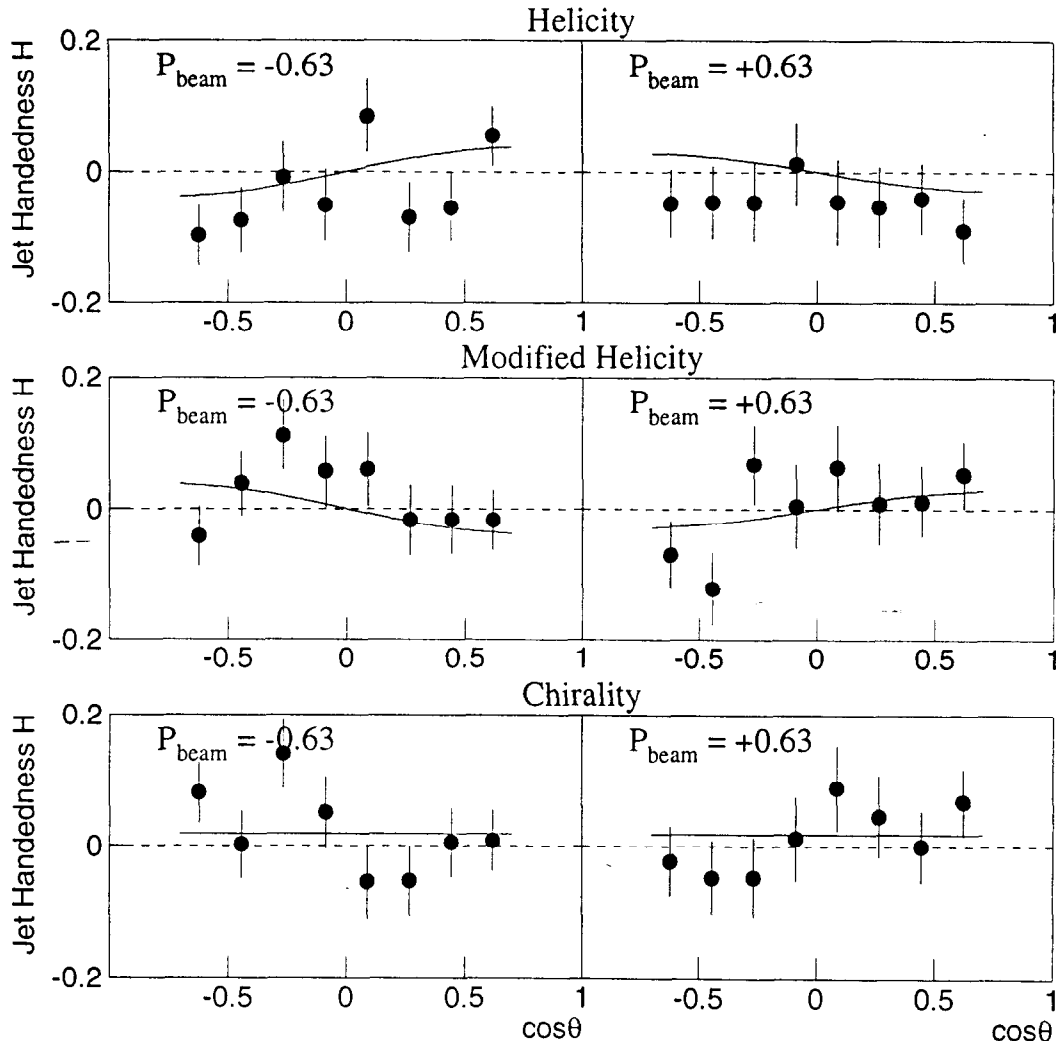
Figure 4.23: Jet handedness as a function of the jet direction $\cos\theta$ for the helicity- (top), modified helicity- (middle) and chirality-based (bottom) analyses for the light-flavor sample. Events were divided into left- (left) and right-handed (right) events. Solid curves are the results of the best fit of Equations (4.8), (4.9) and (4.10) to data and the reduced χ^2s of the fits are 1.19, 1.01 and 1.10 for the helicity-, modified helicity- and chirality-based analyses, respectively. The data were limited to the region $-0.71 < \cos\theta < 0.71$ by the detector acceptance.
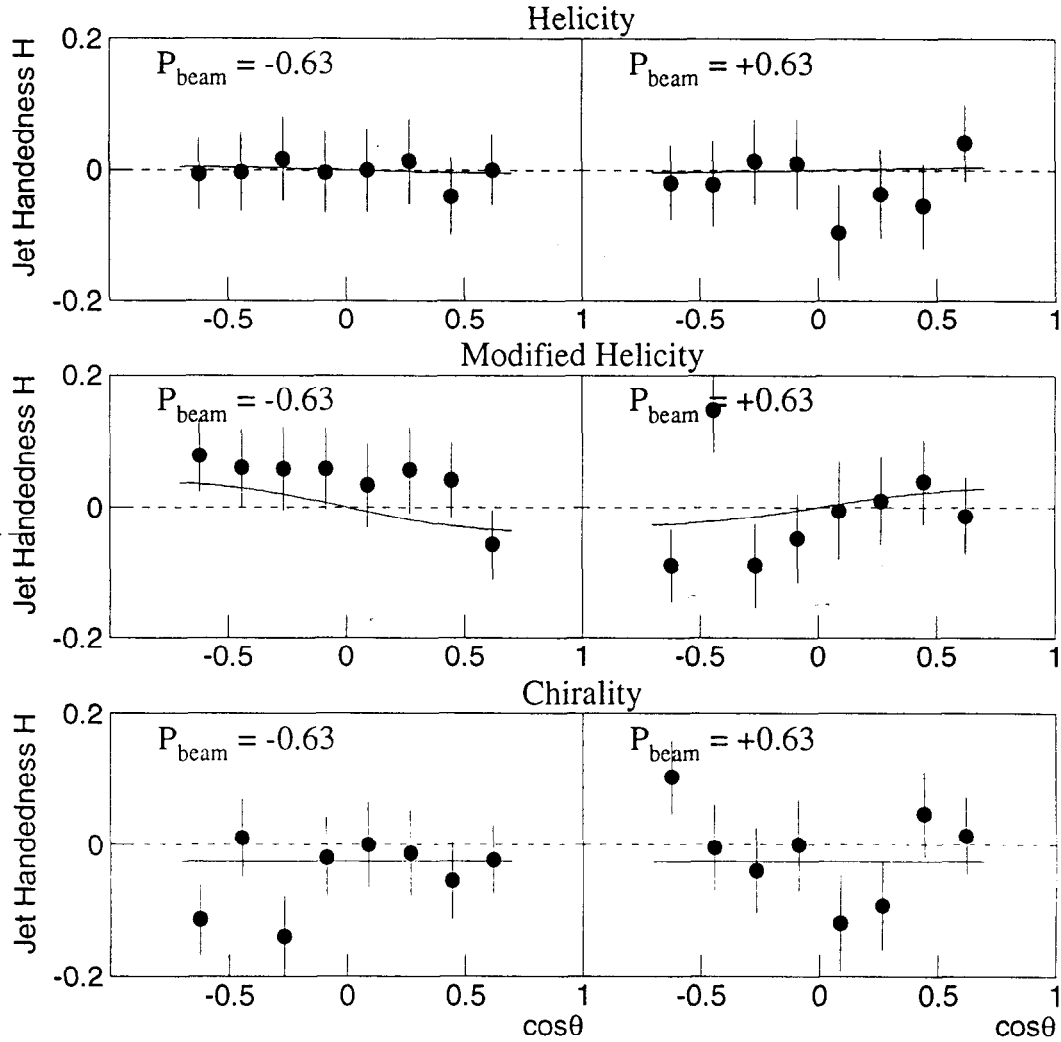
Figure 4.24: Jet handedness as a function of the jet direction $\cos\theta$ for the helicity- (top), modified helicity- (middle) and chirality-based (bottom) analyses for the heavy-flavor sample. Events were divided into left- (left) and right-handed (right) events. Solid curves are the results of the best fit of Equations (4.8), (4.9) and (4.10) to data and the reduced χ^2s for the fts are 0.27, 1.05 and 1.09 for the helicity-, modified helicity- and chirality-based analyses, respectively. The data were limited to the region $-0.71 < \cos\theta < 0.71$ by the detector acceptance.
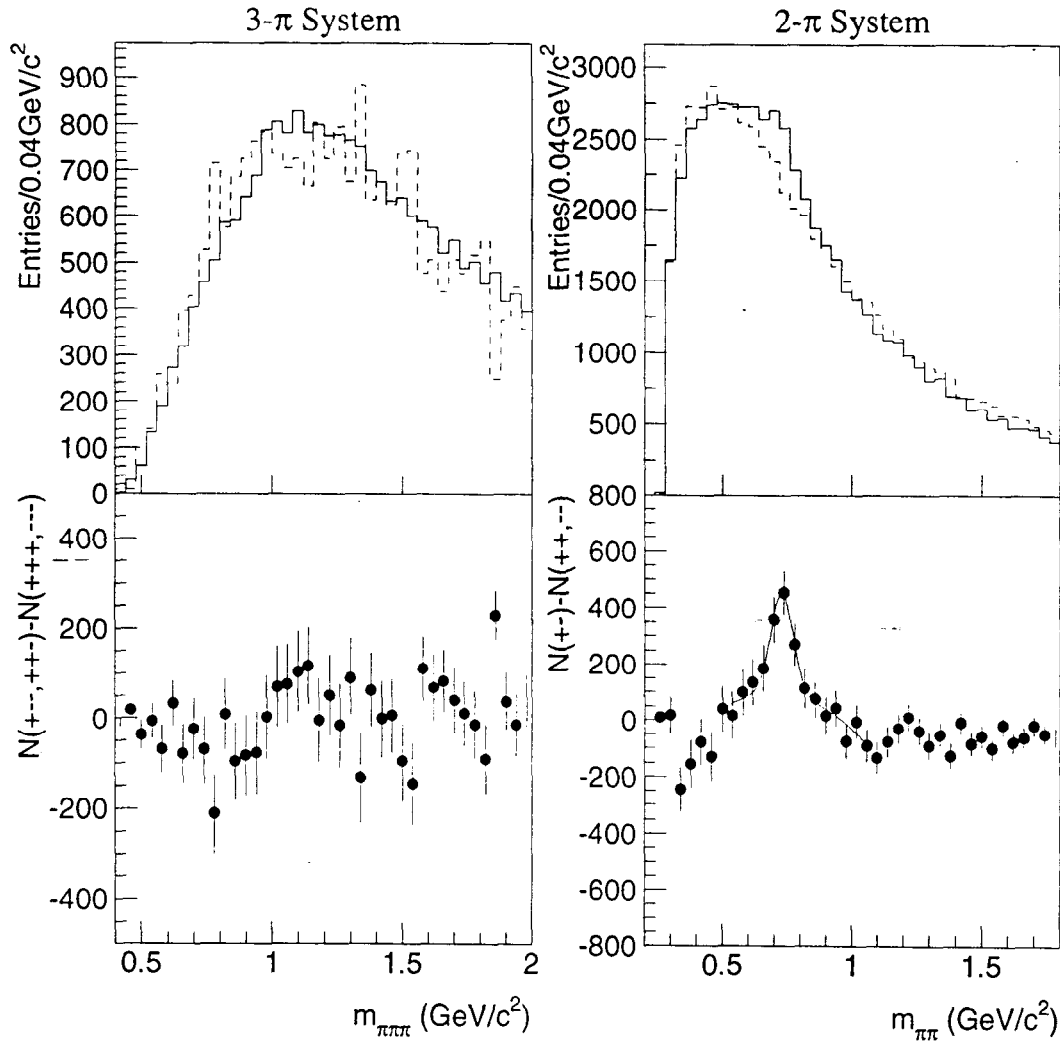
Figure 4.25: Masses of the 3-π and 2-π systems. The two top figures show invariant mass distributions of the 3-π (top-left) and 2-π (top-right) systems. Invariant masses of $\pi^+\pi^-\pi^-$ and $\pi^+\pi^+\pi^-$ for the 3-π system and those of $\pi^+\pi^-$ for the 2-π system are shown as solid histograms. Dashed histograms show invariant masses of like-sign triplets and pairs, i.e. $\pi^+\pi^+\pi^+, \pi^-\pi^-\pi^-$ and $\pi^+\pi^+, \pi^-\pi^-$ for the 3-π and 2-π systems, respectively. Entries in dashed histograms are normalized to that in solid histograms. The two bottom figures show the results from bin-by-bin subtraction of dashed histograms from solid ones.

To investigate the dependence of jet handedness on the applied invariant mass cut, three cuts were considered in addition to the standard invariant mass cut (cut 1) shown in Section 4.5:

no cut no invariant mass cut applied,

cut 1 $0.82\text{GeV}/\text{c}^2 < m_{\pi\pi\pi} < 1.62\text{GeV}/\text{c}^2$ for the 3-π system and $0.62\text{GeV}/\text{c}^2 < m_{\pi\pi} < 0.92\text{GeV}/\text{c}^2$ for one of the two 2-π systems,

cut 2 $1.02\text{GeV}/\text{c}^2 < m_{\pi\pi\pi} < 1.42\text{GeV}/\text{c}^2$ for the 3-π system and $0.695\text{GeV}/\text{c}^2 < m_{\pi\pi} < 0.845\text{GeV}/\text{c}^2$ for one of the two 2-π systems, and

cut 3 $0.82\text{GeV}/\text{c}^2 < m_{\pi\pi\pi} < 1.62\text{GeV}/\text{c}^2$ for the 3-π system and $0.62\text{GeV}/\text{c}^2 < m_{\pi\pi} < 0.92\text{GeV}/\text{c}^2$ for BOTH of the two 2-π systems (1*1 cut).

Figure 4.26 shows dependence of the analyzing power on the invariant mass cuts. All points in each figure are correlated with each other. The no invariant mass cut tends to give small analyzing powers for all analyses with each sample. Excepting that, a dependence on the invariant mass cuts is not obvious.

Dependence on y_{cut} As the y_{cut} value increases, the contamination of 3-or-more-jet events in the samples increases. The thrust axis for these events does not represent the quark-antiquark axis. This means that the handedness signal may be dilute, as the contamination increases. Therefore, the dependence of analyzing power on the y_{cut} value was also checked. Figure 4.27 shows distribution of $y_{cut}(3 \to 2)$ value for which an event changes from 3 jets to 2 jets. Events with large $y_{cut}(3 \to 2)$ value are multi-jet events, and those with small one are 'pencil-like' 2-jet events. The handedness signal may be larger for the events with small $y_{cut}(3 \to 2)$ value.

Figure 4.28 shows dependence of the analyzing power on y_{cut} value. Each analyzing power for each y_{cut} value is determined with events with the $y_{cut}(3 \to 2) \leq y_{cut}$, therefore, points in each figure are also correlated with each other. The analyzing power seems not to depend on the y_{cut} value and all analyzing powers are the same within their statistical errors for all analysis with each sample.

Dependence on Charged track multiplicity in a Jet The dependence of the analyzing power on charged track multiplicity in a jet was also checked. The analyzing powers were determined for the following samples:

jet samples 1 jets containing N charged tracks and

jet samples 2 jets containing N OR LESS charged tracks,

75
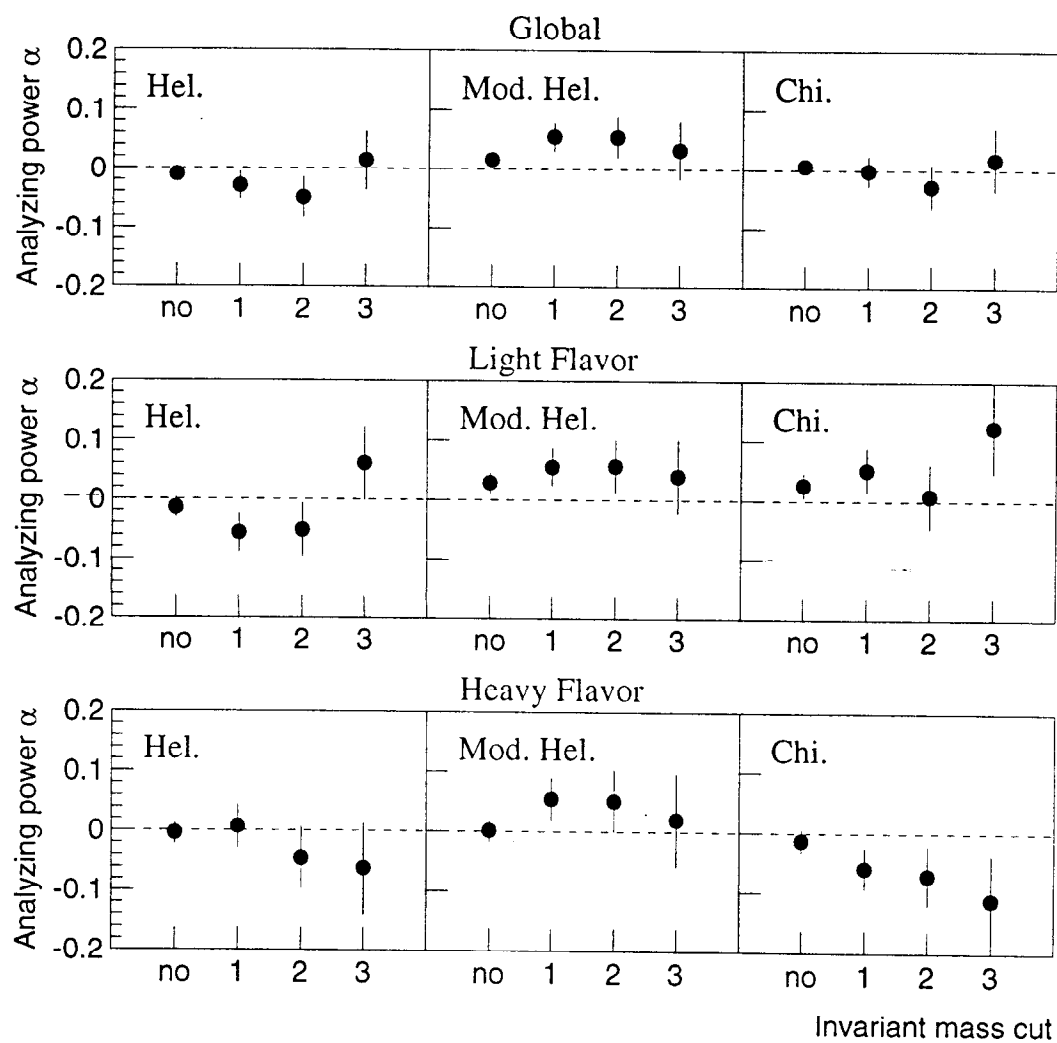
Figure 4.26: Dependence of the analyzing power on the invariant mass cut. Each of the four cuts (no, 1, 2 and 3) is defined in text. All results in each figure are correlated with each other.
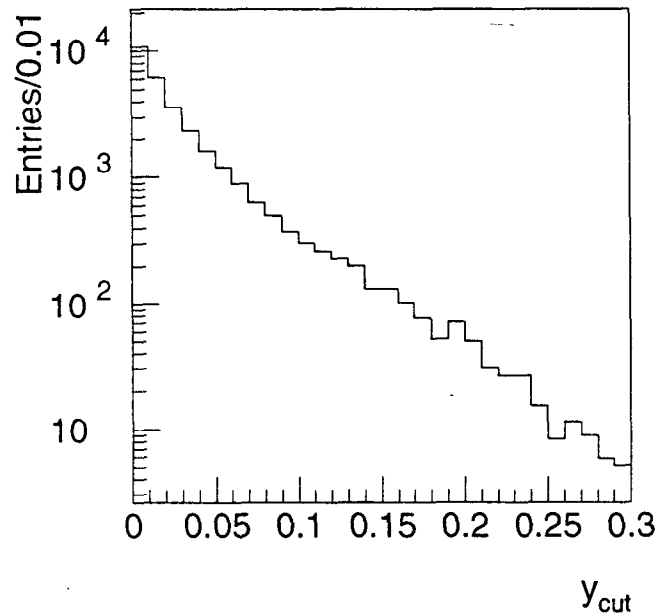
Figure 4.27: Distribution of $y_{cut}(3 \to 2)$ value for which an event changes from 3 jets to 2 jets.

where N is a number in the range $3 \leq N \leq 13$. Therefore, all jets are divided into a set of 11 jet samples for both cases. A set of jet samples 1 consists of 11 samples which is independent of each other so that the resulting analyzing powers are independent. However, 13 samples of the jet samples 2 are correlated with each other so that the resulting analyzing power is correlated.

Figure 4.29 shows dependence of the analyzing power on the charged-track-multiplicity in a jet. Because of poor statistics, we can not see a dependence of the analyzing power for the jet samples 1 on the multiplicity, but the analyzing power in the low multiplicity region seems to have a slightly larger value for the chirality-based analysis. Statistics of the jet samples 2 is also poor in the low multiplicity region, however, all analyzing powers are consistent with each other within their statistical errors.
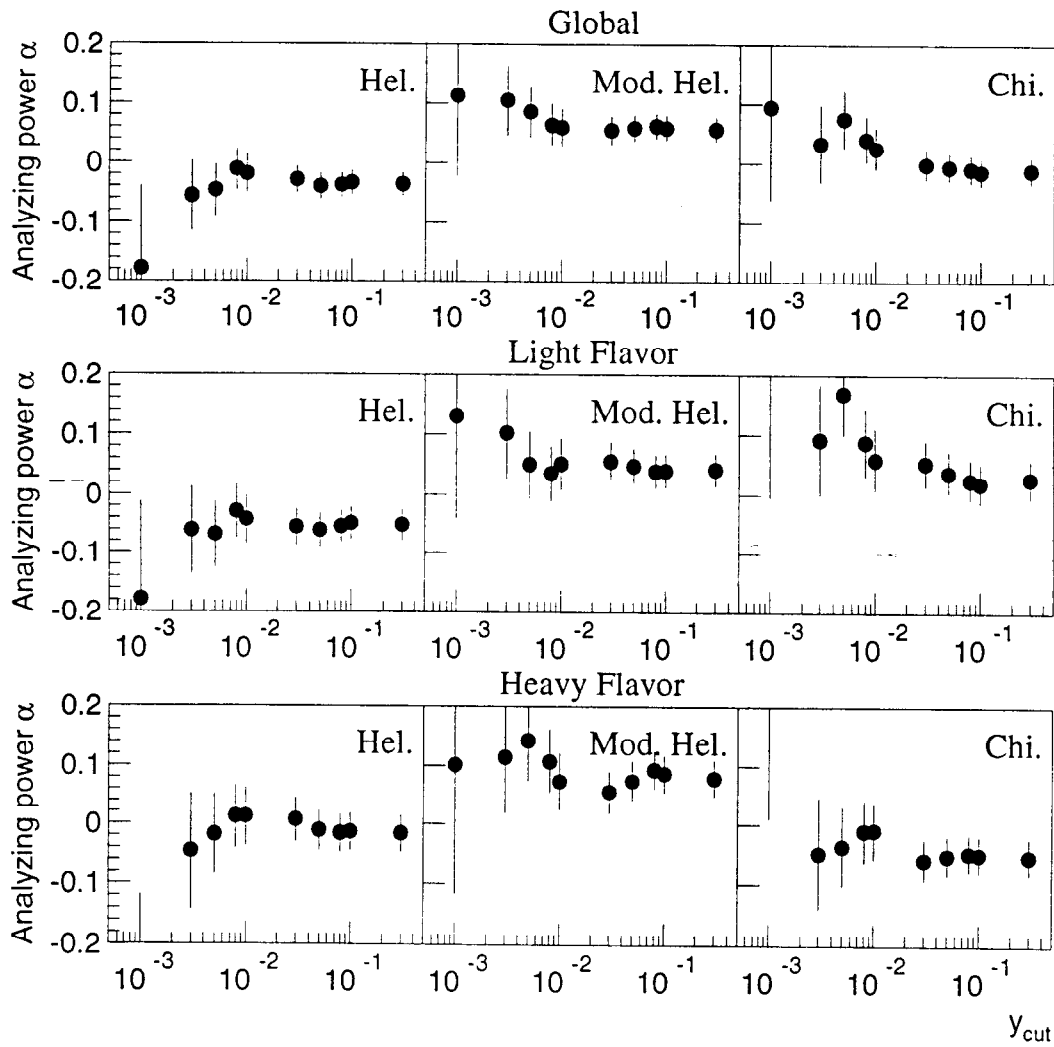
Figure 4.28: Dependence of the analyzing power on y_{cut} value. All points in each figure are correlated with each other.
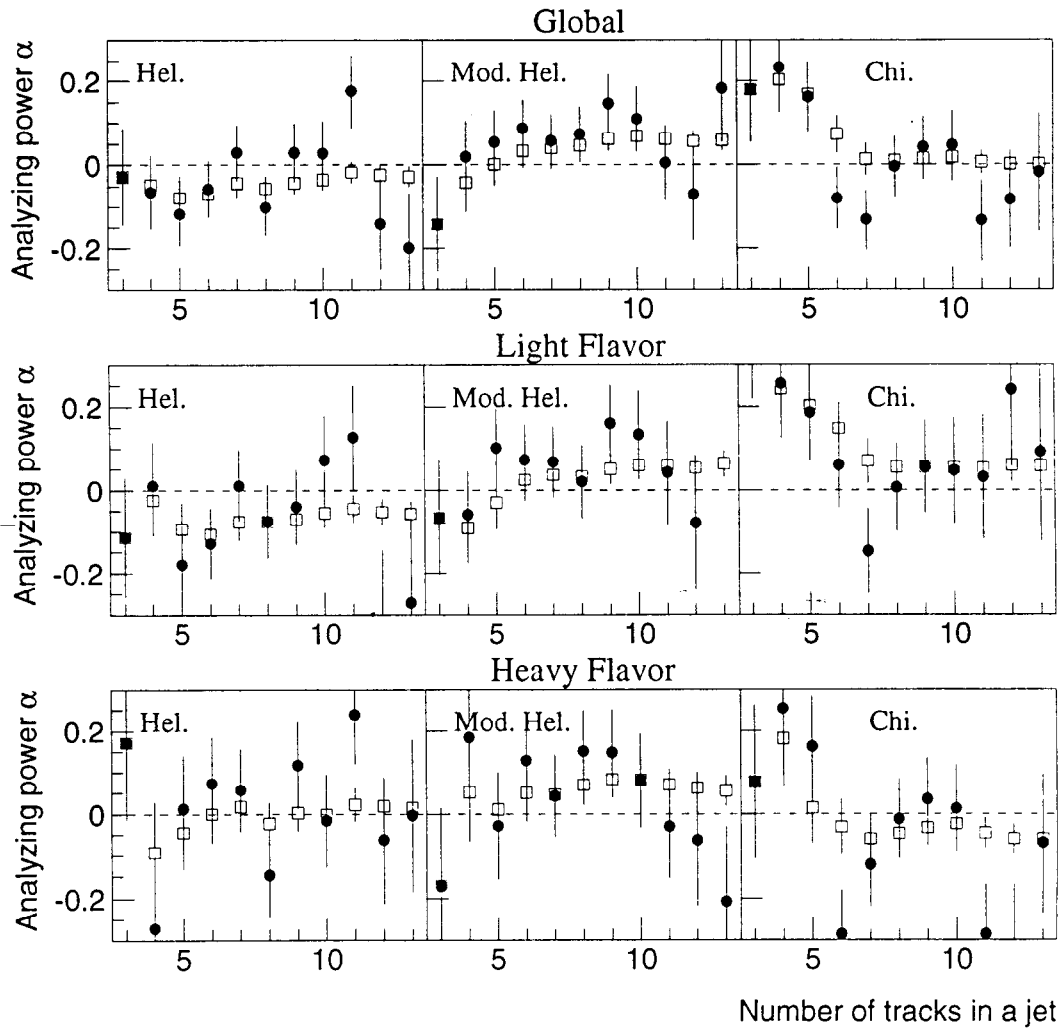
Figure 4.29: Dependence of the analyzing power on charged track multiplicity in a jet. Each point shows the analyzing power for a sample of jets containing N charged tracks, therefore all points are independent. N is a number in the range $3 \leq N \leq 13$. However, each open square shows the analyzing power for a sample of jets containing N or less charged tracks. This means that all squares are correlated with each other.

4.6 N Leading Particle Selection Method

This method is one of the general extensions of the 3-leading-particle selection method.

The procedure of this method was the following:

1. $N_{lead}(\geq 3)$ charged particles were selected from each jet in order of the magnitude of their momenta. All zero-charge pairs i, j among these N_{lead} particles were considered as samples without applying the invariant mass criteria used in the preceding method.

2. Ω_{hel}^{ij} and $\Omega_{chi}^{i'j'}$ were calculated for each pair:

$$\Omega_{hel}^{ij} = \hat{t} \cdot (\vec{k}_i \times \vec{k}_j)$$
$$\Omega_{chi}^{i'j'} = \hat{t} \cdot (\vec{k}_{i'}^{+} \times \vec{k}_{j'}^{-})$$

where $\vec{k}_i$, $\vec{k}_j$ were momenta of two particles chosen from the N_{lead} particles boosted to the N_{lead}-particle rest frame, and $|\vec{k}_i| > |\vec{k}_j|$. The pair of particles, $\vec{k}_{i'}^{+}$, $\vec{k}_{j'}^{-}$ were identical to $\vec{k}_i$, $\vec{k}_j$ except that $\vec{k}_{i'}^{+}$ was one of $\vec{k}_i$, $\vec{k}_j$ with positive charge, and $\vec{k}_{j'}^{-}$ was the other with negative charge. If a jet did not have N_{lead} particles, the jet was excluded from the analysis.

3. The average over Ω^{ij}, $\langle \Omega^{ij} \rangle$ (*average* method), and the Ω^{ij} with largest magnitude, Ω^{max} (*maximum* method) were used for the analysis:

$$\langle \Omega^{ij} \rangle = \frac{1}{N_{pairs}} \sum_{i,j}^{N_{lead}} \frac{\Omega^{ij}}{|\Omega^{ij}|}$$
$$\Omega^{max} = \max(|\Omega^{ij}|)\text{sign}(\Omega^{ij})$$

where N_{pairs} was the number of the combinations of positive and negative charged particles in the N_{lead} particles. sign (Ω^{ij}) is sign of Ω^{ij} which is the largest one in magnitude. The notation, Ω^{ij} refers to either Ω_{hel}^{ij} or $\Omega_{chi}^{i'j'}$ for the helicity- or chirality-based analysis, respectively.

4. Jet handedness for the global, light and heavy flavor samples was calculated for each N_{lead} value for the both helicity- and chirality-based analyses in the same manner as the 3-leading-particle method.

There are two differences between this method and the 3-leading-particle method; In the present method, more than 3 particles are used for the calculation
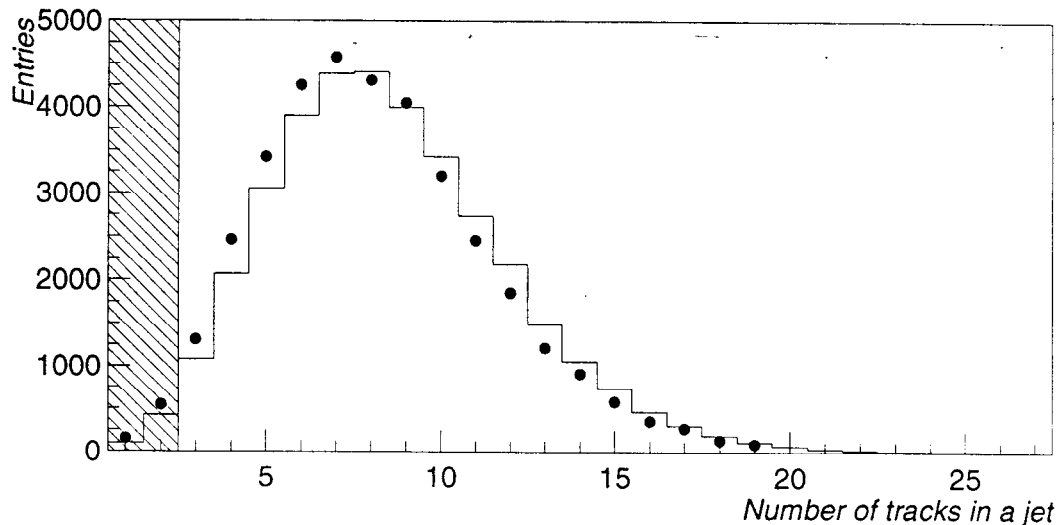
Figure 4.30: Distribution of charged track multiplicity in a jet. Shown are data (points) and the Monte Carlo simulation (histogram). The average multiplicity is about 8.5. Since N_{lead} was 3 or more, jets containing 2 or less tracks (binned in hatched region) were removed beforehand. Due to poor statistics of high multiplicity jets, the N_{lead} value was set in a region of $3 \leq N_{lead} \leq 17$.

of Ω. Further, this method does not require invariant mass criteria for a pair and a triplet as applied in the preceding method.

The main advantage of the method is that the polarization information is efficiently scooped from more than 3 particles. The method, however, has a risk to make the information smeared out because particles with no information of parton polarization may be used. The optimum number of particles to be selected may exist.

Figure 4.30 shows the distribution of number of charged tracks in a jet (*charged track multiplicity* in a jet). The average of the charged track multiplicity in a jet was about 8.5. The N_{lead} value was set in a region of $3 \leq N_{lead} \leq 17$, because the statistics got poor in the high multiplicity region.

Figure 4.31 shows the analyzing power obtained for each N_{lead} value for the global, light flavor and heavy flavor samples. No analyzing power is plotted for the chirality-based analysis with $N_{lead} = 3$, since the chirality-based analysis always gives zero Ω_{chi} resulting in zero jet handedness due to the definition. Same kind symbols in each figure are correlated with each other. The analyzing powers of the average and maximum method have opposite sign in the region of small N_{lead} for the three samples for the chirality-based analysis. Both analyzing powers are at about 2σ of
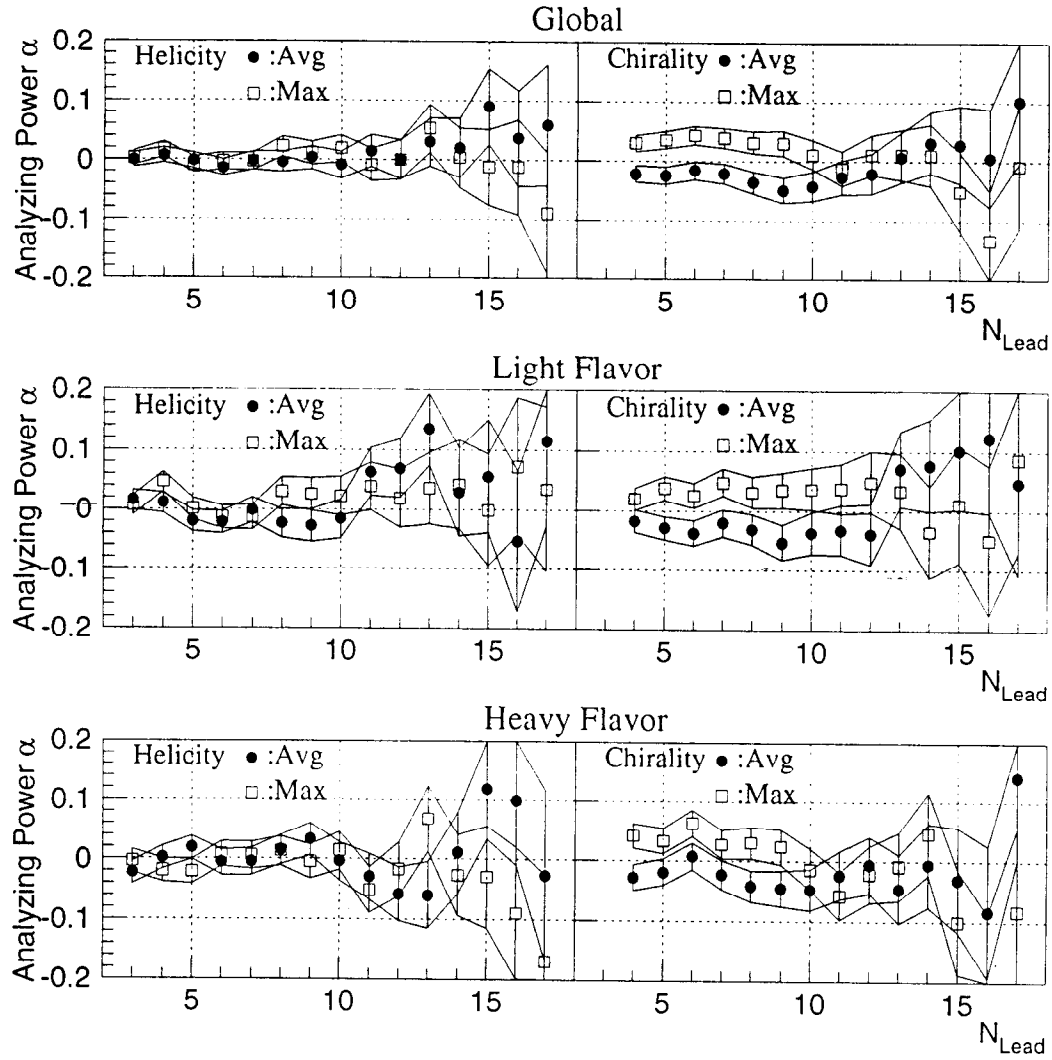
Figure 4.31: Dependence of the analyzing power on N_{lead} for the global (top), light (meddle) and heavy flavor samples (bottom). The left and right figures show the analyzing power for the helicity- and chirality-based analyses, respectively. Shown are the average method (points) and maximum method (open squares).

their statistical errors away from zero, but there is no apparent dependence on N_{lead}. It seems that the analyzing power is independent of N_{lead} and has a value within 2σ away from zero for all N_{lead} values. We found no optimum number for enhancing the analyzing power through all N_{lead} values from Figure 4.31.

4.7 Particle Selection Method based on Rapidity and Momentum

This method is based on the assumption that jet handedness is ascribed to fragmentation phenomena [8] as shown in Section 2.8. According to the model, the polarization effects may appear in angular distribution of hadrons produced from a same string break up. Therefore, it is essential to select pairs of particles likely to be produced by such a string break up.

Studies using JETSET 6.3[29] showed that it is useful to select a pair of tracks according to the difference in the rapidity with respect to the jet axis of the particles in the pair[41]. Requiring zero charge of a pair is not needed for the selection of particles from the same string break up, but the condition was used in the chirality-based analysis. The procedure is the following.

1. Charged particles in each jet were ordered in their rapidity:

$$y_i = \frac{1}{2}\ln\frac{E_i + p_{\|i}}{E_i - p_{\|i}}$$

   where E_i and $p_{\|i}$ were energy and longitudinal momentum of particle i with respect to the thrust axis, signed so as to point along the jet axis. Each track i was assigned a number $1 \le n_i \le n_{tracks}$, where $n_i = 1$ for the particle with the highest rapidity.

2. A pair of charged particles i, j was required to have $\max(n_i, n_j) \le n_{max}$ and $|n_i - n_j| < \Delta n$.

3. Since the signal was expected to increase with transverse momentum p_t with respect to the thrust axis as mentioned in Section 2.8, $|p_{ti}| + |p_{tj}| > p_{min}$ was required for pairs of tracks, where p_{min} is a parameter to be tried to vary.

4. Ω_{hel}^{ij} and $\Omega_{chi}^{i'j'}$ were calculated in the laboratory frame for each pair satisfying these criteria:

$$\begin{aligned}
\Omega_{hel}^{ij} &= \hat{t} \cdot (\vec{k}_i \times \vec{k}_j) \\
\Omega_{chi}^{i'j'} &= \hat{t} \cdot (\vec{k}_{i'}^{+} \times \vec{k}_{j'}^{-})
\end{aligned}$$

83

where $\vec{k}_i$, $\vec{k}_j$ were momenta of two particles in the laboratory frame chosen from N_{lead} of the leading particles and $|\vec{k}_i| > |\vec{k}_j|$. The tracks, $\vec{k}_{i'}^+$, $\vec{k}_{j'}^-$ were identical to $\vec{k}_i$, $\vec{k}_j$ and $\vec{k}_{i'}^+$ was one of $\vec{k}_i$, $\vec{k}_j$ with positive charge, and $\vec{k}_{j'}^-$ was the other with negative charge. Both the average, $\langle \Omega^{ij} \rangle$ (*average* method), and the maximum, Ω^{ij} with largest magnitude, Ω^{max} (*maximum* method) were considered:

$$\langle \Omega^{ij} \rangle = \frac{1}{N_{pairs}} \sum_{\substack{|n_i - n_j| \leq \Delta n}}^{n_{max}-1} \frac{\Omega^{ij}}{|\Omega^{ij}|}$$

$$\Omega^{max} = \max(|\Omega^{ij}|)\mathrm{sign}(\Omega^{ij})$$

where N_{pair} is the number of combinations of two particles which satisfy the criteria on n_{max}, Δn and p_{min}. sign (Ω^{ij}) is sign of Ω^{ij} which is the largest one in magnitude. The notation Ω^{ij} was used to refer to Ω_{hel}^{ij} or $\Omega_{chi}^{i'j'}$ for the helicity- or chirality-based analysis, respectively.

5. In all cases, the jet handedness was calculated for the global, light and heavy flavor samples in the same manner as the 3-leading-particle selection method.

6. n_{max}, Δn and p_{min} were varied in an attempt to maximize the handedness signal.

Figure 4.32 and Figure 4.33 show the distributions of the rapidity, y and transverse momentum, p_t with respect to the thrust axis pointing momentum of the jet, which is used as the jet axis. Figure 4.34, Figure 4.35 and Figure 4.36 show dependence of analyzing powers on n_{max}, Δn and p_{min} in the global, light flavor and heavy flavor samples, respectively. Same kind symbols in each figures are correlated with each other. On the assumption that particles with higher momenta carry more information on the underlying partons, n_{max} and Δn were varied in the regions $2 \leq n_{max} \leq 3$ and $1 \leq \Delta n \leq n_{max} - 1$, respectively. p_{min} was varied in the range $0 \leq p_{min} \leq 3.5$ GeV/c. However, the statistics of the present data became poor in the high p_{min} region where the handedness signal may be potentially large. In the case of the criteria $n_{max} = 2$ and $\Delta n = 1$, the averaged method (shown as points in the figures) produced the exactly same results as that for the maximum method (shown as open squares). Even though n_{max} is more than 2, it seems that the difference between those two results is quite small.

In the high p_{min} region, the analyzing power gets negative for the helicity-based method and it tends to be large and positive for the chirality-based analysis. However, in general, the analyzing power is consistent with zero within 2 σ of its statistical error in all p_{min} regions.
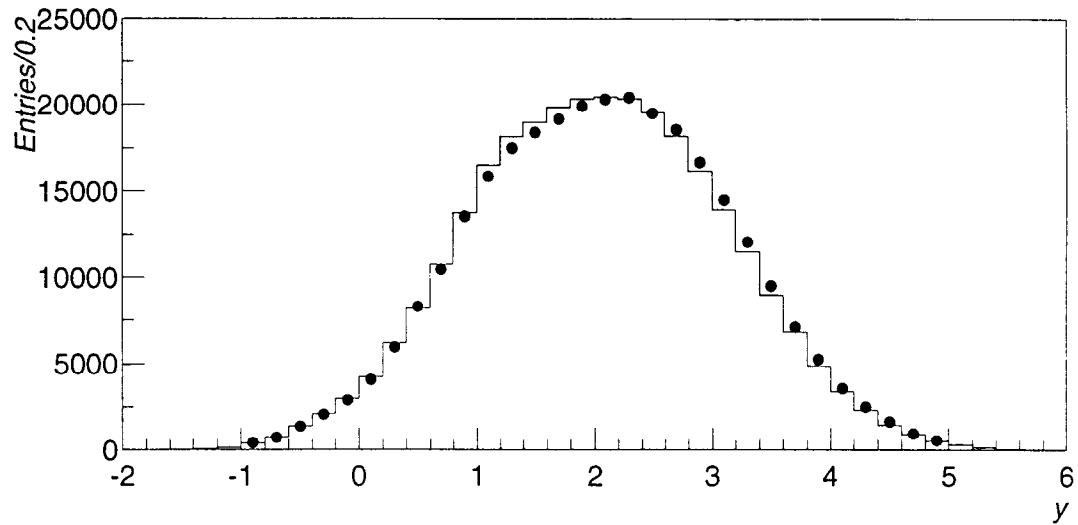
Figure 4.32: Distribution of rapidity of charged particles with respect to the jet axis. Shown are data (points) and the Monte Carlo simulation (histogram).
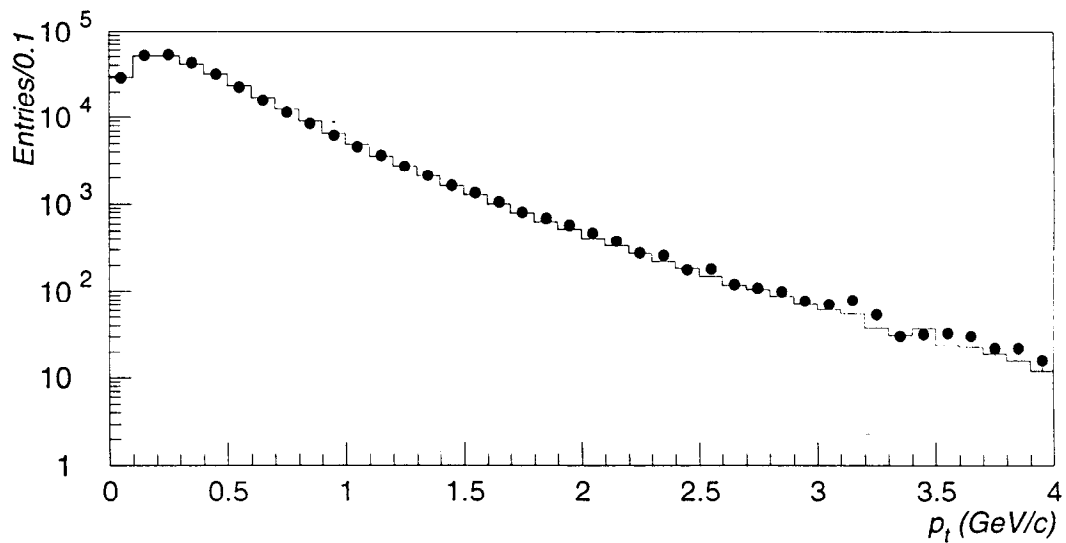
Figure 4.33: Distribution of transverse momentum of charged particles with respect to the jet axis. Shown are data (points) and the Monte Carlo simulation (histogram).
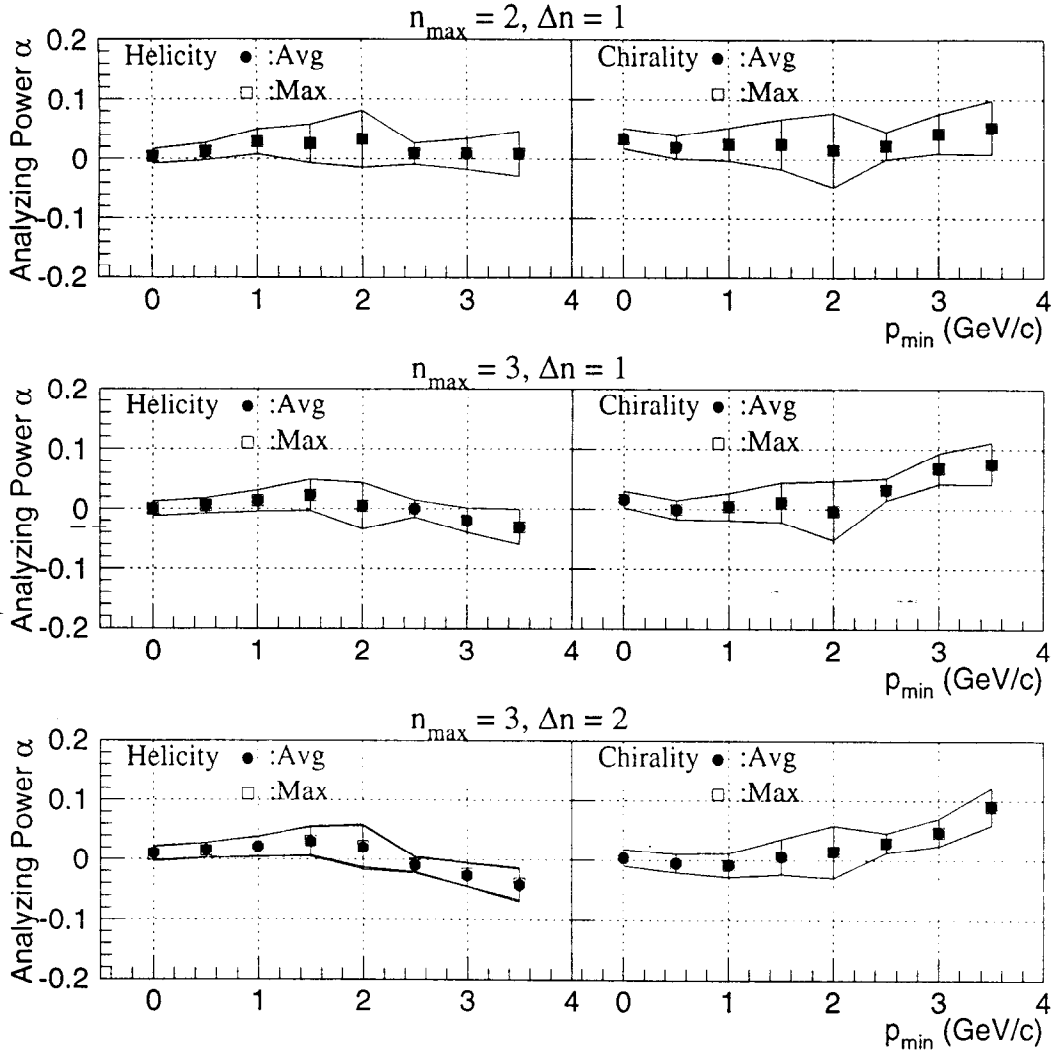
Figure 4.34: Dependence of the analyzing power on p_{min} for combinations of $(n_{max}, \Delta n) = (2, 1)$ (top), (3, 1) (middle) and (3, 2) (bottom) for the global sample. The left and right figures show the analyzing power for the helicity- and chirality-based analyses, respectively. Shown are the average (points) and maximum (open squares) methods. For $p_{min} \geq 2.5$ GeV/c, the analyzing powers are shown multiplied by 1/4, because the analyzing powers in the high p_{min} region have quite large values and errors compared to those in the low p_{min} region.
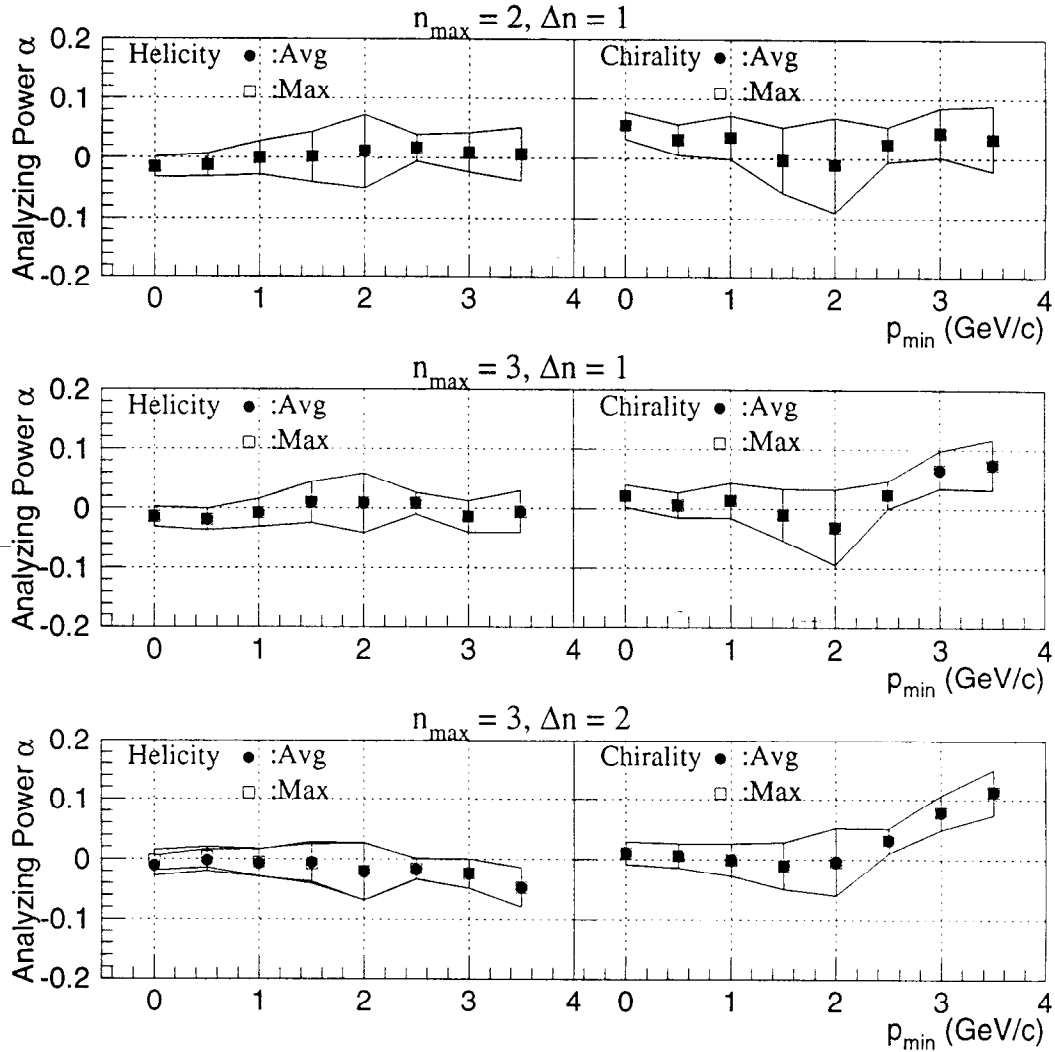
Figure 4.35: Dependence of the analyzing power on p_{min} for combinations of $(n_{max}, \Delta n) = (2, 1)$ (top), (3, 1) (middle) and (3, 2) (bottom) for the light flavor sample. The left and right figures show the analyzing power for the helicity- and chirality-based analyses, respectively. Shown are the average (points) and maximum (open squares) methods. For $p_{min} \geq 2.5$ GeV/c, the analyzing powers are shown multiplied by 1/4, because the analyzing powers in the high p_{min} region have quite large values and errors compared to those in the low p_{min} region.
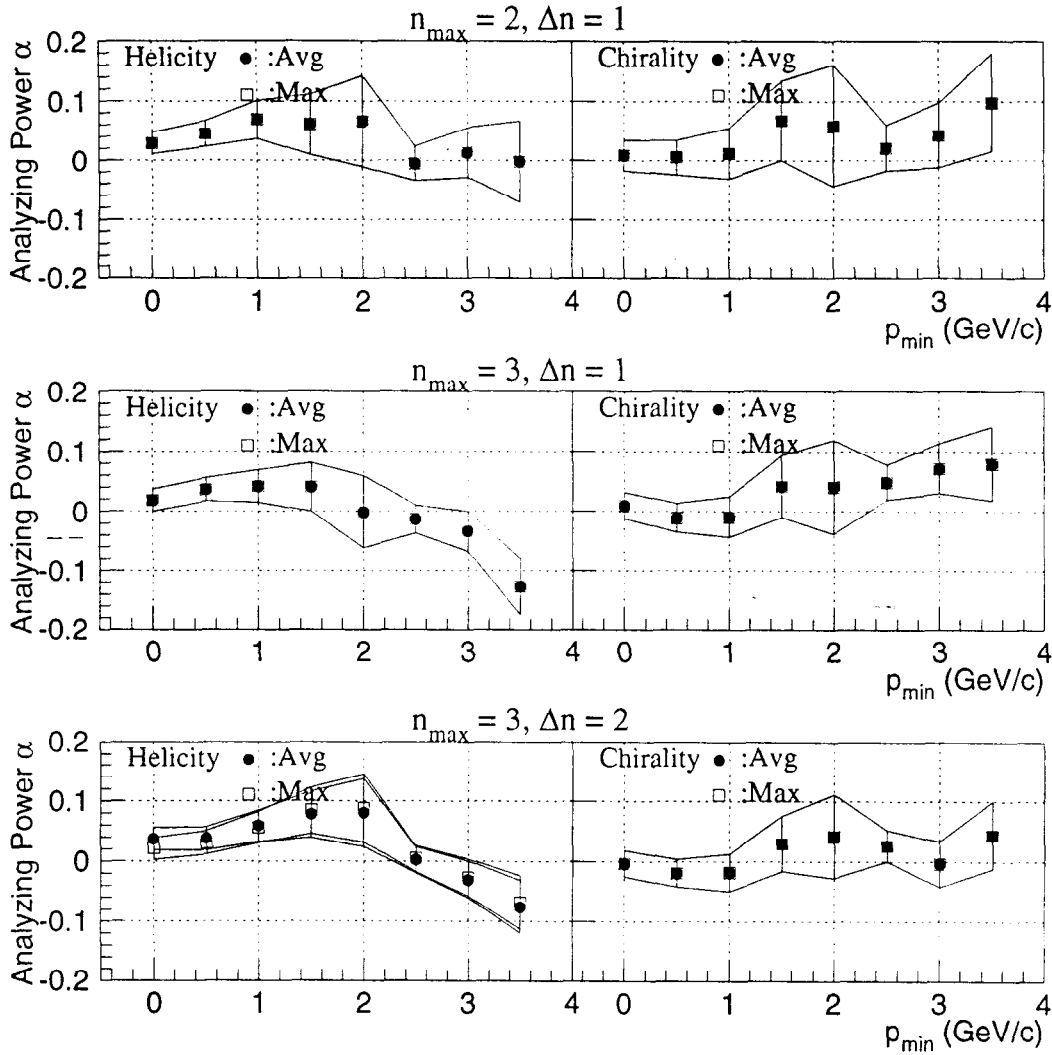
Figure 4.36: Dependence of the analyzing power on p_{min} for combinations of $(n_{max}, \Delta n) = (2, 1)$ (top), $(3, 1)$ (middle) and $(3, 2)$ (bottom) for the heavy flavor sample. The left and right figures show the analyzing power for the helicity- and chirality-based analyses, respectively. Shown are the average (points) and maximum (open squares) methods. For $p_{min} \geq 2.5$ GeV/c, the analyzing powers are shown multiplied by $1/4$, because the analyzing powers in the high p_{min} region have quite large values and errors compared to those in the low p_{min} region.

4.8 Systematic Errors

If all particles produced in an event are detected with precise measurements of their energies and momenta and an ideal analysis can be performed, any physical results coming from such data would not contain any uncertainties except for statistical fluctuation. Such an ideal detector, however, does not exist. The acceptance and resolutions of energy and momentum measurements are limited for any real detectors. Therefore, it is necessary to estimate the correction or systematic error from these limitations to obtain the correct results or the reliability of the results.

The results presented in the preceding sections might be also affected by the event selection with limited detector acceptance and momentum resolution, etc. Therefore, exactly the same analysis as in the preceding three sections were performed to estimate the systematic errors from the following three sources.

1. **Track and event selection**, where by applying several sets of the track and event selection criteria, the variation of the results is calculated in order to estimate the systematic errors due to the selection.

2. **Jet finding**, where the systematic errors due to jet finding algorithm and y_{cut} value are estimated, and

3. **Analysis**, where by using the fact that jet handedness should be zero for the events generated by the Monte Carlo simulation, the bias due to analysis method is estimated.

The analyzing power was calculated with the criteria which were aimed for the systematic study of each error source. The systematic error from each source was defined as the difference between this analyzing power and the analyzing power obtained under the standard criteria. The statistical fluctuation was removed from the difference. The total systematic error is calculated as the quadratic sum of the errors from those sources. A detailed description of the study of the systematic errors is given in Appendix C. Since magnitude of the systematic error could be changed for each particle selection methods, the error was estimated for each method.

Three Leading Particle Selection Method The systematic errors of the analyzing power from the three sources shown above are summarized in Table 4.6.

Most of the systematic errors are negligible or quite small. This means that the analysis method gives unbiased analyzing powers.

Source	Method	Systematic error		
		Global	Light	Heavy
Track and event selection	Helicity	~ 0	~ 0	~ 0
	Modified Helicity	~ 0	~ 0	~ 0
	Chirality	~ 0	~ 0	~ 0
Jet finding	Helicity	~ 0	~ 0	~ 0
	Modified Helicity	~ 0	~ 0	~ 0
	Chirality	~ 0	~ 0	~ 0
Analysis	Helicity	~ 0	~ 0	$+0.001$
	Modified Helicity	~ 0	~ 0	~ 0
	Chirality	-0.003	~ 0	~ 0
Total	Helicity	~ 0	~ 0	$^{+0.001}_{-0.000}$
	Modified Helicity	~ 0	~ 0	~ 0
	Chirality	$^{+0.000}_{-0.003}$	~ 0	~ 0

Table 4.6: The systematic errors for the 3-particle selection method. The total systematic error is the quadratic sum of the errors from all sources.

N **Leading Particle Selection Method**   The dependence of the systematic error on the analyzing power on the number of leading particles N_{lead} is shown in Figure 4.37. The statistical errors are also shown in the figure for comparison. The systematic error was calculated as a quadratic sum of the errors from all the sources. In general, the systematic error becomes large in the large N_{lead} region. The systematic error is smaller than the statistical error in almost the whole region.

Particle Selection Method based on Rapidity and Momentum   The dependence of the systematic error on the analyzing power on p_{min} for several combinations of $(n_{max}, \Delta n)$ is shown in Figure 4.38, 4.39 and 4.40 for the global, light and heavy flavor samples, respectively. The statistical errors are also shown in the figures for comparison.

The systematic error was calculated as the quadratic sum of the errors from all the sources. The systematic error generally becomes large in the high p_{min} region. The systematic error is smaller than the statistical error except in the high p_{min} region.
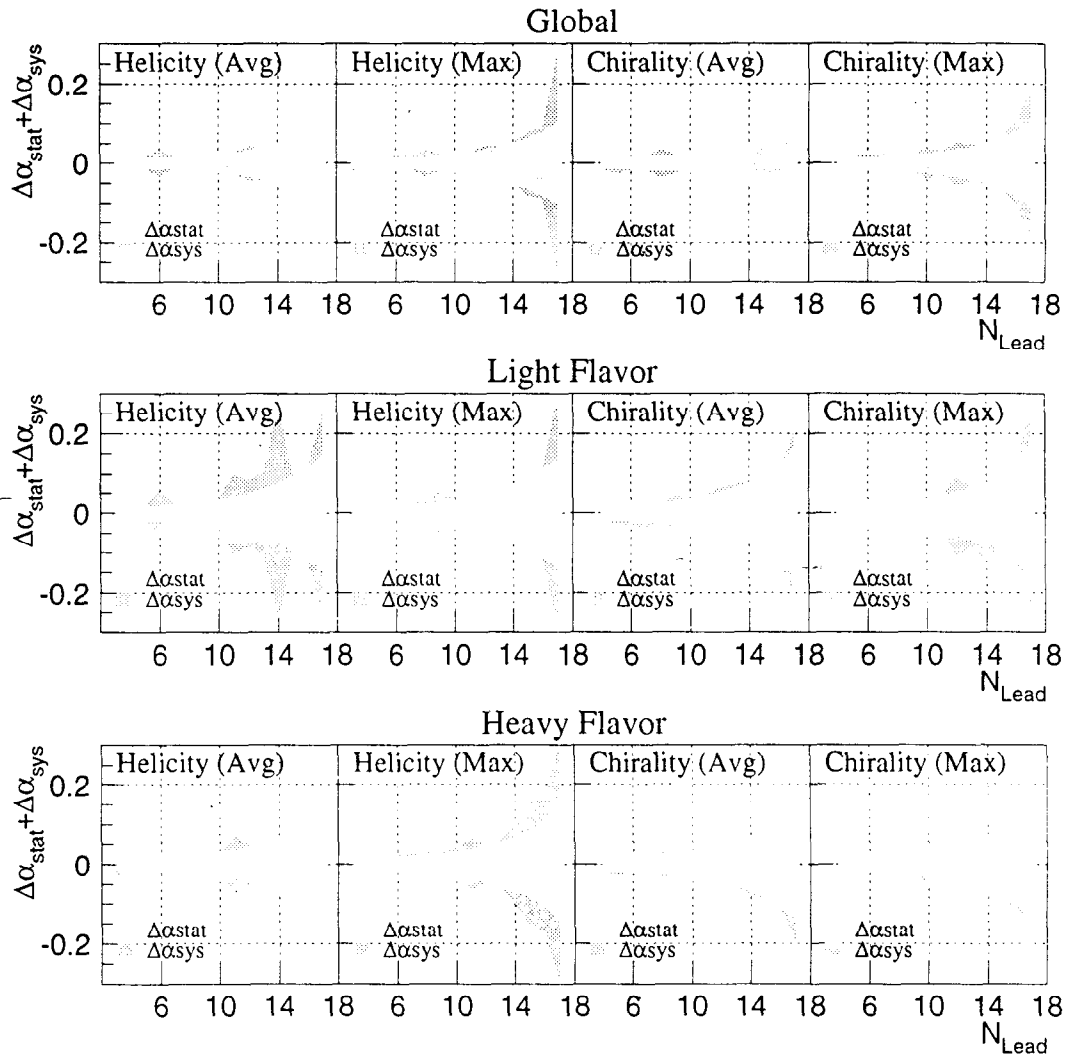
Figure 4.37: Dependence of the statistical errors and systematic errors on the analyzing power on N_{lead} in the global, light and heavy flavor samples. The light and dark hatched areas are shown the statistical and systematic errors, respectively.
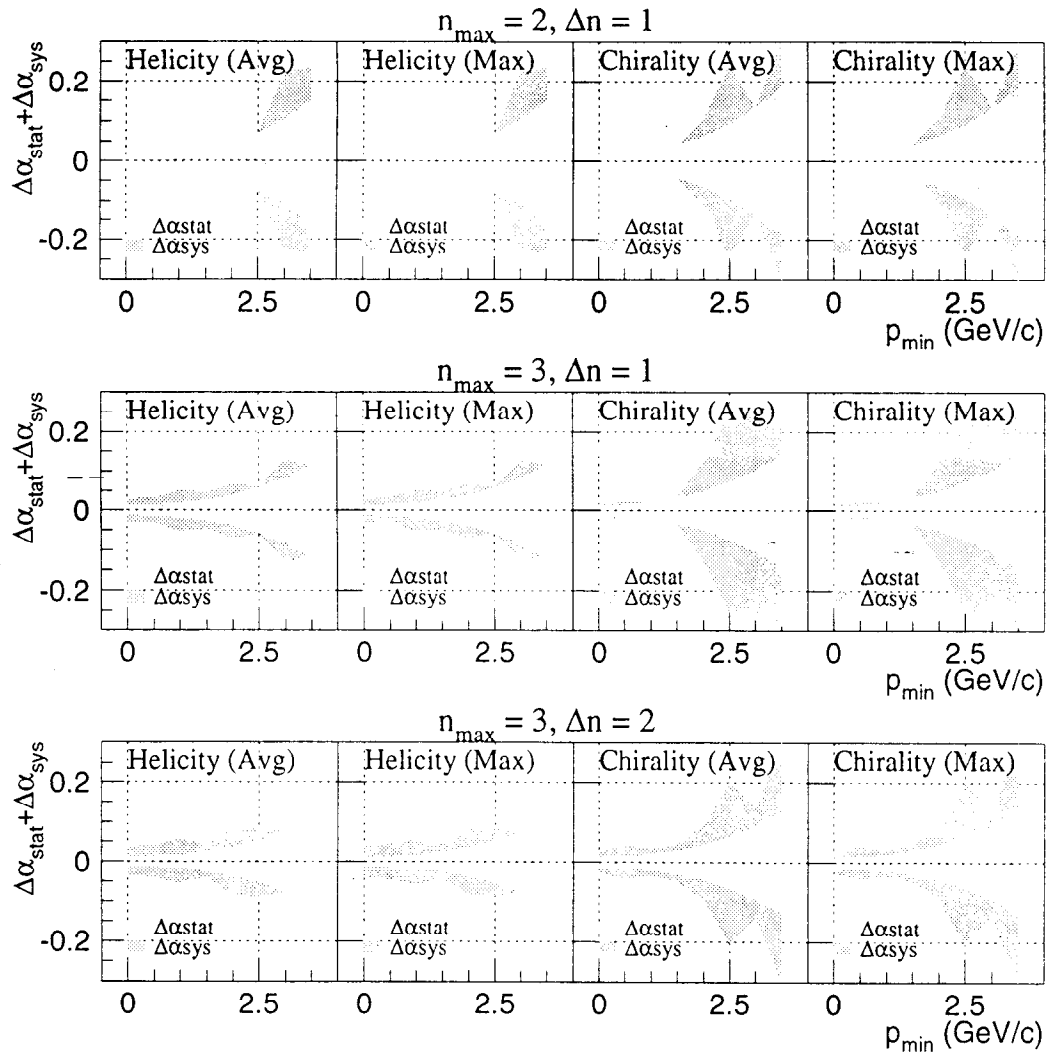
Figure 4.38: Dependence of the systematic and statistical errors on the analyzing power on p_{min} for combinations of $(n_{max}, \Delta n) = (2, 1)$ (top), $(3, 1)$ (middle) and $(3, 2)$ (bottom) for the global sample. The light and dark hatched areas are the statistical and systematic errors, respectively.
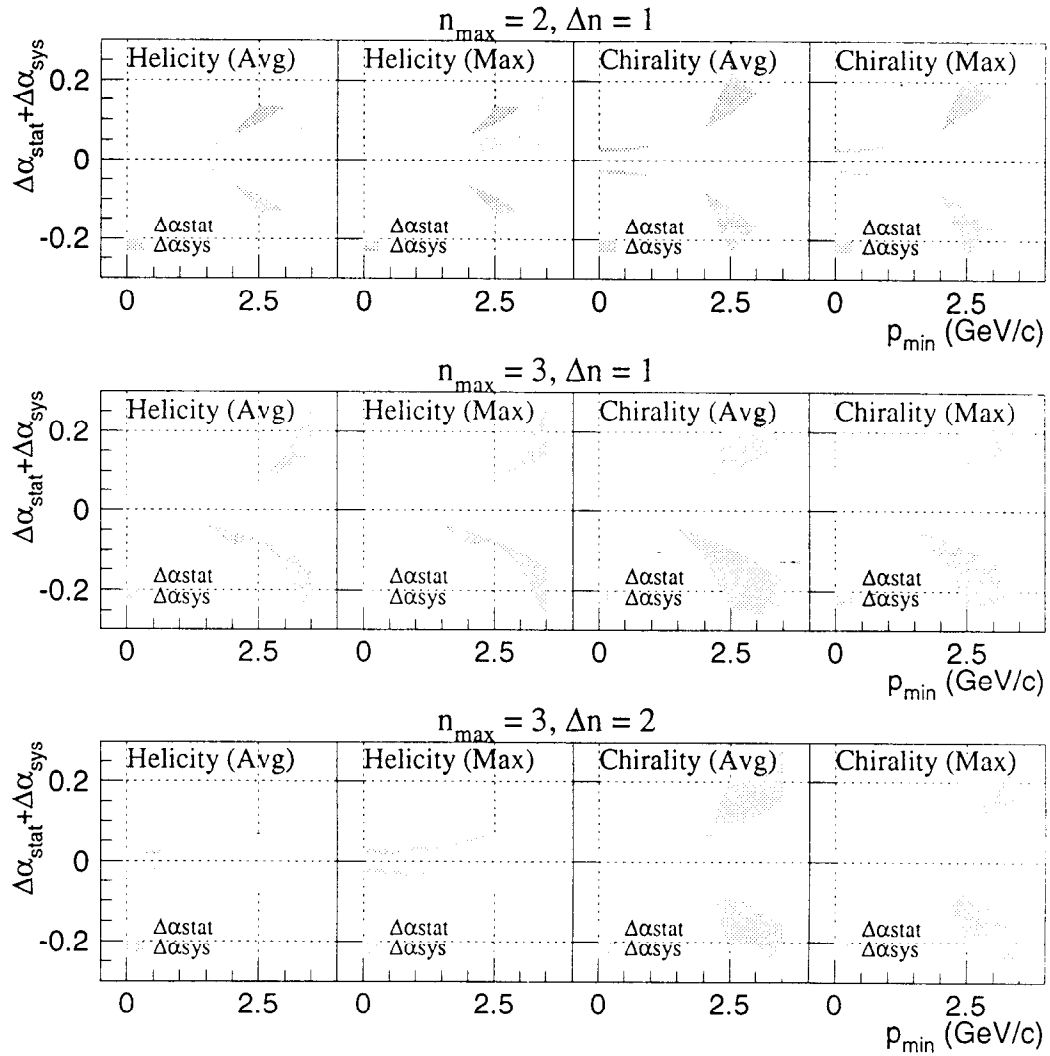
Figure 4.39: Dependence on the systematic and statistical errors of the analyzing power on p_{min} for combinations of $(n_{max}, \Delta n) = (2, 1)$ (top), $(3, 1)$ (middle) and $(3, 2)$ (bottom) for the light flavor sample. The light and dark hatched areas are the statistical and systematic errors, respectively.
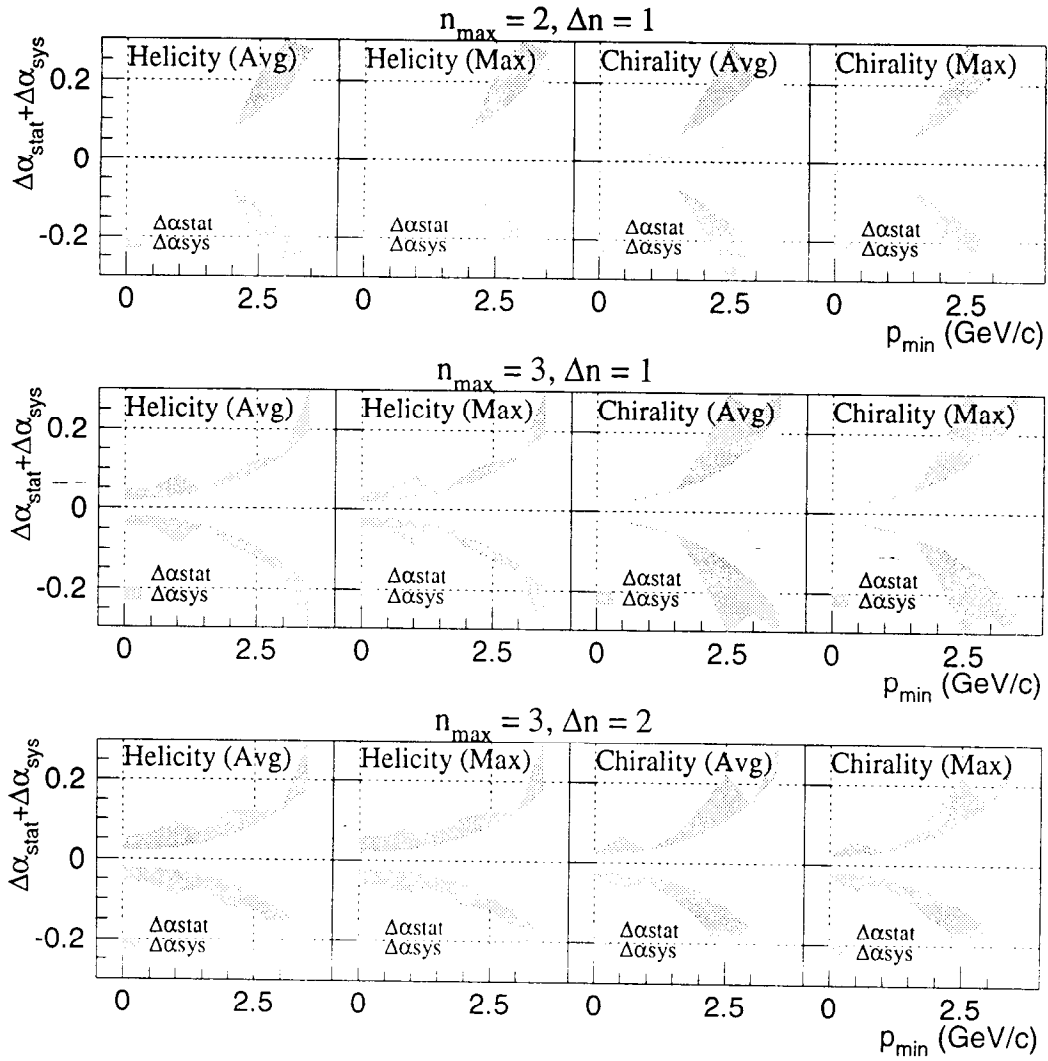
Figure 4.40: Dependence of the systematic and statistical errors on the analyzing power on p_{min} for combinations of $(n_{max}, \Delta n) = (2, 1)$ (top), (3, 1) (middle) and (3, 2) (bottom) for the heavy flavor sample. The light and dark hatched areas are the statistical and systematic errors, respectively.

Chapter 5

Summary and Conclusion

5.1 Summary

Three Leading Particle Selection Method

The analyzing powers for the global, light flavor and heavy flavor samples are summarized in Table 5.1. The analyzing powers obtained by this particle selec-

Analysis	Analyzing Power		
	Global	Light flavor	Heavy flavor
Helicity	$-0.029 \pm 0.024 \pm 0.000$	$-0.057 \pm 0.031 \pm 0.000$	$0.007 \pm 0.036^{+0.001}_{-0.000}$
Mod. Helicity	$0.055 \pm 0.024 \pm 0.000$	$0.056 \pm 0.031 \pm 0.000$	$0.055 \pm 0.036 \pm 0.000$
Chirality	$-0.001 \pm 0.026^{+0.000}_{-0.003}$	$0.052 \pm 0.038 \pm 0.000$	$-0.058 \pm 0.035 \pm 0.000$

Table 5.1: Analyzing powers for the helicity-, modified helicity- and chirality-based analyses. The first numbers are the central values of the analyzing power. The second and third numbers are the statistical and systematic errors, respectively.

tion method are consistent with zero within 2σ except that the analyzing power on the basis of the modified helicity-based analysis for the global sample is 2.3σ away from zero. The modified helicity-based handedness seems to have angular and beam polarization dependence. However, we can not conclude that the dependence is significant, because statistics is still poor. This method does not give systematic bias to the results, therefore, we will obtain more precise results with large statistics.

Since the analyzing powers are small, we set upper limits at 95% confidence level on the analyzing powers as follows. First, the total error $\Delta\alpha_{tot}$ was assumed as the quadratic sum of the statistical and systematic errors. Then, we find u and l to

satisfy the following equations:

$$0.95 = \frac{1}{\sqrt{2\pi}\Delta\alpha_{tot}} \int_{-\infty}^{u} \exp\left\{-\frac{(x-\alpha)^2}{2\Delta\alpha_{tot}^2}\right\} dx,$$

$$0.95 = \frac{1}{\sqrt{2\pi}\Delta\alpha_{tot}} \int_{l}^{\infty} \exp\left\{-\frac{(x-\alpha)^2}{2\Delta\alpha_{tot}^2}\right\} dx,$$

for the upper and lower limits at 95% confidence level. The upper limit on the magnitude of the analyzing power was defined as the largest in magnitude of u and l, *i.e.* $\max(|u|, |l|)$. The upper limits on the analyzing powers calculated in this way are given in Table 5.2.

Analysis	Upper limit on Analyzing Power		
	Global	Light flavor	Heavy flavor
Helicity	0.069	0.108	0.075
Modified Helicity	0.094	0.108	0.115
Chirality	0.052	0.125	0.115

Table 5.2: Upper limits at 95 % confidence level on the magnitude of the analyzing powers for the helicity-, modified helicity- and and chirality-based analyses.

N Leading Particle Selection Method

Fig 5.1 shows the analyzing powers as a function of N_{lead}. No dependence of the analyzing power was found from this figure, and the analyzing power is consistent with zero for all N_{lead} values within 2σ of its error. We also set the upper limits at 95% confidence level on the analyzing powers by using the same calculation given in the previous section. The upper limits on the magnitude of the analyzing powers are shown in Fig 5.2 as a function of N_{lead}. For $N_{lead} \leq 10$, the upper limits are in the range 0.05-0.10. For a larger N_{lead} region, the upper limits increase due to the reduction in data statistics.

Particle Selection Method Based on Rapidity and Momentum

The analyzing powers are shown in Fig 5.3, Fig 5.4 and Fig 5.5 for the global, light flavor and heavy flavor samples as a function of p_{min}, respectively. The results are plotted for combinations of $(n_{max}, \Delta n) = (2, 1), (3, 1)$ and $(3, 2)$ separately. For the helicity-based method with $n_{max} = 3$, the analyzing power becomes negative as P_{min}
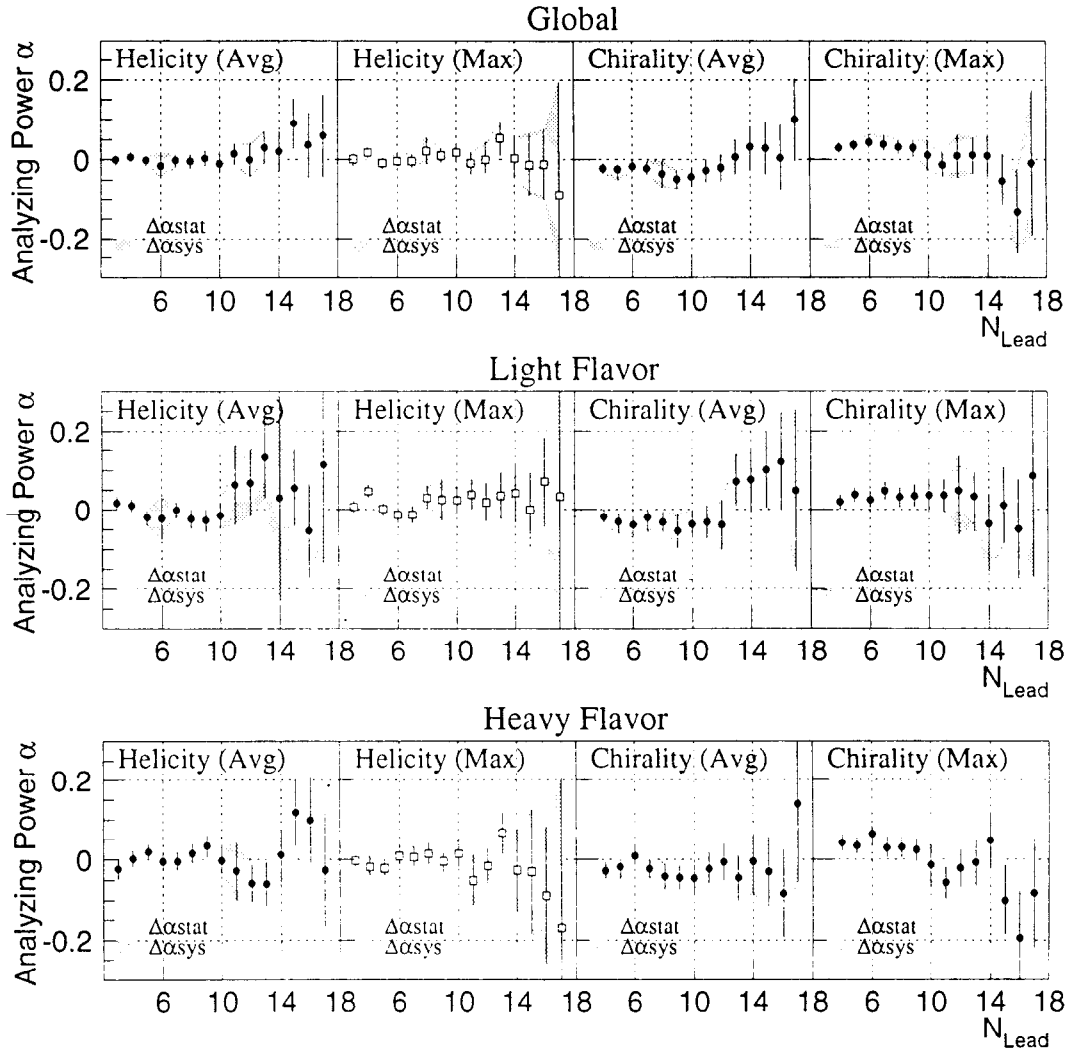
Figure 5.1: The analyzing power as a function of N_{Lead} for the global (top), light (middle) and heavy flavor sample (bottom). The two left and two right figures show the analyzing power by the helicity- and chirality-based analyses, respectively. Shown are average method (points) and maximum method (open squares). The light and dark hatched regions show statistical and systematic errors, respectively. For every analyzing power, the statistical error is dominant.
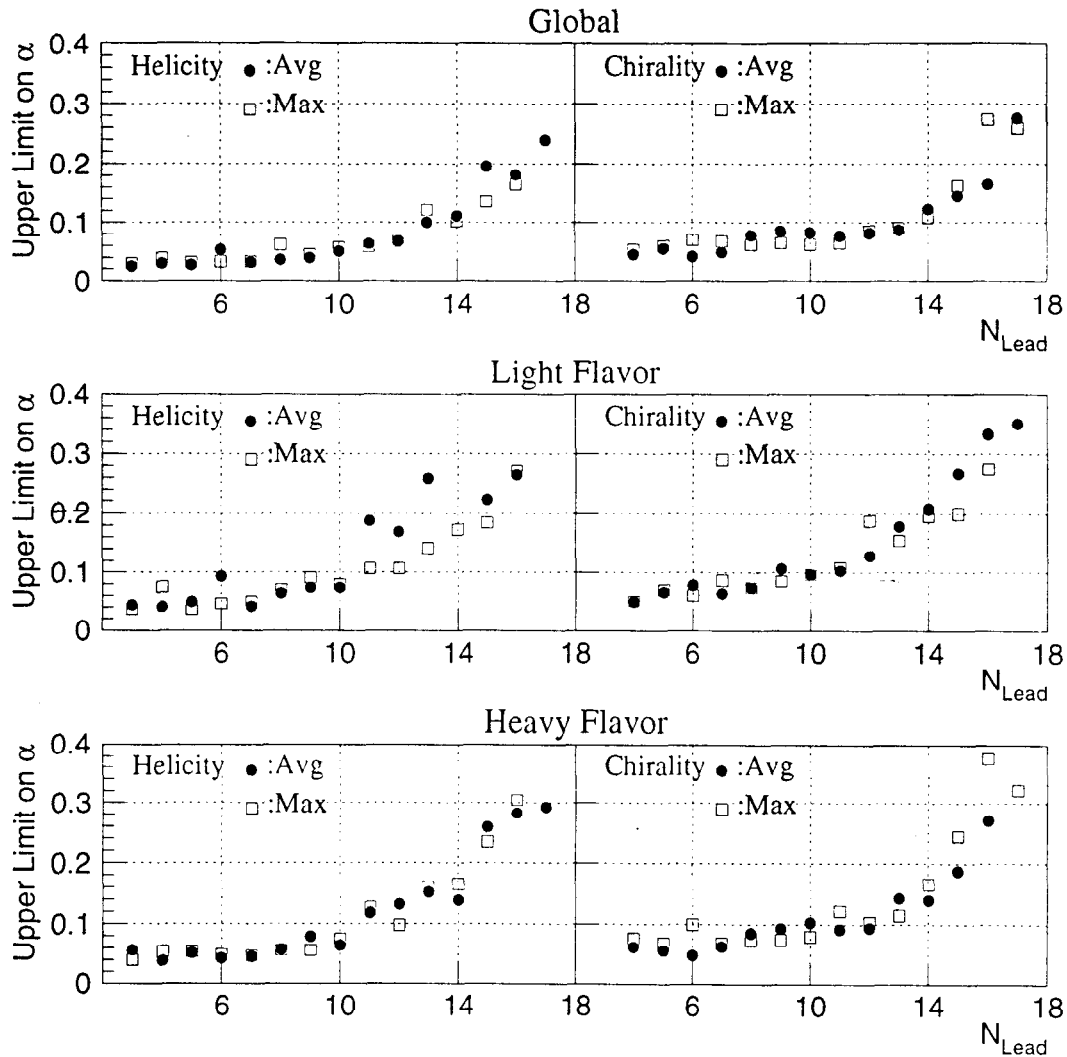
Figure 5.2: Upper limits at 95 % confidence level on the magnitude of the analyzing power for the global (top), light (middle) and heavy flavor samples (bottom). The left and right figures show the upper limit for the helicity- and chirality-based analyses, respectively. Shown are the average (points) and maximum (open squares).

increases, on the contrary, it tends to have positive value for the chirality method. However, all analyzing powers are consistent with zero within 2σ. We set upper limits at 95% confidence level on the analyzing powers for this particle selection method. The upper limits on analyzing powers are shown in Fig 5.6, Fig 5.7 and Fig 5.8 for the global, light flavor and heavy flavor samples, respectively, as a function of p_{min} for the combinations of Δn and n_{max} values, separately. This particle selection method gave the upper limits of analyzing powers of less than 0.10 for $n_{max} \leq 3$, $\Delta n \leq 2$ and $p_{min} < 1.5$ GeV/c, but the larger upper limits for $p_{min} > 1.5$ GeV/c.

Figure 5.3: The analyzing power as a function of p_{min} for combinations of $(n_{max}, \Delta n) = (2, 1)$ (top), (3, 1) (middle) and (3, 2) (bottom) for the global sample. The two left and two right figures show the analyzing power by the helicity- and chirality-based analyses, respectively. Shown are the average (points) and maximum method (open squares). The light and dark hatched regions show statistical and systematic errors, respectively. For $p_{min} \geq 2.5$ GeV/c, the analyzing powers are shown multiplied by 1/4, because the analyzing powers in the high p_{min} region have quite large values and errors compared to those in the low p_{min} region. For every analyzing power, statistical error is dominant.
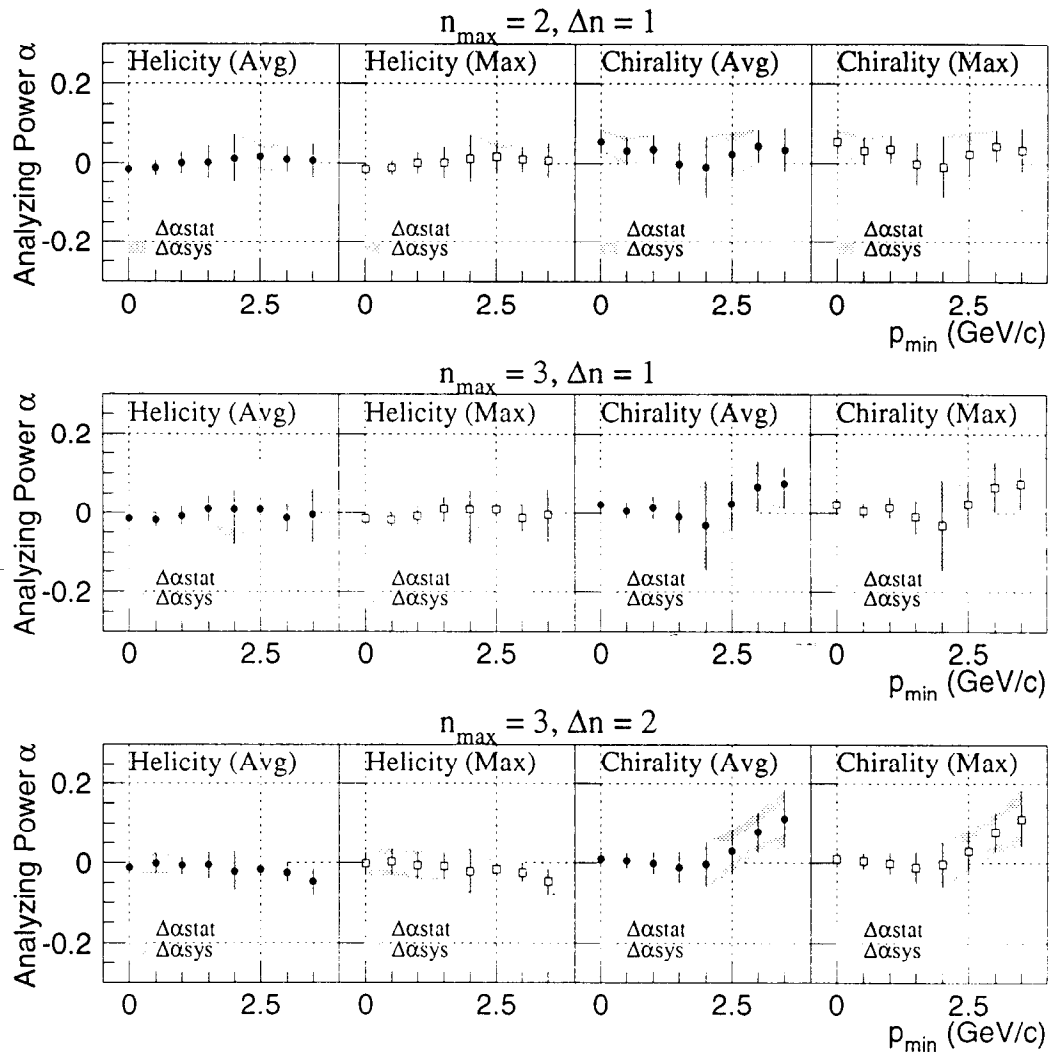
Figure 5.4: The analyzing power as a function of p_{min} for combinations of $(n_{max}, \Delta n) = (2, 1)$ (top), (3, 1) (middle) and (3, 2) (bottom) for the light flavor sample. The two left and two right figures show the analyzing power by the helicity- and chirality-based analyses, respectively. Shown are the average (points) and maximum method (open squares). The light and dark hatched regions show statistical and systematic errors, respectively. For $p_{min} \geq 2.5$ GeV/c, the analyzing powers are shown multiplied by 1/4, because the analyzing powers in the high p_{min} region have quite large values and errors compared to those in the low p_{min} region. For every analyzing power, the statistical error is dominant.
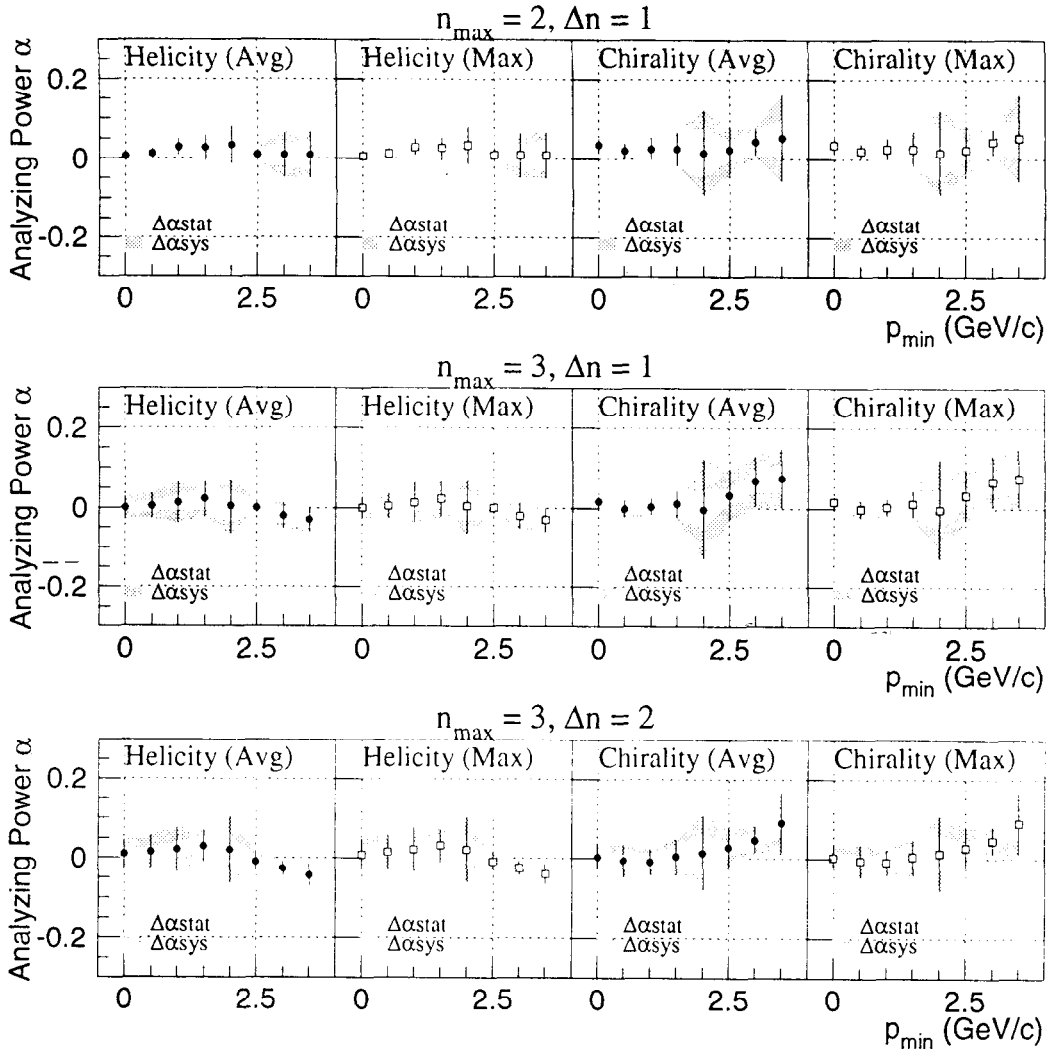
Figure 5.5: The analyzing power as a function of p_{min} for combinations of $(n_{max}, \Delta n) = (2, 1)$ (top), (3, 1) (middle) and (3, 2) (bottom) for the heavy flavor sample. The two left and two right figures show the analyzing power by the helicity- and chirality-based analyses, respectively. Shown are the average (points) and maximum method (open squares). The light and dark hatched regions show statistical and systematic errors, respectively. For $p_{min} \geq 2.5$ GeV/c, the analyzing powers are shown multiplied by 1/4, because the analyzing powers in the high p_{min} region have quite large values and errors compared to those in the low p_{min} region. For every analyzing power, the statistical error is dominant.

Figure 5.6: Dependence of the upper limits at 95% confidence level on magnitude of the analyzing power on p_{min} for combinations of $(n_{max}, \Delta n) = (2, 1)$ (top), $(3, 1)$ (middle) and $(3, 2)$ (bottom) for the global sample. The left and right figures show the analyzing power for the helicity- and chirality-based analyses, respectively. Shown are the average (points) and maximum method (open squares). For $p_{min} \geq 2.5$ GeV/c, the upper upper limits are shown multiplied by 1/4, because the upper limits in the high p_{min} region are quite large compared to those in the low p_{min} region.
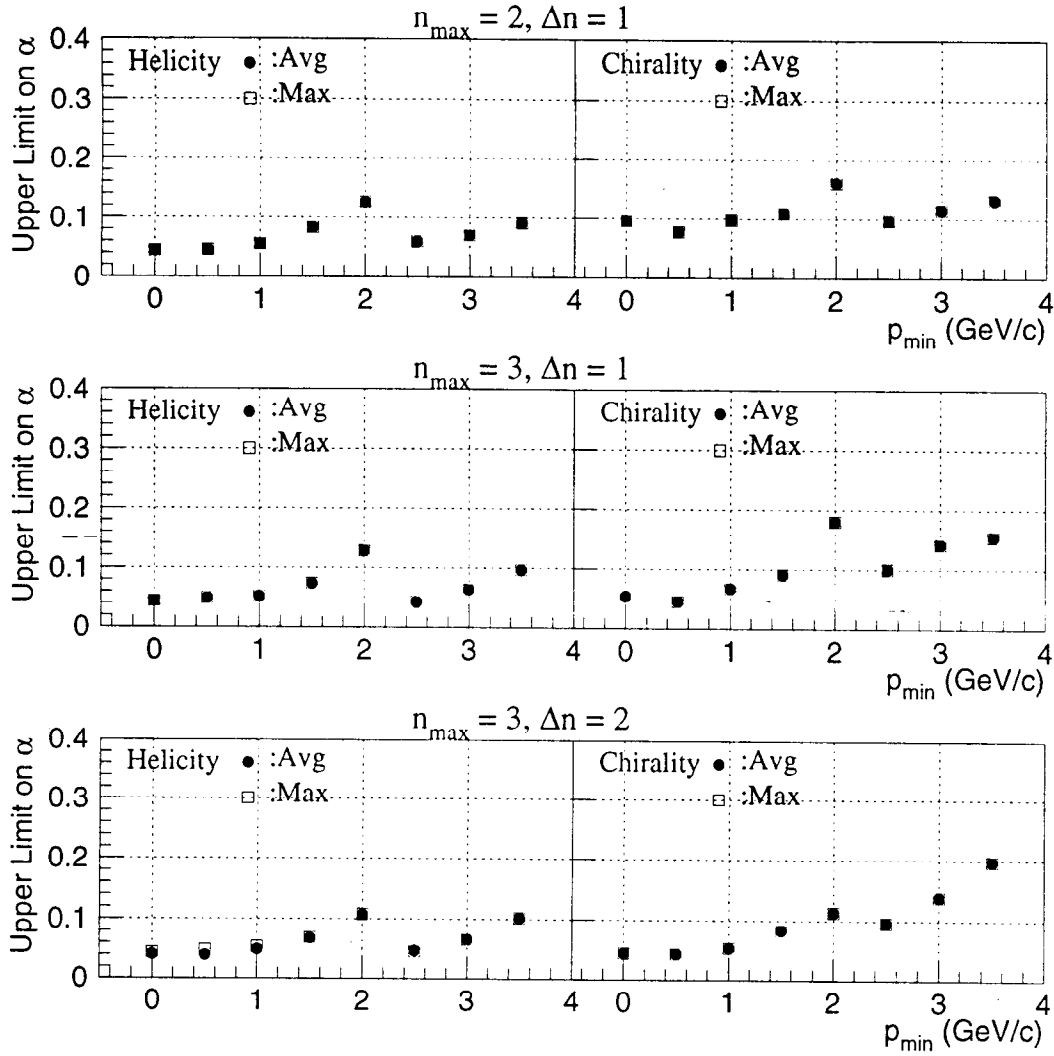
Figure 5.7: Dependence of upper limits at 95% confidence level on magnitude of the analyzing power on p_{min} for combinations of $(n_{max}, \Delta n) = (2, 1)$ (top), (3, 1) (middle) and (3, 2) (bottom) for the light flavor sample. The left and right figures show the analyzing power for the helicity- and chirality-based analyses, respectively. Shown are the average (points) and maximum method (open squares). For $p_{min} \geq 2.5$ GeV/c, the upper upper limits multiplied are shown by 1/4, because the upper limits in the high p_{min} region are quite large compared to those in the low p_{min} region.
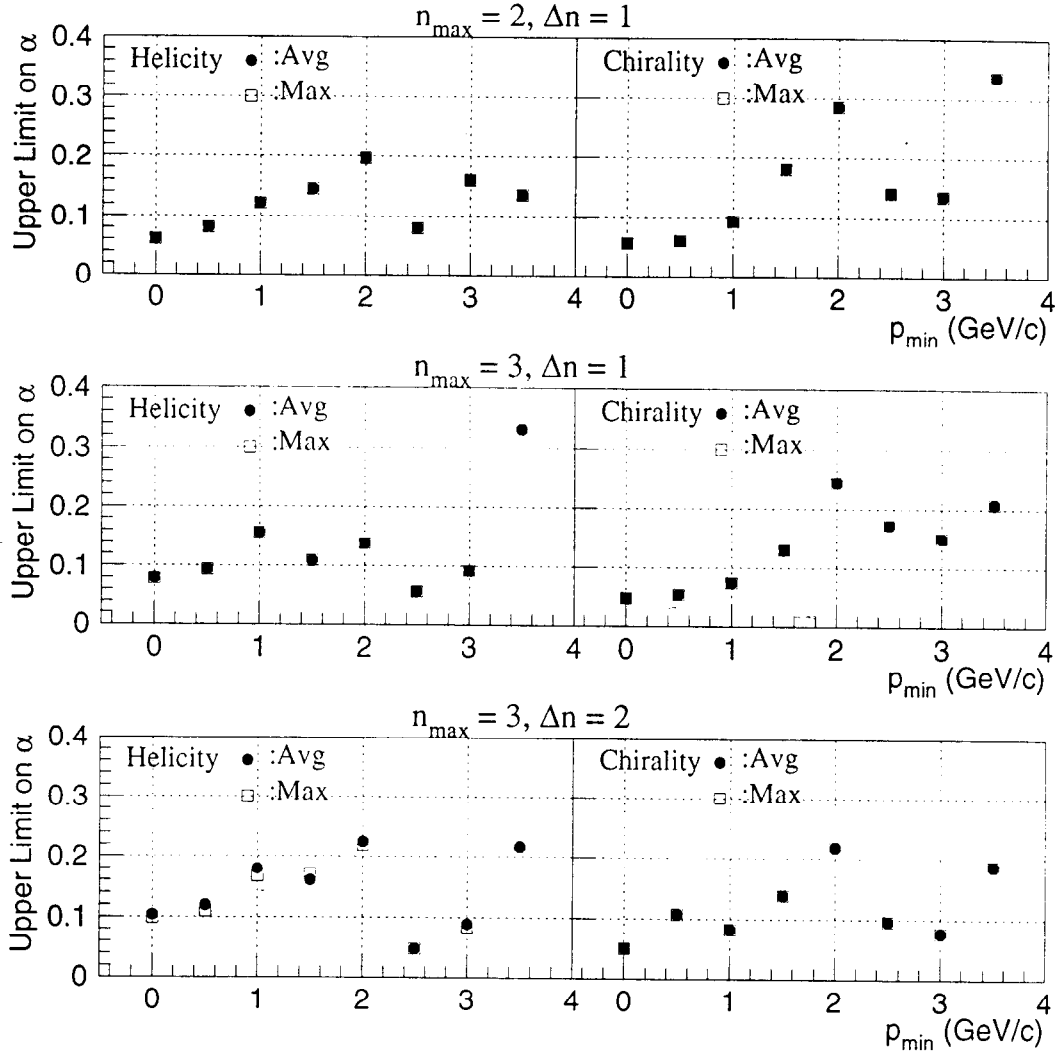
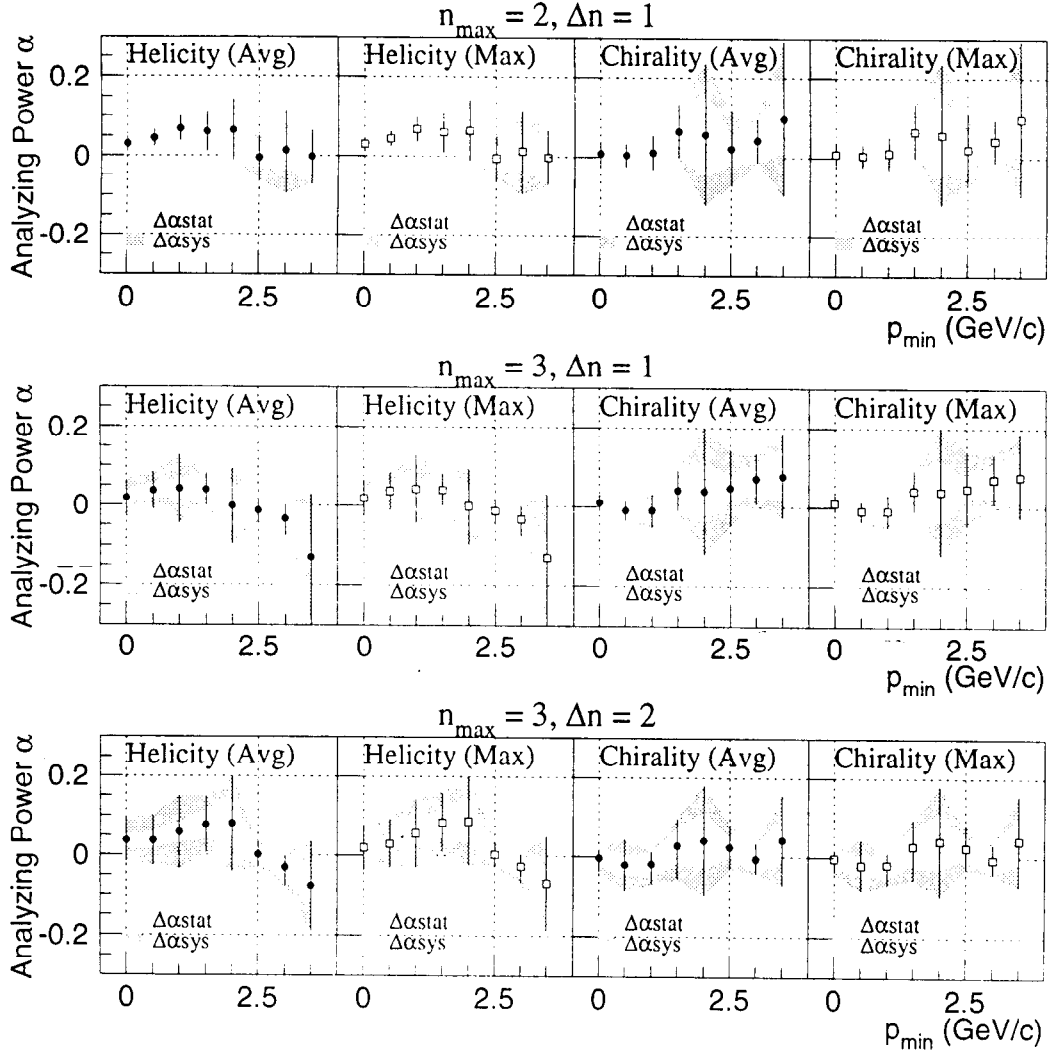Figure 5.8: Dependence of upper limit at 95% confidence level on magnitude of the analyzing power on p_{min} for combinations of $(n_{max}, \Delta n) = (2, 1)$ (top), $(3, 1)$ (middle) and $(3, 2)$ (bottom) for the heavy flavor sample. The left and right figures show the analyzing power for the helicity- and chirality-based analyses, respectively. Shown are the average (points) and maximum method (open squares). For $p_{min} \geq 2.5$ GeV/c, the upper upper limits are shown multiplied by 1/4, because the upper limits in the high p_{min} region are quite large compared to those in the low p_{min} region.

5.2 Conclusion.

We have searched for jet handedness in hadronic decays of Z^0 bosons produced by the SLC and detected by the SLD, where quark and antiquark from Z^0 decays were highly longitudinally polarized. This high polarization of partons may potentially give a large signal of jet handedness. Defining jet handedness as an asymmetry in the observable Ω which was taken for each jet as a triple vector product of two particles and the jet axis, we calculated the analyzing power for three particle selection methods with two different (helicity and chirality) Ω definitions. However, none of them showed a significant signal of jet handedness, giving analyzing powers consistent with zero. The upper limits on the magnitude of the analyzing power for these methods are about 0.2 or less.

The error on jet handedness is still dominated by the statistics of the data sample. If the statistical error becomes small, the systematic error becomes dominant. Therefore, if the data statistics increases by a factor of four, we may be able to find a signal of jet handedness at the few % level in jets in Z^0 decays.

Another way to get a large analyzing power may be to make a new definition of Ω. In this sense, more new theoretical studies for jet handedness may help us to define Ω and to find a significant signal of handedness. Such theoretical study is useful to understand the transport of the parton polarization in jets and what happens during the hadronization process.

Appendix A

Polarization for Analyses

This study assumed the simplest model of decay of a parton. A parton decays into two particles which carry information of helicity of the parton. This model gives the relations between Ωs of quarks and antiquarks. These relations for each of the helicity- and chirality-based analyses give the polarization for each analysis.

Helicity-based analysis

A quark in $e^+e^- \to q\bar{q}$ decays into two particles with momenta $\vec{k}_1, \vec{k}_2$ as shown in Figure A.1 (a). Ω_{hel} is defined as:

$$\Omega_{hel} = \hat{t} \cdot (\vec{k}_1 \times \vec{k}_2), \qquad (A.1)$$

where $\hat{t}$ is a unit vector of a parton momentum. The charge conjugate (C), parity (P) operations make this decay changed to the states (b) and (c) shown in Figure A.1, respectively. Two successive operation CP makes the state (a) changed to the state (d). These four states give the the relations:

$$\begin{aligned}
\Omega_{hel}(\bar{q}_R) &= +\Omega_{hel}(q_R) \\
\Omega_{hel}(q_L) &= -\Omega_{hel}(q_R) \\
\Omega_{hel}(\bar{q}_L) &= -\Omega_{hel}(q_R) \qquad (A.2)
\end{aligned}$$

Therefore, Ω_{hel} depends on only helicity of a parton, the 'helicity-based' polarization $\mathcal{P}_{hel}$ is given by:

$$\mathcal{P}_{hel} \equiv \frac{\displaystyle\sum_{\substack{p=f,\bar{f} \\ h=R,L}} \text{sign}\left\{\Omega_{hel}(f_R)\Omega_{hel}(p_h)\right\} \sigma_h^p}{\displaystyle\sum_{\substack{p=f,\bar{f} \\ h=R,L}} \sigma_h^p}$$
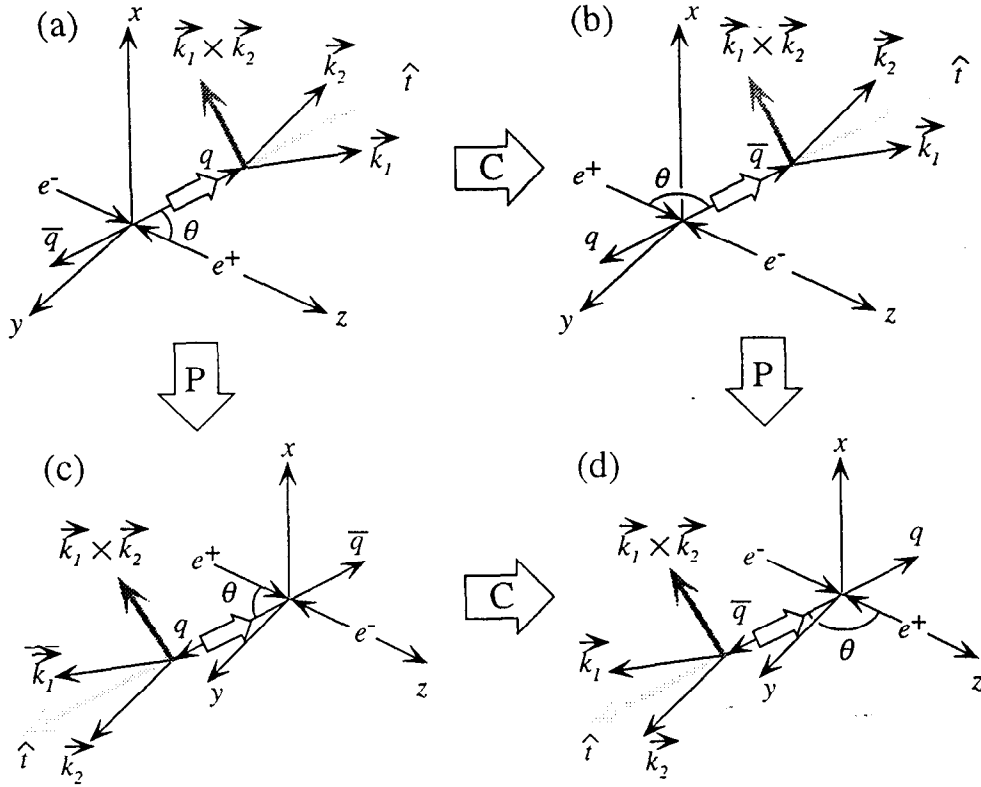
Figure A.1: Decays of partons in the helicity-based analysis.

$$= \frac{\sigma_R^f + \sigma_R^{\bar{f}} - \sigma_L^f - \sigma_L^{\bar{f}}}{\sigma_R^f + \sigma_R^{\bar{f}} + \sigma_L^f + \sigma_L^{\bar{f}}} \tag{A.3}$$

Chirality-based analysis

A quark in $e^+ e^- \rightarrow q\bar{q}$ decays into two positive and negative charged particles with momenta $\vec{k_+}$ and $\vec{k_-}$, respectively, as shown in Figure A.2 (a). Ω_{chi} is defined as:

$$\Omega_{chi} = \hat{t} \cdot (\vec{k_+} \times \vec{k_-}). \tag{A.4}$$

The C, P and CP operations make the state (a) changed to the states (b), (c) and (d), respectively. These four states give the the relations:

$$\Omega_{chi}(\bar{q}_R) = -\Omega_{chi}(q_R)$$
$$\Omega_{chi}(q_L) = -\Omega_{chi}(q_R)$$
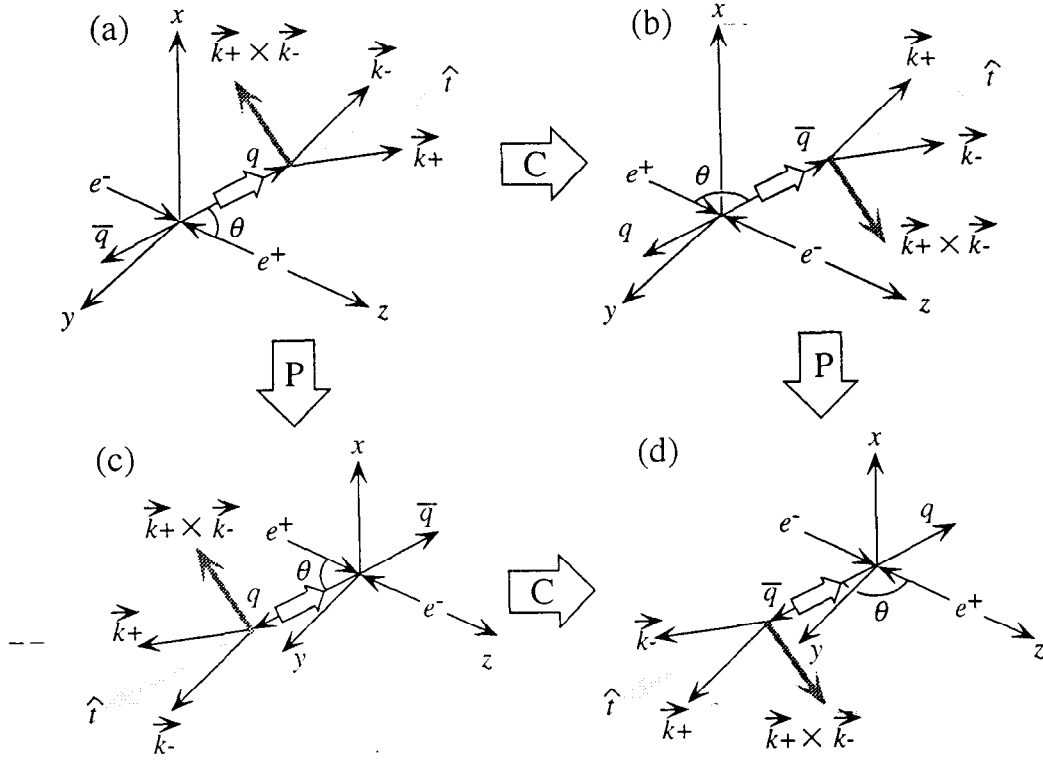
Figure A.2: Decays of partons in the chirality-based analysis.

$$\Omega_{chi}(\bar{q}_L) \;=\; +\Omega_{chi}(q_R) \tag{A.5}$$

Therefore, Ω_{chi} depends on not only helicity but also charge of a parton, the 'chirality-based' polarization for fermion f, $\mathcal{P}_{chi}^{f}$ is given by:

$$
\mathcal{P}_{chi}^{f} \;\equiv\; \frac{\displaystyle\sum_{\substack{p=f,\bar{f}\\h=R,L}} \mathrm{sign}\left\{\Omega_{chi}(f_R)\Omega_{chi}(p_h)\right\}\sigma_h^p}{\displaystyle\sum_{\substack{p=f,\bar{f}\\h=R,L}}\sigma_h^p}
$$

$$
\;=\; \frac{\sigma_R^f - \sigma_R^{\bar{f}} - \sigma_L^f + \sigma_L^{\bar{f}}}{\sigma_R^f + \sigma_R^{\bar{f}} + \sigma_L^f + \sigma_L^{\bar{f}}}. \tag{A.6}
$$

Ω_{chi} depends on particle's charge, therefore, Ω_{chi}s for up-type and down-type quark have opposite sign. If Figure A.2 shows the decay of up-type quark, the decay of down-type quark is obtained by substituting $\vec{k}_{\pm} \rightarrow \vec{k}_{\mp}$. This gives the following

relations:

$$\begin{aligned}
\Omega_{chi}(d_R) &= -\Omega_{chi}(u_R) \\
\Omega_{chi}(d_L) &= +\Omega_{chi}(u_R) \\
\Omega_{chi}(\bar{d}_L) &= -\Omega_{chi}(u_R) \\
\Omega_{chi}(\bar{d}_R) &= +\Omega_{chi}(u_R).
\end{aligned} \tag{A.7}$$

Thus, the chirality-based polarization for a sample is given by:

$$\mathcal{P}_{chi} = \sum_{f=u,d,s,c,b} s_f R_f \mathcal{P}_{chi}^f, \tag{A.8}$$

where s_f is sign of fermion f. R_f is fraction of $f\bar{f}$ events in the sample.

Appendix B

Detailed Helicity-based Analysis

For the 3-prong τ decays, the helicity-based analysis gave small analyzing power which was consistent with zero. In this appendix, the reason for that will be investigated by comparing with the modified helicity-based analysis.

The helicity-based Ω (2.26) is related to the modified helicity-based one (2.27) as follows:

$$\Omega_{hel} = \Omega_{mod.hel} \, \text{sign}(|\vec{k}_3| - |\vec{k}_i|) \tag{B.1}$$

where $\vec{k}_3$ is the momentum of the unlike-sign pion in the 3-charged pion system, i.e., π^+ for a τ^- decay or π^- for a τ^+ decay. $\vec{k}_i$ is the momentum of a pion selected from the two remaining same-charge pions. Squared invariant masses s_1 and s_2 are defined as $(k_1 + k_3)^2$ and $(k_2 + k_3)^2$, respectively. If s_1 is larger(smaller) than s_2, $\vec{k}_{1(2)}$ is used as $\vec{k}_i$. The relation B.1 means that the magnitude of Ω_{hel} is the same as that of $\Omega_{mod.hel}$, but their signs are sometimes different. The difference depends on s_1 and s_2. Therefore, it is useful to investigate the Dalitz plot for the 3-prong decays of τ. Figure B.1 shows the Dalitz plots for the sign-flip triplets with $\Omega_{hel} = -\Omega_{mod.hel}$ and for the no-flip ones with $\Omega_{hel} = \Omega_{mod.hel}$. The two kinds of triplets are well separated in the Dalitz plot.

The helicity-based analyzing power was calculated for τ decaying into sign-flip and no-flip triplets separately in the same way as the 3-leading-particle selection method shown in Section 4.5. Figure B.2 shows jet handedness as a function of $\cos\theta$ and $\mathcal{P}$. τ decaying into the sign-flip and the no-flip triplet has different dependence on $\cos\theta$ and $\mathcal{P}$. Therefore, the analyzing powers for the two kinds of triplets are different. The dependence of jet handedness for the sign-flip and no-flip triplets gives the analyzing powers of -0.141 ± 0.010 and 0.089 ± 0.010, respectively. Due to the opposite contributions from those two triplets, the helicity-based analysis gives small magnitude of the analyzing power. This means that the helicity-based analyzing power depends on the regions in the Dalitz plot which contain selected triplets,
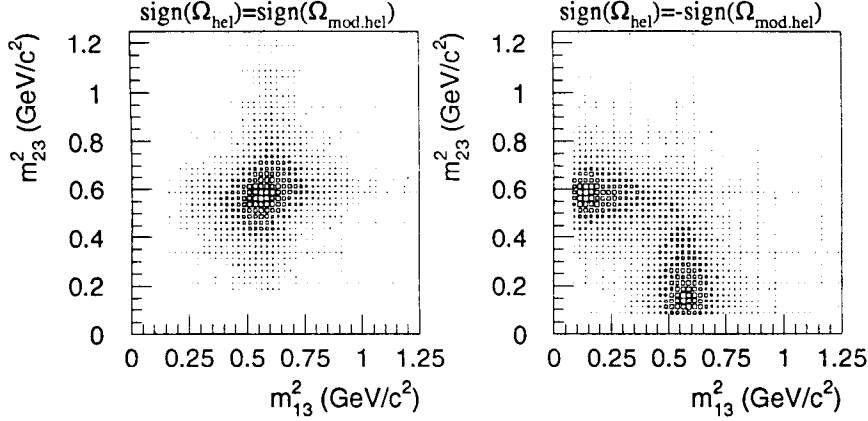
Figure B.1: The Dalitz plots for the sign-flip (right) and no flip (left) triplets. The size of a square if proportional to the entry in each region. The sign-flip and no-flip triplets are well separated.

therefore, the invariant mass cut for the triples is important.

To study such invariant mass cut dependence, the following 6 invariant mass cuts are considered:

Cut A: No cut on invariant masses for 2-pion and 2-pion systems,

Cut B: The cut used in the 3-particle selection method.
i.e. $0.62 < m_{12}, m_{23} < 0.92$ GeV/c^2 AND $0.86 < m_{\pi\pi\pi} < 1.66$ GeV/c^2,

Cut C: $0.62 < m_{12} < 0.92$ GeV/c^2 AND $m_{23} < 0.62$ GeV/c^2 AND $0.86 < m_{\pi\pi\pi} < 1.66$ GeV/c^2
OR
$m_{12} < 0.62$ GeV/c^2 AND $0.62 < m_{23} < 0.92$ GeV/c^2 AND $0.86 < m_{\pi\pi\pi} < 1.66$ GeV/c^2,

Cut D: $0.62 < m_{12} < 0.92$ GeV/c^2 AND 0.62 GeV/c^2 $< m_{23}$ AND $0.86 < m_{\pi\pi\pi} < 1.66$ GeV/c^2
OR
0.62 GeV/c^2 $< m_{12}$ AND $0.62 < m_{23} < 0.92$ GeV/c^2 AND $0.86 < m_{\pi\pi\pi} < 1.66$ GeV/c^2,

Cut E: Cut B AND sign(Ω_{hel}) = sign($\Omega_{mod.hel}$) and

112
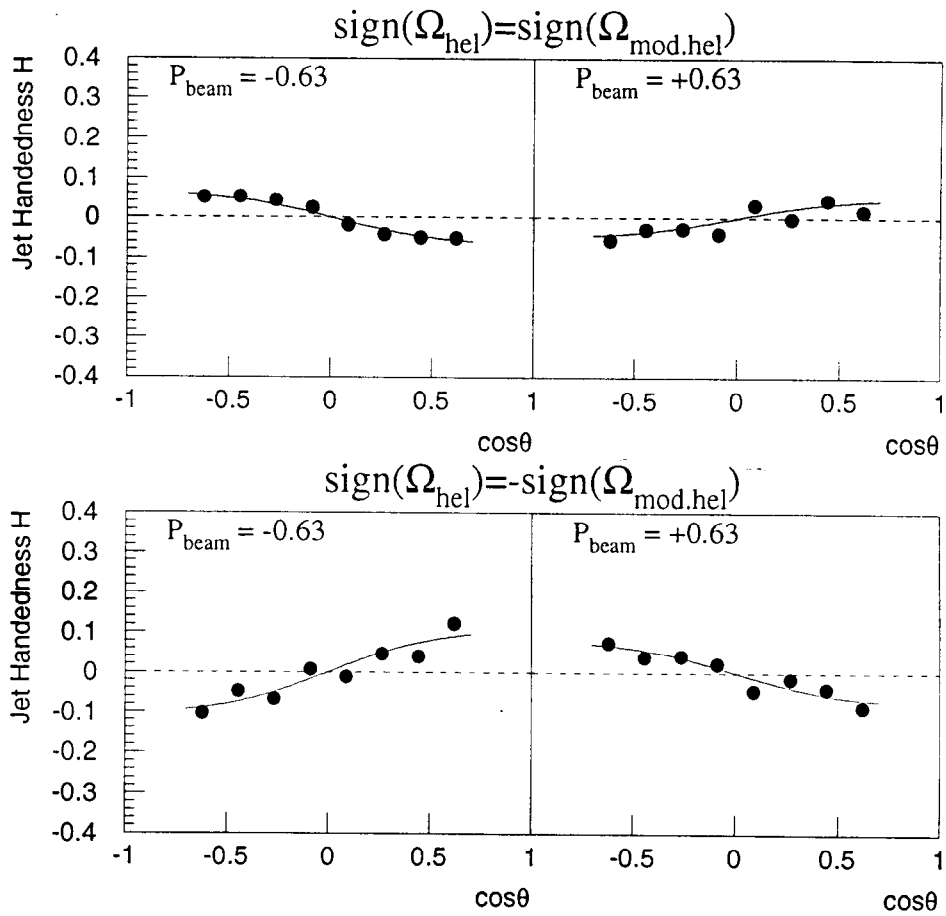
Figure B.2: Dependence of jet handedness on $\cos\theta$ and $\mathcal{P}$ for the sign-flip and no-flip regions.
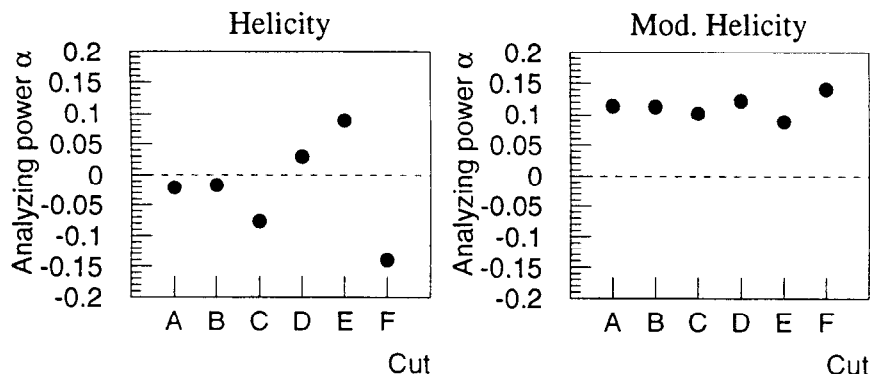
Figure B.3: Dependence of the analyzing power on the invariant mass cuts for 3-prong τ decays generated by the Monte Carlo simulation.

Cut F: Cut B AND $\text{sign}(\Omega_{hel}) = -\text{sign}(\Omega_{mod.hel})$.

Combination of Cut C and Cut D, Cut E and Cut F are identical with Cut B. Cut C and Cut F (Cut D and Cut E) select triplets in similar regions in the Dalitz plot, since sign-flip and no-flip triplets are mainly located in the areas determined by Cut C and Cut D, respectively.

The analyzing power for the helicity-based analysis is calculated with each invariant mass cut. Figure B.3 shows the dependence of the analyzing power on the cuts. Averages of the analyzing powers for Cut C and Cut D, Cut E and Cut F are same as the analyzing power for Cut B. The figure also shows dependence of the modified helicity-based analyzing powers on the invariant mass cuts for comparison. The helicity-based analyzing powers for Cut C and Cut D, Cut E and Cut F have opposite signs and Cut F gives largest analyzing power in magnitude.

The invariant mass cuts were applied for jets in the data and the dependence of the helicity and modified helicity-based analyzing powers on the cuts was investigated. Figure B.4 shows the dependence for the three samples. All of the analyzing powers for the heavy-flavor sample are consistent with zero with in 1.5 σ. On the other hand, some of the analyzing powers for the light-flavor sample, especially with Cut C and Cut F, are away from zero by 2 σ or more. The analyzing powers seems to have positive values for the modified helicity-based analysis. However, since some results are correlated with each other, it is not clear that these non-zero analyzing powers

114
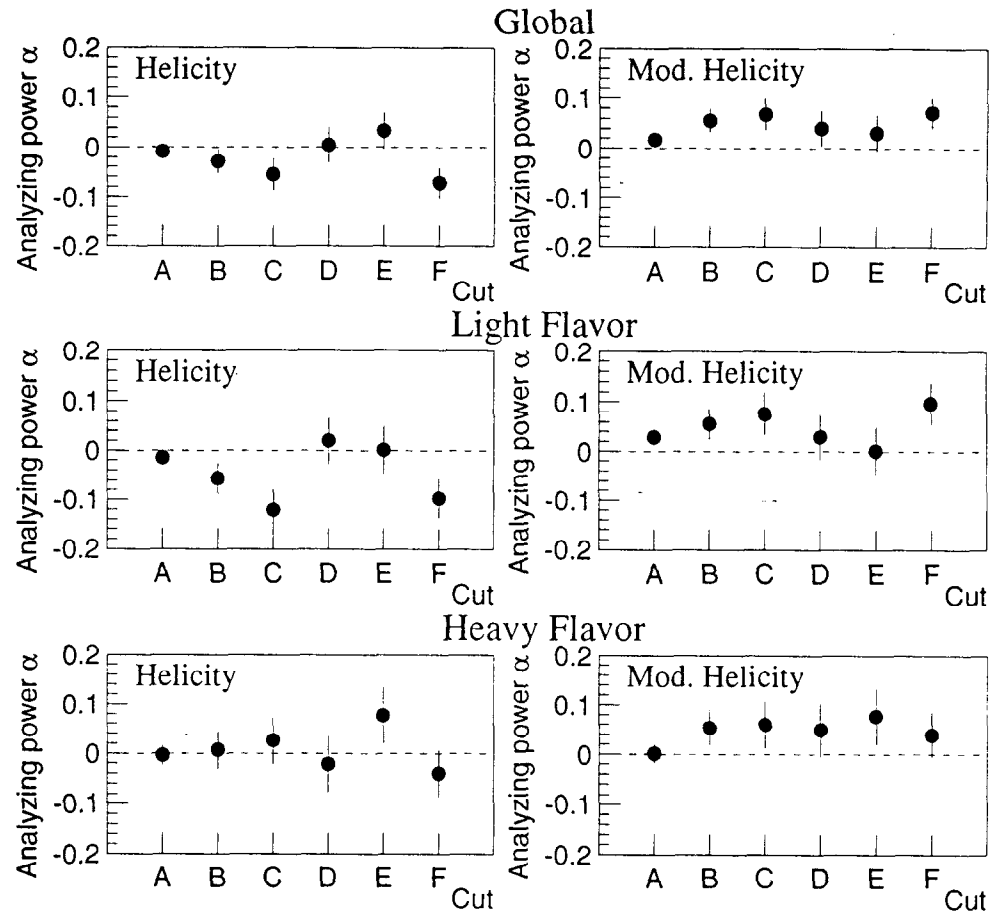
Figure B.4: Dependence of the analyzing power on the invariant mass cuts for the global, light- and heavy-flavor samples. Results from Cut C and Cut D (Cut E and Cut F) are not correlated. The other results are correlated with each other.

and the tendency are significant.

Appendix C

Systematic Errors

As mentioned in Section 4.8, we considered the following three sources of systematic errors.

1. **Track and event selection**

   The criteria for track and event selection are divided into two categories which are concerned with detector acceptance and transverse momentum, visible energy, etc. Therefore, we considered samples with loose and tight cuts for these two categories of track and event selection.

2. **Jet finding**

   In this study, the P scheme of the JADE algorithm was used as the jet-finding algorithm. The systematic error due to jet-finding algorithms was also studied by using P0, E and E0 schemes[1] of the JADE algorithm. DURHAM[37] and GENEVA[38] algorithms were also used. y_{cut} values are suitably chosen to produce same number of 2-jet events as P scheme of the JADE algorithm with $y_{cut} = 0.03$. The systematic error due to variation of y_{cut} value was also estimated.

3. **Analysis**

   The analysis method may introduce bias in the results. To estimate the bias, exactly same analysis was performed using the events generated by the Monte Carlo simulation (the MC events). Since the Monte Carlo simulation does not take into account jet handedness, the MC events should give zero jet handedness. Therefore, the difference between the result from these events and zero is regarded as the systematic bias due to the analysis method. About 200k of events generated by tuned JETSET 6.3 program[29] with the SLD detector

---

[1]The difference in the P, P0, E and E0 schemes of the JADE algorithm is the calculation of invariant mass, y_{ij} (4.4), and the method of combination (4.5) [42].

simulation were used in these studies. These simulations give a good description of our measured inclusive track and event topology distributions as shown in Section 4.3. As for the Ω in the analyses, Figure C.1 shows comparisons of the Ω distribution for data to that for the MC events in which spin transport was not simulated. For the helicity-based analysis, distributions of $\text{sign}(\mathcal{P}\cos\theta)\Omega_{hel}$ are shown for the three samples. Those figures show only distribution for the 3-leading-particle selection method. For the N-leading-particle and the particle selection method based on rapidity and momentum, difference between data and the MC events was not found in Ω distribution. The data and the MC events had also similar distributions of other quantities, such as charged track multiplicity of a jet, rapidity and transverse momentum with respect to the jet axis as shown in Figures 4.30, 4.32 and 4.33. Those quantities are important because of the relation with N_{lead} in the N-leading-particle selection method, n_{max}, Δn and p_{min} in the particle selection method based on rapidity and momentum. This means that the Monte Carlo program can well simulated the SLD detector acceptance and resolutions. The bias due to the analysis method was estimated by removing such effects.

Event samples used in the study of the systematic errors are summarized in Table C.1.

The analyzing power α_i was calculated for a sample i. Then the following quantity $\Delta\alpha$ was defined.

$$\Delta\alpha = \sqrt{\frac{\sum_i(\alpha_i - \alpha_{std})^2}{N_{samples}}} \tag{C.1}$$

where i runs all samples in same source, *e.g.* from (a1) to (a2) in Table C.1, and $N_{samples}$ is the number of samples for same source, *e.g.* 2 for the source due to acceptance. α_{std} is the analyzing power calculated with the *standard*[2] criteria. The systematic error $\Delta\alpha_{sys}$ for each source is defined as:

$$\Delta\alpha_{sys} = \sqrt{\Delta\alpha^2 - \Delta\alpha_{stat}^2} \tag{C.2}$$

where $\Delta\alpha_{stat}$ is the statistical fluctuation of the analyzing power. If $\Delta\alpha$ is smaller that $\Delta\alpha_{stat}$, the systematic error is neglected. Otherwise, $\pm\Delta\alpha_{sys}$ is regarded as the systematic error.

The systematic error (C.2) was calculated for each source except for the bias due to the analysis methods. Using the fact that the analyzing power for the MC events should be zero, the shift of the analyzing power from zero gives the bias of each analysis method including statistical fluctuation. Removing the statistical fluctuation by similar way as (C.2), the bias including sign was determined.

---

[2]The *standard* criteria means the criteria described in Section 4.3.

Source	Sample #	Criteria
Track and event selection		
Acceptance	(a1)	Loose : no cut on $\cos\theta_{track}$ and $\lvert\cos\theta_{thrust}\rvert < 0.8$.
	(a2)	Tight : $\cos\theta_{track} < 0.75$ and $\lvert\cos\theta_{thrust}\rvert < 0.65$.
p_t, r_0, z_0 and E_{vis}	(b1)	Loose : no cut on p_t, r_0, z_0 and E_{vis}.
	(b2)	Tight : $p_t > 0.3$ GeV/c, $r_0 < 2.5$ cm, $z_0 < 5.0$ cm and $E_{vis} > 30$ GeV,
Jet finding		
Algorithm	(c1)	P scheme with $y_{cut} = 0.0235$
	(c2)	E scheme with $y_{cut} = 0.054$
	(c3)	E0 scheme with $y_{cut} = 0.0305$
	(c4)	DURHAM with $y_{cut} = 0.008$
	(c5)	GENEVA with $y_{cut} = 0.038$
y_{cut}	(d1)	$y_{cut} = 0.028$
	(d2)	$y_{cut} = 0.032$
Analysis		
Method	(e)	200K events generated by the Monte Carlo simulation

Table C.1: The sources of the systematic errors and samples for the estimate of the systematic errors.

The total systematic error was calculated as a quadratic sum of the systematic errors from all sources. Due to the bias from the analysis method, the total systematic errors may not have same magnitude in positive and negative signs.

The systematic errors for the three-leading-particle selection method are summarized in Table C.2. The results shows the systematic errors are negligible or quite small. This means that the method does not give biases to the analyzing power.

Figure C.2 shows the systematic errors from each source shown in Table C.1 for the N-leading-particle selection method.

The systematic errors from each source for the particle selection method based on rapidity and momentum are shown in Figure C.3, C.4 and C.5 for the global, light flavor and heavy flavor samples, respectively.

Source	Sample	Analysis	Global	Light	Heavy
Track and event selection					
	acceptance (a)	Helicity	~ 0	~ 0	~ 0
		Modified helicity	~ 0	~ 0	~ 0
		Chirality	~ 0	~ 0	~ 0
	momenta etc. (b)	Helicity	~ 0	~ 0	~ 0
		Modified helicity	~ 0	~ 0	~ 0
		Chirality	~ 0	~ 0	~ 0
	subtotal	Helicity	~ 0	~ 0	~ 0
		Modified helicity	~ 0	~ 0	~ 0
		Chirality	~ 0	~ 0	~ 0
Jet finding					
	Algorithm (c)	Helicity	~ 0	~ 0	~ 0
		Modified helicity	~ 0	~ 0	~ 0
		Chirality	~ 0	~ 0	~ 0
	y_{cut} (d)	Helicity	~ 0	~ 0	~ 0
		Modified helicity	~ 0	~ 0	~ 0
		Chirality	~ 0	~ 0	~ 0
	subtotal	Helicity	~ 0	~ 0	~ 0
		modified helicity	~ 0	~ 0	~ 0
		Chirality	~ 0	~ 0	~ 0
Analysis					
	Method (e)	Helicity	~ 0	~ 0	+0.001
		Modified helicity	~ 0	~ 0	~ 0
		Chirality	−0.003	~ 0	~ 0
total		Helicity	~ 0	~ 0	$+0.001_{-0.000}$
		Modified helicity	~ 0	~ 0	~ 0
		Chirality	$+0.000_{-0.003}$	~ 0	~ 0

Table C.2: The systematic errors for the 3-leading-particle selection method. The subtotal is calculated as a quadratic sum of all sources in same category. The total systematic error is a quadratic sum of all sources.
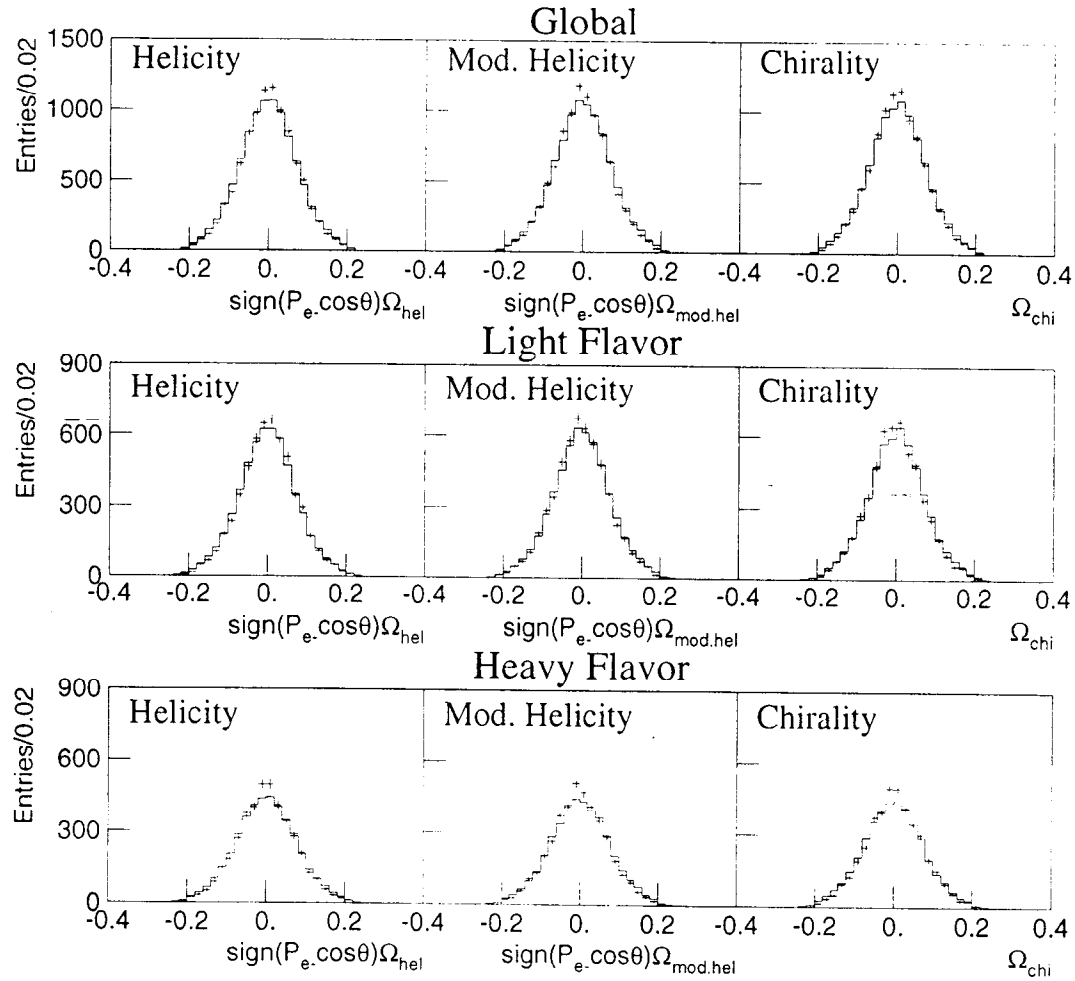
Figure C.1: Comparison of Ω distributions for data to that for the MC events. Shown are data (puls symbols whose vertical lines show their statistical errors) and the Monte Carlo (histograms).
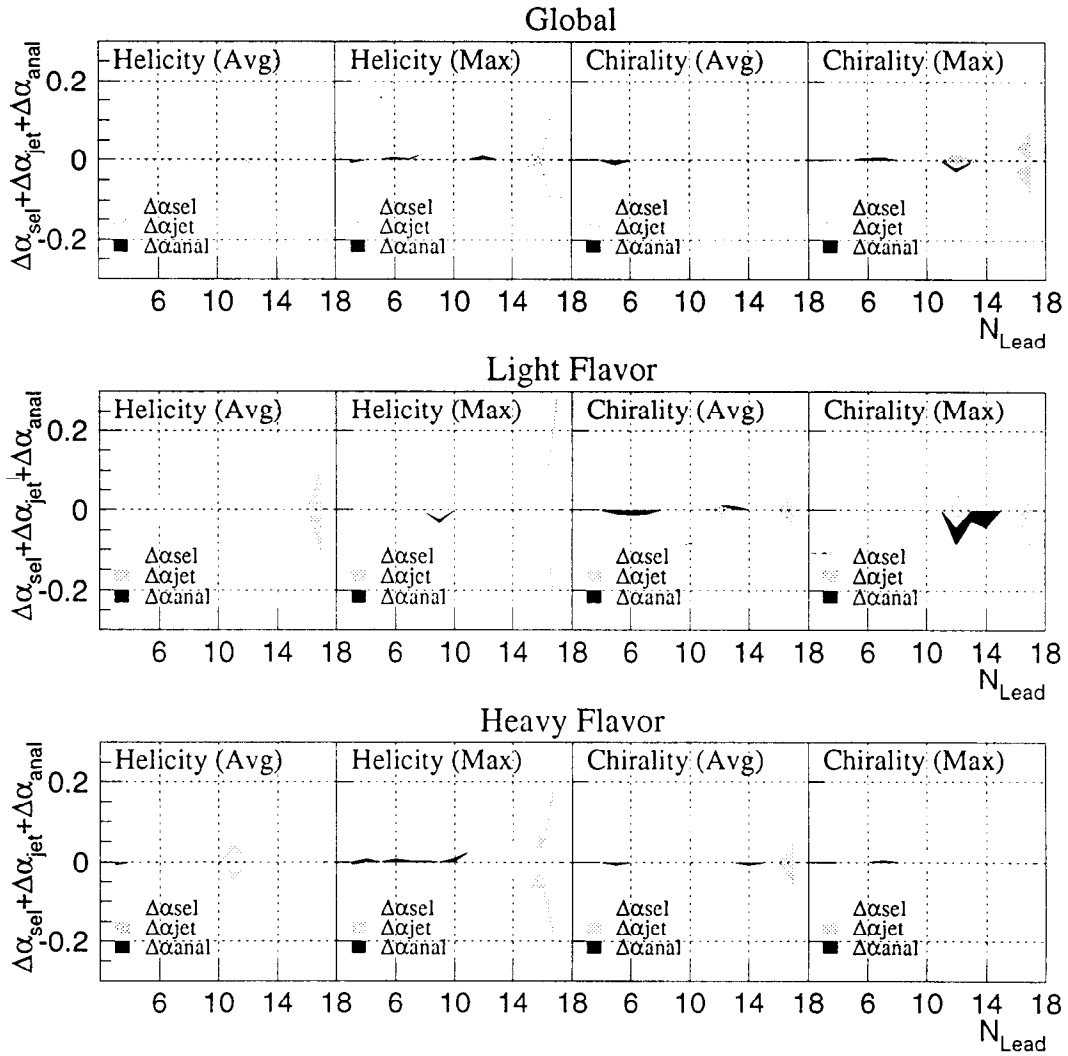
Figure C.2: The systematic errors from the sources for the N-particle-selection method. The light and dark hatched areas show the systematic errors from track and event selection and jet finding, respectively. The black area shows the systematic error from the analysis method.
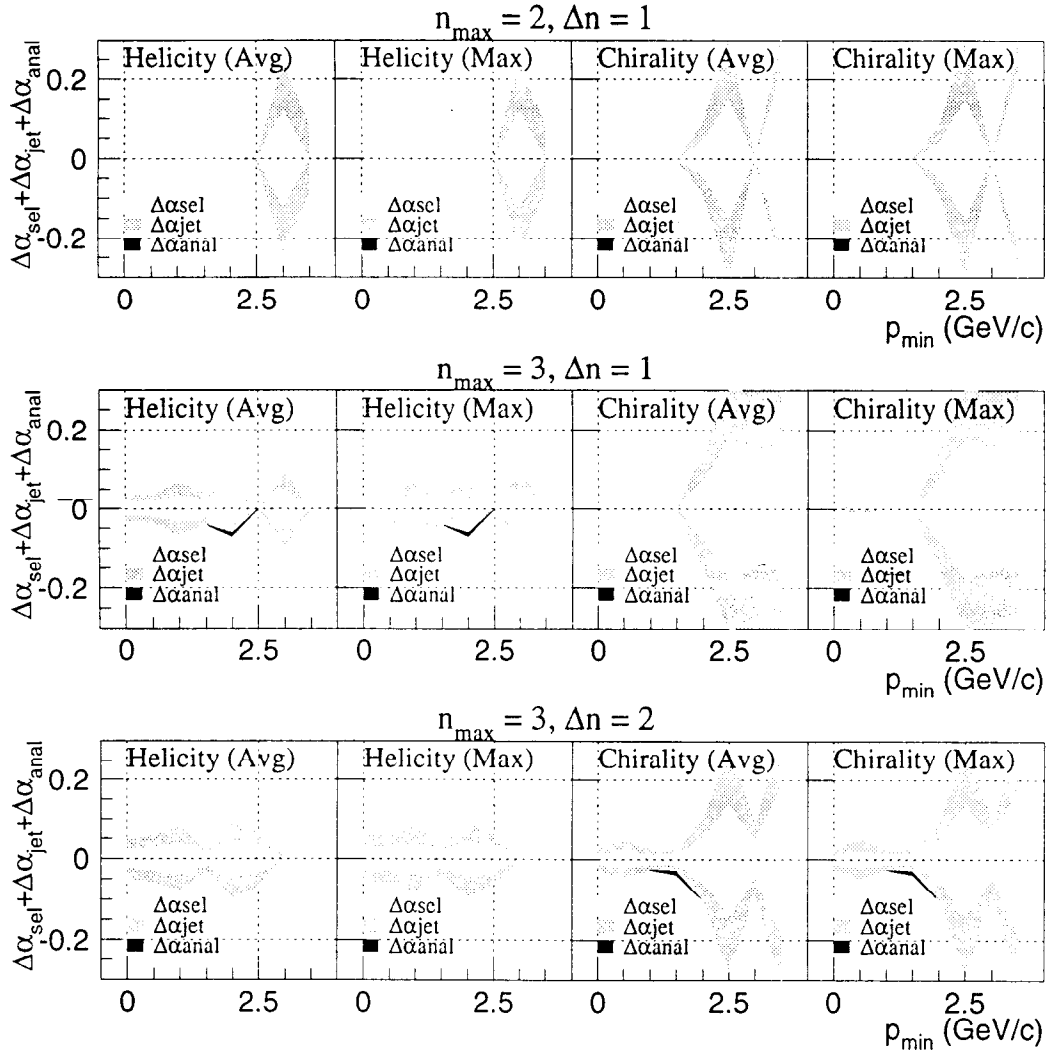
Figure C.3: The systematic errors from the sources for the particle selection method based on rapidity and momentum for the global sample. The light and dark hatched areas show the systematic errors from track and event selection and jet finding, respectively. The black area shows the systematic error from the analysis method.
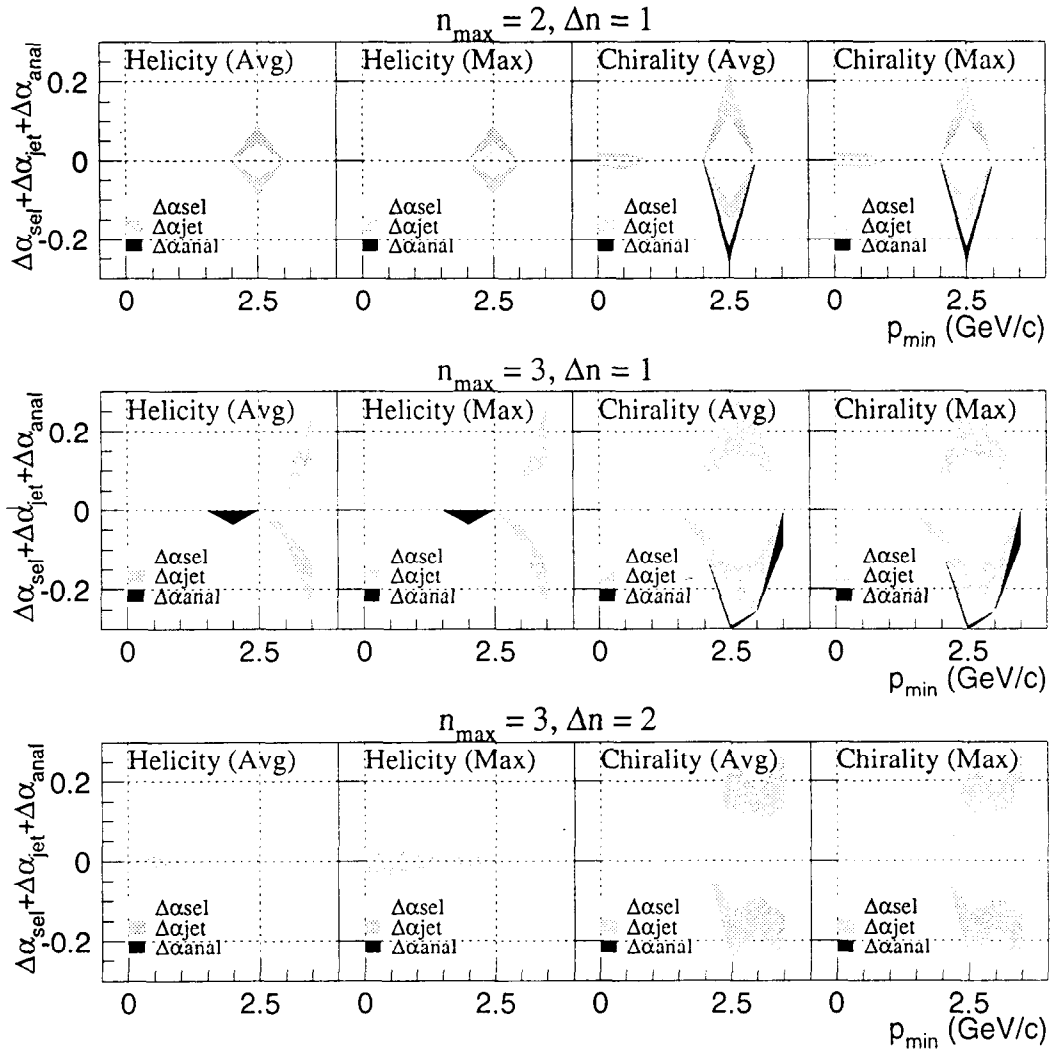
Figure C.4: The systematic errors from the sources for the particle selection method based on rapidity and momentum for the light flavor sample. The light and dark hatched areas show the systematic errors from track and event selection and jet finding, respectively. The black area shows the systematic error from the analysis method.

Figure C.5: The systematic errors from the sources for the particle selection method based on rapidity and momentum for the heavy flavor sample. The light and dark hatched areas show the systematic errors from track and event selection and jet finding, respectively. The black area shows the systematic error from the analysis method.
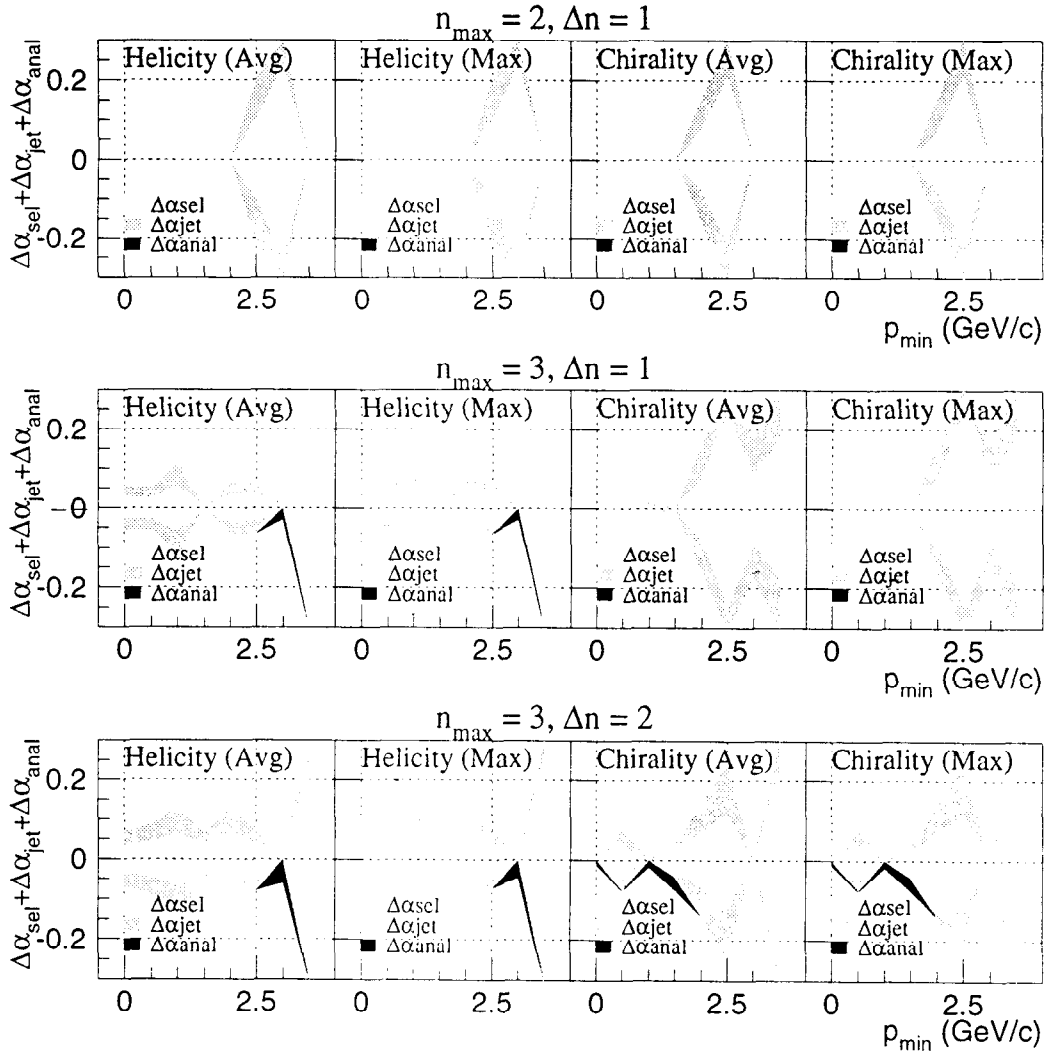
Appendix D

The SLD Collaboration

K. Abe[29], I. Abt[14], C. J. Ahn[26], T. Akagi[27], N. J. Allen[27], W. W. Ash[27], D. Aston[27],
K. G. Baird[24], C. Baltay[33], H. R. Band[32], M. B. Barakat[33], G. Baranko[10],
O. Bardon[16], T. Barklow[27], A. O. Bazarko[11], R. Ben-David[33], A. C. Benvenuti[2],
T. Bienz[27], G. M. Bilei[22], D. Bisello[21], G. Blaylock[7], J. R. Bogart[27], T. Bolton[11],
G. R. Bower[27], J. E. Brau[20], M. Breidenbach[27], W. M. Bugg[28], D. Burke[27],
T. H. Burnet[31], P. N. Burrows[16], W. Busza[16], A. Calcaterra[13], D. O. Caldwell[6],
D. Calloway[27], B. Camanzi[12], M. Carpinelli[23], R. Cassel[27], R. Castaldi[23],
A. Castro[21], M. Cavalli-Sforza[7], E. Church[31], H. O. Cohn[28], J. A. Coller[3],
V. Cook[31], R. Cotton[4], R. F. Cowan[16], D. G. Coyne[7], A. D'Oliveira[8],
C. J. S. Damerell[25], M. Daoudi[27], R. De Sangro[13], P. De Simone[13], R. Dell'Orso[23],
M. Dima[9], P. Y. C. Du[28], R. Dubois[27], B. I. Eisenstein[14], R. Elia[27], D. Falciai[22],
C. Fan[10], M. J. Fero[16], R. Frey[20], K. Furuno[20], T. Gillman[25], G. Gladding[14],
S. Gonzalez[16], G. D. Hallewell[27], E. L. Hart[28], Y. Hasegawa[29], S. Hedges[4],
S. S. Hertzbach[17], M. D. Hildreth[27], J. Huber[20], M. E. Huffer[27], E. W. Hughes[27],
H. Hwang[20], Y. Iwasaki[29], D. J. Jackson[25], P. Jacques[24], J. Jaros[27], A. S. Johnson[3],
J. R. Johnson[32], R. A. Johnson[8], T. Junk[27], R. Kajikawa[19], M. Kalelkar[24],
I. Karliner[14], H. Kawahara[27], H. W. Kendall[16], Y. Kim[26], M. E. King[27], R. King[27],
R. R. Kofler[17], N. M. Krishna[10], R. S. Kroeger[18], J. F. Labs[27], M. Langston[20],
A. Lath[16], J. A. Lauber[10], D. W. G. Leith[27], X. Liu[7], M. Loreti[21], A. Lu[6],
H. L. Lynch[27], J. Ma[31], G. Mancinelli[22], S. Manly[33], G. Mantovani[22],
T. W. Markiewicz[27], T. Maruyama[27], R. Massetti[22], H. Masuda[27], E. Mazzucato[12],
A. K. McKemey[4], B. T. Meadows[8], R. Messner[27], P. M. Mockett[31], K. C. Moffeit[27],
B. Mours[27], G. Müller[27], D. Muller[27], T. Nagamine[29], U. Nauenberg[10], H. Neal[27],
M. Nussbaum[8], Y. Ohnishi[19], L. S. Osborne[16], R. S. Panvini[30], H. Park[20],
T. J. Pavel[27], I. Peruzzi[13], M. Piccolo[13], L. Piemontese[12], E. Pieroni[23], K. T. Pitts[20],
R. J. Plano[24], R. Prepost[32], C. Y. Prescott[27], G. D. Punkar[27], J. Quigley[16],
B. N. Ratcliff[27], T. W. Reeves[30], P. E. Rensing[27], L. S. Rochester[27],

J. E. Rothberg[31], P. C. Rowson[11], J. J. Russel[27], O. H. Saxton[27], T. Schalk[7],
R. H. Schindler[27], U. Schneekloth[16], B. A. Schumm[15], A. Seiden[7], S. Sen[33],
V. V. Serbo[32], M. H. Shaevitz[11], J. T. Shank[3], G. Shapiro[15], S. L. Shapiro[27],
D. J. Sherden[27], C. Simopoulos[27], N. B. Sinev[20], S. R. Smith[27], J. A. Snyder[33],
P. Stamer[24], H. Steiner[15], R. Steiner[1], M. G. Strauss[17], D. Su[27], F. Suekane[29],
A. Sugiyama[19], S. Suzuki[19], M. Swartz[27], A. Szumilo[31], T. Takahashi[27],
F. E. Taylor[16], E. Torrence[16], J. D. Turk[33], T. Usher[27], J. Va'vra[27], C. Vannini[23],
E. Vella[27], J. P. Venuti[30], R. Verdier[16], P. G. Verdini[23], S. R. Wagner[27],
A. P. Waite[27], S. J. Watts[4], A. W. Weidemann[28], E. R. Weiss[31], J. S. Whitaker[3],
S. L. White[28], F. J. Wickens[25], D. A. Williams[7], D. C. Williams[16], S. H. Williams[27],
S. Willocq[33], R. J. Wilson[9], W. J. Wisniewski[5], M. Woods[27], G. B. Word[24],
J. Wyss[21], R. K. Yamamoto[16], J. M. Yamartino[16], X. Yang[20], S. J. Yellin[6],
C. C. Young[27], H. Yuta[29], G. Zapalac[32], T. W. Zdarko[27], C. Zeitlin[20], Z. Zhang[16]
and J. Zhou[20]

[1] Adelphi University, Garden City, New York 11530
[2] INFN Sezione di Bologna, I-40126 Bologna, Italy
[3] Boston University, Boston, Massachusetts 02215
[4] Brunel University, Uxbridge, Middlesex, UB8 3PH, United Kingdom
[5] California Institute of Technology, Pasadena, California 91125
[6] University of California at Santa Barbara, Santa Barbara, California 93106
[7] University of California at Santa Curz, Santa Curz, California 95064
[8] University of Cincinnati, Cincinnati, Ohio 45221
[9] Colorado State University, Fort Collins, Colorado 80523
[10] University of Colorado, Boulder, Colorado 80309
[11] Columbia University, New York, New York 10027
[12] INFN Sezione di Ferrara and Università di Ferrara, I-44100 Ferrara, Italy
[13] INFN Lab. Nazionali di Frascati, I-00044 Frascati, Italy
[14] University of Illinois, Urbana, Illinois 61801
[15] Lawrence Berkeley Laboratory, University of California, Berkeley, Clifornia 94720
[16] Massachusetts Institute of Technology, Cambridge, Massachusetts 02139
[17] University of Massachusetts, Amherst, Massachusetts 01003
[18] University of Mississippi, University, Mississippi 38677
[19] Nagoya University, Chikusa-ku, Nagoya 464 Japan
[20] University of Oregon, Eugene, Oregon 97403
[21] INFN Sezione di Padova and Università di Padova, I-35100 Padova, Italy
[22] INFN Sezione di Perugia and Università di Perugia, I-06100 Perugia, Italy
[23] INFN Sezione di Pisa and Università di Pisa, I-56100 Pisa, Italy
[24] Rutgers University, Piscataway, New Jersey 08855
[25] Rutherford Appleton Laboratory, Chilton, Didcot, Oxon OX11 0QX United
Kingdom

· [26] Sogang University, Seoul, Korea
[27] Stanford Linear Accelerator Center, Stanford University, Stanford, California 94309
[28] University of Tennessee, Knoxville, Tennessee 37996
[29] Tohoku University, Sendai 980 Japan
[30] Vanderbilt University, Nashville, Tennessee 37235
[31] University of Washington, Seattle, Washington 98195
[32] University of Wisconsin, Madison, Wisconsin 53706
[33] Yale University, New Haven, Connecticut 06511

Bibliography

[1] O. Nachtmann. A NEW TOOL FOR THE STUDY OF FUNDAMENTAL INTERACTIONS, parity-odd correlations in quark fragmentation. *Nuclear Physics*, B127:314–330, 1977.

[2] R. H. Dalitz, G. R. Goldstein, and R. Marshall. On the helicity of charm jets. *Zeitschrift für Physik*, C42:441–448, 1989.

[3] A. V. Efremov, L. Mankiewicz, and N. A. Törnqvist. Jet handedness as a measure of quark and gluon polarization. *Physics Letters*, B284:394–400, 1992.

[4] A. Rougé. Polarization observables in the $3\pi\nu$ decay mode of the τ. *Zeitschrift für Physik*, C48:75–77, 1990.

[5] J. H. Kühn and E. Mirkes. Angular distributions in semileptonic τ decays. *Physics Letters*, B286:381–386, 1992.

[6] A. V. Efremov, L. Mankiewicz, and N. A. Törnqvist. On the handedness in polarized $\tau \to a_1\nu \to 3\pi\nu$ decay. *Physics Letters*, B291:473–480, 1992.

[7] C. Quigg. *Gauge Theories of the Strong, Weak and Electromagnetic Interactions*, chapter 7, pages 156–164. Addison–Wesley, 1983.

[8] M. G. Ryskin. The origin of handedness in the jet fragmentation. *Physics Letters*, B319:346,347, 1993.

[9] SLD Collaboration, P. N. Burrows et al. Studies of qcd b physics and jet handedness at sld. In *Les Arcs 1993, Proceedings, QCD and high energy hadronic interactions*, 1993.

[10] SLD Collaboration, H. Masuda et al. A study of jet handedness at the z0 resonance. In *Marseille 1993, Proceedings, High energy physics*, 1993.

[11] SLD Collaboration, K. Abe et al. A search for jet handedness in hadronic z0 decays. SLAC-PUB-6643, Submitted to Physical Review Letters, 1994.

[12] F. Halzen and A. D. Martin. *QUARKS & LEPTONS: An Introductory Course in Modern Particle Physics.* JOHN WILEY & SONS, New York, 1984.

[13] Particle Data Group, L. Montanet et al. Review of particle properties. *Physical Review*, D50:1173–1826, 1994.

[14] V. D. Barger and R. J. N. Phillips. *Collider Physics*, chapter 6, pages 180–188. Addison–Wesley, 1987.

[15] G. Marchesini et al. HERWIG 5.1 – a Monte Carlo event generator for simulating hard emission reactions with interfering gluons. *Computer Physics Communications*, 67:465–508, 1992.

[16] B. Andersson. The lund model. *Nuclear Physics*, A461:513–520, 1987.

[17] K. Hagiwara and D. Zeppenfeld A. D. Martin. τ polarization measurements at LEP and SLC. *Physics Letters*, B235:198–202, 1990.

[18] The ALEPH Collaboration, D. Decamp et al. Measurement of the polarization of τ leptons produced in z decays. *Physics Letters*, B265:430–444, 1991.

[19] The L3 Collaboration, M. Acciarri et al. A mesurement of τ polarization in z^0 decays. *Physics Letters*, B298, 1992.

[20] SLD Collaboration, K. Abe et al. Precise Measurement of the Left-Right Cross Section Asymmetry in Z Boson Production by e^+e^- Collisions. *Physical Review Letters*, 73:25–29, 1994.

[21] R. Dubois. Precision Electroweak Experiments at SLD. Presented at XXII SLAC Summer Institute on Particle Physics, August 1994.

[22] D. T. Pierce and F. Meier. Photoemission of spin-polarized electrons from gaas. *Physical Review*, B13:5484, 1976.

[23] T. Maruyama et al. High polarization photocathode r&d at slac. SLAC-PUB-6033, January 1993.

[24] R. C. King. *A Precise Measurement of the Left-Right Asymmetry of Z Boson Production at the SLAC Linear Colloder.* PhD thesis, Stanford University, September 1994.

[25] R. D. Elia. *Measurement of the Left-Right Asymmetry in Z Boson Production by Electron-positron Collisions.* PhD thesis, Stanford University, April 1994.

[26] P. Billoir. Track fitting with multiple scattering: A new method. *Nuclear Instruments & Methods in Physics Research*, 225:352, 1984.

[27] D. C. Williams. *The left-Right Forward-Backward Asymmetry for B quarks at the SLD*. PhD thesis, Massachusetts Institute of Technology, May 1994.

[28] S. C. Berridge et al. First Results From the SLD Sillicon Calorimeters. SLAC-PUB-5694, November 1991.

[29] T. Sjöstrand and M. Bengtsson. THE LUND MONTE CARLO FOR JET FRAGMENTATION AND e^+e^- PHYSICS – JETSET 6.3 – AN UPDATE. *Computer Physics Communications*, 43:367–379, 1986.

[30] S. Jadach, B. F. L. Ward, and Z. Wąs. The Monte Carlo program KORALZ, version 3.8, for the lepton or quark pair production at LEP/SLC energies. *Computer Physics Communications*, 66:276–292, 1991.

[31] B. F. L. Ward et al. Monte Carlo BHLUMI-2.01 for Bhabha scattering at low angles with Yennie-Frautschi-Suura exponentiation. *Computer Physics Communications*, 70:305–344, 1992.

[32] H. Aihara et al. Measurement of the photon structure function $F_2^\gamma(x, Q^2)$ in the region 0.2 GeV$^2 < Q^2 < 7$ GeV^2. *Zeitschrift für Physik*, C34:1, 1987.

[33] R. Brun et al. GEANT3 user's guide. CERN-DD/EE/84-1, CERN.

[34] J. M. Yamartino. Hadronic Event Selection Using the LAC. SLD Physics Note # 14, November 1992.

[35] E. Fahri. Quantum chromodynamics test for jets. *Physical Review Letters*, 39:1587, 1977.

[36] W. Bartel et al. Experimental study on multi-jet production in e^+e^- annihilaion at PETRA energies. *Zeitschrift für Physik*, C33:23, 1986.

[37] S. Bethke et al. New Jet Cluster Algorithms: Next-to-leading order QCD and hadronization corrections. *Nuclear Physics*, B370:310–334, 1992.

[38] G. Kramer and B. Lampe. Two-jet cross section in e^+e^- annihilation. *Zeitschrift für Physik*, C34:497–522, 1987.

[39] SLD Collaboration, G. Punkar et al. Measurement of the Average lifetime of B Hadrons at SLD. SLAC-PUB-5595, September 1994.

[40] S. Jadach, Z. Wąs, R. Decker, and J. H. Kühn. The τ decay library TAUOLA, version 2.4. *Computer Physics Communications*, 76:276–292, 1993.

[41] D. Muller. Private communication, 1994.

[42] J. A. Lauber. *A Study of Jet Rates and a Measurement of* α_s *at the* Z^0 *Resonance.* PhD thesis, University of Colorado, 1992. Section 4.3.